Ferredoxins containing Heterometallic Clusters – Synthesis and Characterization

Martic, Maja

Publication date:
2011

Document Version
Publisher's PDF, also known as Version of record

Ferredoxins containing Heterometallic Clusters – Synthesis and Characterization

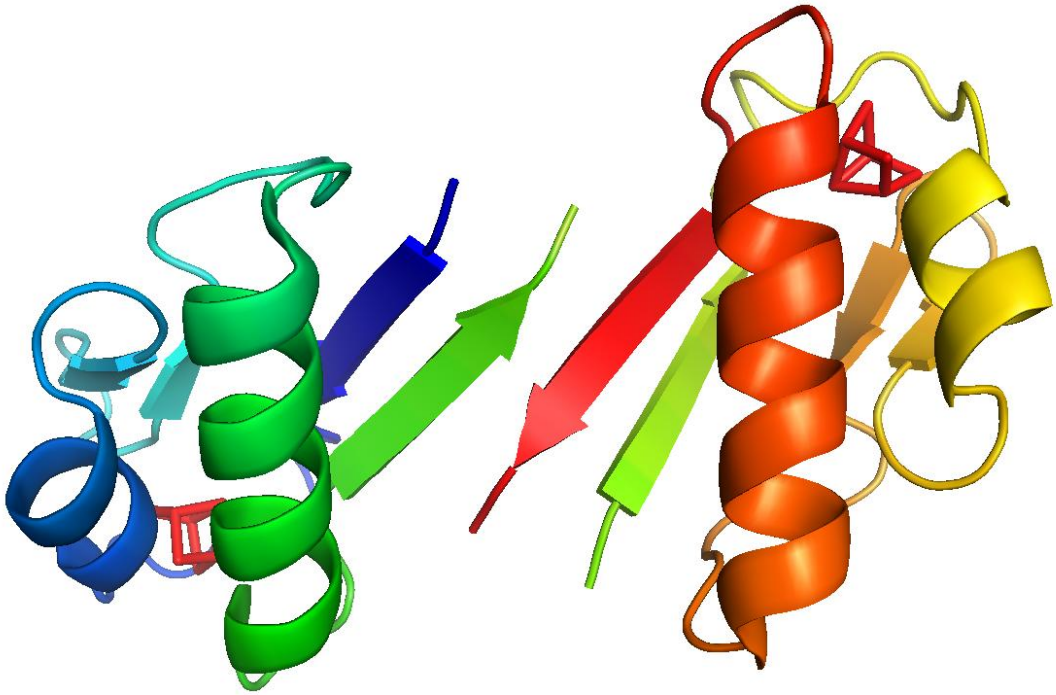

Ph.D. Thesis by Maja Martic

Metalloprotein Chemistry and Engineering Group
Department of Chemistry
Technical University of Denmark
January 2011

Ferredoxins containing Heterometallic Clusters – Synthesis and Characterization

Ph.D. Thesis by Maja Martic

Metalloprotein Chemistry and Engineering Group
Department of Chemistry
Technical University of Denmark
January 2011

Front page illustration: The structure of the wild-type ferredoxin from *Pyrococcus furiosus*. The figure was made using PyMol by DeLano Scientific.

Preface and Acknowledgements

This dissertation is a result of my three years work as a Ph.D. student in the Metalloprotein Chemistry and Engineering Group, Department of Chemistry, Technical University of Denmark, with Associate Professor Hans E. M. Christensen as my main supervisor and the late Associate Professor Bee Lean Ooi as co-supervisor. I would like to thank them very much for always being friendly and supportive, and for their guidance throughout my work.

A special thank goes to Professor Wilfred R. Hagen at Delft University of Technology (Netherlands) for his help and guidance with electron paramagnetic resonance spectroscopic characterization.

I also wish to thank the members of the Metalloprotein Chemistry Group for providing a nice and friendly atmosphere. Special thanks go to Laboratory Technicians Lise-Lotte Jespersen, Stefanie Boy and Martin Hasling Pedersen for always being helpful. Erasmus student Jordi Espín Martí is acknowledge for his work on the D14C variant during his stay in our group. Also, I would like to thank Ph.D. Jytte Kristensen, Assoc. Prof. Jingdong Zhang, Ph.D. Hanne Nørgaard, and Ph.D. student Monika Nøhr Løvgreen for very helpful and valuable scientific discussions and advices.

Additionally, I would like to thank The Danish Research Council for Technology and Production Sciences for providing the Ph.D. scholarship and funding for this project.

Finally, I wish to thank my family for their love, support and understanding.

Kgs. Lyngby, 31st of January 2011

_____

Maja Martic

Abstract

Ubiquitously found in nature with great diversity in function, relatively small in size, and with apparently early use in evolution, iron-sulfur proteins are found in to be an ideal template for bioinspired catalysis. *Pyrococcus furiosus* ferredoxin is a small iron-sulfur protein containing a [Fe_4S_4] cluster in which one Fe-ion lacks cysteinyl coordination and that Fe-ion can easily be removed and the cluster converted to the [Fe_3S_4] form. Incubation of the [Fe_3S_4] form with appropriate metal-ions ($M^{2+/+}$) leads to the formation of artificial ferredoxins containing heterometallic cluster [M-Fe_3S_4].

This project concerns the synthesis and characterization of artificial ferredoxins using wild type *Pyrococcus furiosus* ferredoxin (WT *P.f.* Fd) and its D14C variant as a starting material. Thus, two sets of artificial ferredoxins were synthesized and subsequently characterized using multidisciplinary approach consisting of mass spectrometric analysis, electrochemical and EPR spectroscopic characterization. The first set of artificial ferredoxins contains the [Zn-Fe_3S_4] cluster and the second the [Ag-Fe_3S_4] cluster.

WT *P.f.* Fd and its D14C variant were studied as reference systems for these artificial ferredoxins. They were characterized using mass spectrometric analysis of intact metalloproteins and a bulk solution cyclic voltammetry under anaerobic conditions. Oxidation of [Fe_4S_4] to [Fe_3S_4] D14C *P.f.* Fd has turned out to be pH dependent under aerobic conditions. It was successfully carried out at pH 5.8 by overnight incubation using excess of ferricyanide. At pH 8.0 the formation of disulfide bonded dimer occurs which was confirmed by mass spectrometric analysis. The D14C variant containing the [Fe_3S_4] cluster was electrochemically characterized for the first time and the formal potential is -155 mV vs. SHE.

Both the WT *P.f.* Fd and its variant D14C containing [Zn-Fe_3S_4] cluster were successfully synthesized and chromatographically purified under anaerobic conditions. The artificial ferredoxins were characterized using the multidisciplinary approach. Mass spectrometric data showed that the proteins were synthesized in a form containing the reduced cluster [Zn-Fe_3S_4]$^+$ and that a good separation was achieved during the purification procedure. Both ferredoxins containing [Zn-Fe_3S_4] cluster were electrochemically characterized and the formal potentials determined for the [Zn-Fe_3S_4] cluster in the WT *P.f*. Fd and in the D14C *P.f*. Fd are -206 mV and -254 mV vs. SHE, respectively. The EPR spectroscopy has confirmed the presence of the [Zn-Fe_3S_4]$^+$ cluster (ground spin state S = 5/2) in both WT and D14C *P.f*. Fd.

The [Ag-Fe_3S_4] cluster was synthesized for the first time inside a protein. The WT *P.f*. Fd and its D14C variant containing the [Ag-Fe_3S_4] cluster were synthesized, chromatographically purified and characterized using UV-vis spectrophotometry, intact metalloprotein mass spectrometric analysis, cyclic voltammetry and EPR spectroscopy. Mass spectrometric analysis of the purified samples showed that the proteins are synthesized in a form containing the reduced cluster [Ag-Fe_3S_4]$^+$. Stability studies of these novel ferredoxins have shown that they are much more inert towards oxygen exposure than other ferredoxins containing heterometallic cluster, especially the [Ag-

Fe_3S_4] D14C *P.f*. Fd. Attempts were made to characterize both Fds electrochemically using a bulk solution cyclic voltammetry. However, no redox signal was obtained for the given conditions.The EPR spectroscopic studies combined with mass spectrometric analysis have confirmed the presence of the [Ag-Fe_3S_4] cluster in both WT and D14C *P.f*. Fd.

Resumé

Jern-svovl proteiner findes i næsten alle levende systemer og de har mange forskellige funktioner. De kan spores tilbage til den tidlige evolution og mange af dem er relativt små, hvilket gør dem til et ideelt udgangspunkt for udvikling af biologisk inspireret de nye katalytiske systemer. *Pyrococcus furiosus* ferredoxin er et lille jern-svovl protein som indeholder en $[Fe_4S_4]$-klynge, hvor en af jern-ionerne mangler koordinering til cystein. Denne jern-ion kan nemt fjernes og klyngen omdannes til en $[Fe_3S_4]$-klynge. Inkubering af $[Fe_3S_4]$-klyngen med passende metal-ioner ($M^{2+/+}$) fører til dannelsen af kunstige ferredoxiner, der indeholder heterometalliske klynger af typen $[M\text{-}Fe_3S_4]$.

Dette projekt omhandler syntese og karakterisering af kunstige ferredoxiner, hvor *Pyrococcus furiosus* ferredoxin og varianten D14C anvendes som udgangspunkt. Der er således syntetiseret og karakteriseret to set af kunstige ferredoxiner – et med en $[Zn\text{-}Fe_3S_4]$ klynge og et med en $[Ag\text{-}Fe_3S_4]$ klynge.

Som sammenligningsgrundlag for de kunstige ferredoxiner blev vildtype *Pyrococcus furiosus* ferredoxin (WT *P.f.* Fd) og D14C varianten også karakteriseret ved hjælp af massespektrometrisk analyse af intakte metalloproteiner og cyklisk voltammetri under oxygen-fri betingelser. Oxidation af $[Fe_4S_4]$ til $[Fe_3S_4]$ D14C *P.f.* Fd har vist sig at være pH-afhængig under aerobe betingelser. Oxidationen blev udført ved pH 5,8 ved inkubation natten over med overskud af ferricyanid. Ved pH 8,0 dannes en disulfidbundet dimer, hvilket blev bekræftet ved massespektrometrisk analyse. $[Fe_3S_4]$ D14C *P.f.* Fd er for første gang blevet karakteriseret ved hjælp af elektrokemi; det formelle potentiale er -155 mV vs. SHE.

Både WT *P.f.* Fd og D14C varianten med $[Zn\text{-}Fe_3S_4]$ klyngen er blevet syntetiserede og kromatografisk oprenset under oxygen-fri betingelser. De kunstige ferredoxiner er karakteriseret ved hjælp af intakt metalloprotein massespektrometrisk analyse, elektrokemi og EPR spektroskopi. Den massespektrometriske analyse viser, at proteinet indeholder en reduceret $[ZnFe_3S_4]^+$ klynge og at der er opnået god adskillelse i den kromatografiske separation. Begge ferredoxiner indeholdende en $[ZnFe_3S_4]$ klynge er blevet elektrokemisk karakteriseret og de formelle potentialer er for $[ZnFe_3S_4]$ WT *P.f*. Fd og for $[ZnFe_3S_4]$ D14C *P.f*. Fd henholdsvis -206 mV og -254 mV vs. SHE. Den EPR spektroskopiske analyse har bekræftet tilstedeværelsen af $[ZnFe_3S_4]^+$ klyngen (grund tilstand S = 5/2) i begge varianter.

$[Ag\text{-}Fe_3S_4]$ klyngen er blevet fremstillet for første gang i et protein. WT *P.f*. Fd og D14C varianten indeholdende en $[Ag\text{-}Fe_3S_4]$ klynge er blevet syntetiseret, kromatografisk oprenset og karakateriseret ved hjælp af spektrofotometri, intakt metalloprotein massespektrometrisk analyse, cyklisk voltammetri og EPR spektroskopi. Den massespektrometriske analyse viser, at proteinerne indeholder en reduceret $[Ag\text{-}Fe_3S_4]^+$ klynge. Stabilitetsstudier af disse nye ferredoxiner viser at de er mere stabile overfor dioxygen end andre heterometalliske ferredoxiner, specielt $[Ag\text{-}Fe_3S_4]$ D14C *P.f*. Fd varianten. Disse nye kunstige ferredoxiner er også forsøgt elektrokemisk karakteriseret, men der blev ikke observeret nogen signaler. De EPR spektroskopiske studier kombineret med den massespektrometriske analyse har bekræftet tilstedeværelsen af

[Ag-Fe_3S_4] klyngen i både vildtypen og D14C varianten af *P.f*. Fd; [Ag-Fe_3S_4]$^{2+}$ klyngen med en grund spin-tilstand S = 1/2 og [Ag-Fe_3S_4]$^{+}$ klyngen med en grund spin-tilstand S = 2.

Abbreviations

amp	Ampicillin
B	Magnetic field strength
Bis-Tris	Bis-(2-hydroxyethyl)imino-tris(hydroxymethyl)methane
carb	Carbenicillin
CV	Column volume
D.a.	*Desulfovibrio africanus*
D.g.	*Desulfovibrio gigas*
$E^{0'}$	Formal potential
ΔE	Peak-peak separation
E_a	Anodic peak potential
E_c	Cathodic peak potential
$E_{1/2}$	Peak half-width
EDTA	Ethylenediaminetetraacetate
EPG	Edge-plane pyrolytic graphite
EPR	Electron paramagnetic resonance
E.coli	*Escherichia coli*
ESI	Electrospray ionization
Fd	Ferredoxin
FeMo	Iron-molybdenum
FeS	Iron-sulfur
G	Receiver gain
HiPIP	High potential iron-sulfur protein
HPLC	High performance liquid chromatography
IPTG	Isopropyl-β-D-thiogalactopyranoside
LB	Luria broth
M	Modulation amplitude
MALDI	Matrix-assisted laser desorption ionization
MCP	Microchannel plate
Milli-Q	18.2 M cm water, Milli-Q Synthesis system (millipore)
m/z	Mass-to-charge
MS	Mass spectrometry
MWCO	Molecular weight cut off
Nano-ESI	Nano-electrospray ionization
OD_{600}	Optical density at 600 nm
v	Frequency of radiation

PBD	Protein data bank
P.f.	*Pyrococcus furiosus*
S	Primary spin quantum number of electrons
SHE	Standard hydrogen electrode
T	Temperature
TB	Terrific broth
TOF	Time-of-flight
Tris	Tris(hydroxymethyl)aminoethane
UV-vis	Ultraviolet-visible
WT	Wild type

The International system (SI) of units is used. Standard abbreviations of amino acids, elements and ions are used.

Contents

1 Introduction and Outline of the Thesis

Metalloproteins account for almost half of all naturally occurring proteins. They are involved in variety of important biological processes. Metalloprotein design and engineering offers the opportunity to improve the existing functional properties of natural metalloproteins or to impart them with new ones. Chapter 2 gives a brief overview of a current status of metalloprotein design and engineering.

Iron-sulfur proteins are widespread in nature, small in size with simple and structurally similar metal center; however, functionally very diverse which makes them ideal templates for metalloprotein design. Several iron-sulfur proteins are known to be involved in chemical catalysis where the catalytically active cuboidal-type [Fe_4S_4] cluster was found to lack cysteinyl ligation at the specific Fe-site and/or that Fe-site has been replaced by other transition metal (1; 2). This potential for heterometallic cuboidal-type cluster to participate in enzymatic catalysis has raised a great interest for these proteins.

This project concerns the synthesis and subsequent characterization of two sets of artificial iron-sulfur proteins containing heterometallic cluster. The small electron-transfer ferrdoxin (Fd) from the hyperthermophilic archaeon *Pyrococcus furiosus* (*P.f*.) was used as a template in this study. It contains [Fe_4S_4] cluster coordinated by three cysteinyle and one aspartate residue (3). The cluster readily interconverts to the [Fe_3S_4] form with the labile iron being coordinated to Asp14 residue (4). Site-directed mutagenesis of Asp14 to a cysteine residue (D14C) has been used to extensively study factors such as structural, electronic, and functional characteristics of Cys substitution. An introduction to the iron-sulfur class of proteins and particularly to the WT ferredoxin from the *P.f*. and its D14C variant is presented in chapter 3. These two ferredoxins were used for the synthesis of artificial ferredoxins containing heterometallic cluster in their active center. Two metal ions were used for incorporation into the [Fe_3S_4] cluster – Zn^{2+} and Ag^{+}.

Mass spectrometric analysis of intact metalloproteins has emerged as a powerful tool for characterization. It has been extensively used through this project hence this technique is introduced in chapter 4.

The experimental work is described in chapters 5 to 8. Chapter 5 describes the expression, purification and mass spectrometric characterization of WT *P.f.* Fd and its D14C variant. Electrochemical characterization of these proteins, which was used as a reference for studying the artificial ferredoxins, is presented in chapter 6. Chapter 7 describes the synthesis, purification, mass spectrometric, electrochemical and EPR spectroscopic characterization of two artificial ferredoxins containing the [Zn-Fe_3S_4] cluster in its active center. The same multidisciplinary approach is presented in chapter 8 for the two novel ferredoxins containing the [Ag-Fe_3S_4] cluster.

Chapter 9 gives the final concluding remarks based on the presented work and outlook for the future studies.

List of publications is presented in chapter 10.

2 Metalloprotein Design and Engineering

Metalloproteins account for about half of all the proteins in nature and about 1/3 of all structurally characterized proteins. They are among the most efficient and diverse biocatalysts responsible for catalysing important biological processes such as respiration, photosynthesis, etc. Therefore, understanding the structure and function of metalloproteins is of great importance. If creation is the ultimate demonstration of understanding, then the ultimate test to our knowledge is to design new metalloproteins that do not only reproduce the function and structure of native metalloproteins but also reveal some structural and/or functional features that may not be apparent from the studies of native metalloproteins (5).

As compared to design of non-metalloproteins, metalloprotein design seems to be more challenging since besides the issue of polypeptide chain design it also involves metal ions which are much larger in number than amino acids and with much more variable geometries which need to be taken into account (6).

Metalloprotein design and engineering open the possibility to design metalloproteins with improved properties compared to natural metalloproteins or to impart them with functions which are not found in nature. This will open the possibility of their wider pharmaceutical and biotechnological applications (7; 8).

Three approaches to metalloprotein design will be described in the following sections:

1) metalloprotein design in *de novo* designed scaffolds,
2) metalloprotein design in native protein scaffolds,
3) design of metalloproteins containing unnatural amino acids and nonnative metal-ions or metal-cofactors.

2.1 Metalloprotein Design in *De Novo* Designed Scaffolds

De novo design, or a design 'from scratch', involves constructing a polypeptide sequence that is not directly related to any natural protein but it folds into defined tree-dimensional structure that binds a metal ion (9; 10). De novo designed metallopeptides are systems that are generally much simpler than the natural metalloproteins that they are mimicking. However, they are sufficiently complex to provide understanding the functional properties of metalloproteins (11). Most of the *de novo* designed metalloproteins rely on unstructured linear peptide segments or on established α-helix and coiled-coil strategies (11).

The majority of work in this area has been done on introducing metal-binding sites into designed α-helical bundles which are a common heme-protein scaffold in nature (9). Therefore, heme centers were among the first metal centers incorporated into *de novo* α-helical bundles. A so-called 'heme protein maquettes' consist of four anti-parallel helical peptides and they can be from mono-heme binding to multi-heme maquettes (12; 13). These proteins were rationally designed by comparing them with native proteins as a mean to get information about the structure-stabilizing residues. Other metal ions/cofactors than heme were incorporated into α-helical bundles by introducing metal-

binding ligands. Cysteine ligands were introduced as metal binding ligands. This has led to a development of α-helical coiled-coil metaloproteins capable of binding Co(II), Fe(II), Cd(II), Zn(II), As(III), and Hg(II) (14).

2.2 Metalloprotein Design in Native Protein Scaffolds

Design of metal-binding sites in *de novo* designed scaffold represents the ultimate goal of metalloprotein design. However, the number of *de novo* designed scaffolds is limited to a few a very well-characterized ones as compared to more than 600 different natural scaffolds available in Protein Data Bank (6). Therefore, design of metal-binding site in native scaffolds offers much more choices and opportunities to build proteins with new properties. Also, native scaffolds are easier to crystallize, and the fact that the same scaffold can be seen in different proteins with diverse metal-binding motifs and structure suggests that these native scaffolds are also more robust and able to modify (5).

Different biochemical techniques such as site-directed mutagenesis have been used to study the function of metalloproteins. If the mutation of highly conserved residues is performed the loss of the protein function will allow identification of residues essential for the protein function. The mutagenesis technique can be used to impart a new function into the protein by introducing the residues that bind metal ions which can be performed by redesign of existing metal-binding sites, introduction of mononuclear metal-binding sites into proteins that natively do not bind metal ions, or by introducing the homonuclear or heteronuclear metal-binding sites into proteins (5; 6).

One of the simplest forms of metalloprotein design is redesign of existing metal-binding sites. However, this approach is still powerful in discovering which structural features are important for the change in function by redesign. Heme proteins have been redesigned in this way. Functionally, they are one of the most diverse groups of metalloproteins with functions such as electron transfer, small molecule sensing and transport, oxygen transport, etc. The key factors influencing their functional specificity are the types of hemes, nature of the axial ligands and the architecture of the distal site. Redesign was therefore focused on these three areas (15).

Redesign of existing metal-binding sites can provide insight into the structural differences between the template and the target protein but it cannot give us the information about the roles of structural features common to both of them. To overcome this problem, new metal-binding sites can be introduced into a protein where no native metal-binding site is found. Using this approach new Mn(II)-binding sites was designed in cytochrome *c* peroxidases (16).

2.3 Design of Metalloproteins Containing Unnatural Amino Acids and Nonnative Metal-Ions or Metal-Cofactors

Natural metalloproteins use only 20 amino acids, with only about 10 of them are potential metal ligands, and a small number of the metal ions listed in the periodical table. In order to build metalloproteins with properties that exceed those found in nature, introduction of unnatural amino acids and nonnative metal ions or metal-containing prosthetic group was necessary (17).

Several methods have been developed to incorporate unnatural amino acid. One of them is a total synthesis of proteins using a solid-state peptide synthesizes (18). However, a cost and a size constrains limit this method to smaller proteins (~ 60 – 100 amino acids). For large proteins a different method is required. Expressing the protein in cells lacking a particular amino acid and supplementing the growth media with an unnatural amino acid will cause the replacement of one type of amino acid with unnatural amino acid. However, this method can replace only a limited number of amino acids such as methionine (19). Very promising technique is the use of t-RNA synthetase molecules for *in vitro* and *in vivo* translation which resulted in saving in cost and increase in yield (20).

Replacing the natural amino acids with unnatural ones in metalloprotein design has made a great contribution to understanding the role of each amino acid residue and its effect on the activity of the metal center inside the metalloproteins. For instance, it has been shown that the heme iron is most commonly coordinated to histidine in most designed systems. However, introduction of new and unnatural amino acids have proven to be efficient as well but causing changes not only in heme affinity for the peptide but also a significant changes in the reduction potential of the protein (21). Also, replacement of L-amino acids with their D-enanthiometrs can result in changed coordination sphere of metal ion e.g. in three- or four- coordinated Cd(II) complexes in *de novo* designed metalloproteins (22).

Another approach is to incorporate nonnative metal-ions or metal-containing prosthetic groups into *de novo* designed proteins or into native proteins. One way to introduce a nonnative prosthetic group into a native protein is to replace natural with the artificial one. For example, when native heme group is replaced with synthetic isomer such as porphycene it resulted in enhanced O_2-binding ability (23).

2.4 Summary

De novo designed peptides have increased the fundamental understanding of protein-metal interactions in metalloproteins. This technique has been used to mimic many classes of metalloproteins. Designing metal-binding sites in *de novo* designed proteins is the ultimate goal in metalloprotein design and its success is a measure of progress in the field. However, the number of de novo designed scaffolds is very limited compared to number of native scaffolds. Also a fact that nature uses the same scaffold in numerous proteins suggests that they are very modifiable. Discovering how nature is able to achieve this is an important goal of metalloprotein design. Metalloprotein design in native scaffolds can be performed by designing a new metal-binding site or by redesigning an existing one. Incorporation of artificial metal-ions or metal-containing cofactors in proteins has been a way of designing new catalytic systems. The metal-ions or metal-cofactors have been incorporated in proteins that lack a metal site in the native form as well as proteins with native metal sites in which the metal site has been replaced by the new, artificial one.

3 Iron-Sulfur Proteins

3.1 Introduction

Iron-sulfur proteins form one of the largest classes of metalloproteins with more than 160 enzymes and proteins that contain Fe-S centers known today. They are found in all types of organisms and involved in great variety of functions; predominantly electron transfer, catalysis, structure, metabolism of carbon, oxygen, hydrogen, sulfur and nytrogen, sensors for iron and oxygen as well as gene regulation (24).

Broadly defined, iron-sulfur proteins are proteins containing Fe with at least partial S coordination. According to this definition iron-sulfur proteins include proteins containing mononuclear Fe centers coordinated by cysteinyl-S in addition to the large group of proteins containing clusters of Fe bridged by inorganic S which are attached to the protein by amino acid side-chain coordination of Fe-atoms. Also, iron-sulfur proteins can be further classified into simple and complex iron-sulfur proteins. Simple iron-sulfur proteins contain iron-sulfur centers as their only prosthetic group, while complex iron-sulfur proteins contain additional groups such as Mo/W cofactors, flavin, or another type of metal center (24).

3.2 Evolution of Iron-Sulfur Proteins

The existence of iron-sulfur proteins in simple and evolutionary old organisms and their general properties suggest this class of proteins is ancient and has been important in early evolution. This hypothesis has been supported by the fact that they are functionally very diverse. Also, their structural similarities suggested that these proteins share an evolutionary common ancestor, and it has been suggested that this common ancestor is a simple 2 [Fe_4S_4] cluster ferredoxin (25).

Recent theory on the origin of life suggests that life may have originated in deep sea volcanic and hydrothermal vents on the surface of pyrite, FeS_2. These theories suggest that the energy source for this life should be the irreversible and strongly exergonic reaction between FeS and H_2S to form FeS_2 (26; 27). The environment around hydrothermal vents is rich in iron and sulfur, and iron-sulfur proteins may have played an important role in early life. Interesting feature is that both [Fe_4S_4] and to a lesser extent [Fe_2S_2] clusters have been located on the surface of pyrite (26). It has been shown that the clusters can assemble spontaneously in the apoprotein upon addition of iron and sulfur (28). The idea that [Fe_4S_4] clusters are the evolutionary oldest has been supported by several facts. Biomimetic studies of [Fe_4S_4] and [Fe_2S_2] clusters have shown that both clusters can be synthesized, however the [Fe_4S_4] clusters are easier to assemble, and they are often a by-product when synthesizing [Fe_2S_2] clusters (28). Also, theoretical calculations have demonstrated that the [Fe_4S_4] clusters are very robust towards pollution from other metals (29). These properties could have been the advantageous in a primitive world.

3.3 Iron-Sulfur Clusters in Proteins

As mentioned in section 3.1, all ion-sulfur proteins, with the exception of rubedoxin active site, contain clusters of iron atoms and inorganic sulfur linked to the protein by amino acid side-chain coordination of iron atoms. Iron-sulfur clusters can contain from one to

eight iron atoms. The simplest iron-sulfur center contains a single iron atom linked to polypetide by four cysteine residues (see Figure 3.1). The more common iron-sulfur clusters have two, three and four iron atoms coordinated coordinated by polypeptide residues and bridged by inorganic sulfur (see Figure 3.1). By far cysteine is the most common protein ligand, which is in an agreement with the strong affinity of iron for thiolate residues, but a variety of others have been observed (e.g. aspartate in ferredoxin from *Pyrococcus furiosus* (30)). Also, metals other than iron have been located in the cluster (FeMoco in nitrogenase (31)). In general, all iron-sulfur clusters are oxygen sensitive and the stability of iron-sulfur proteins under aerobic conditions depends on the surrounding polypeptide (28). Some iron-sulfur proteins are stable under aerobic conditions for extended periods of time (e.g. *Pyrococcus furiosus* Fd (4)), while others undergo rapid breakdown when exposed to oxygen (28).

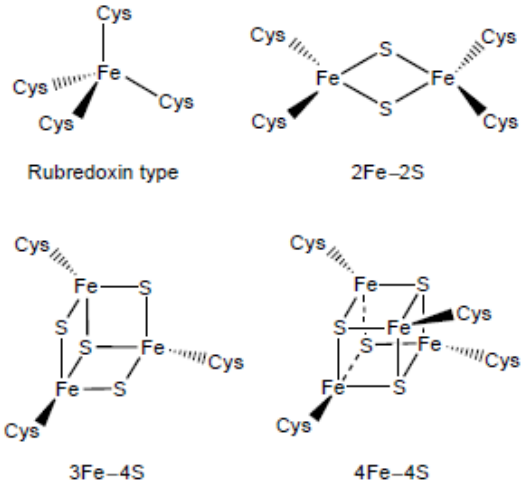

Figure 3.1: The coordination of Fe and S in the four simplest types of Fe–S metalsites of proteins (32). Reprinted with permission.

The range of redox potentials that have been reported for the most common redox states of each of most common types iron-sulfur centers in iron-sulfur proteins are shownin Figure 3.2.

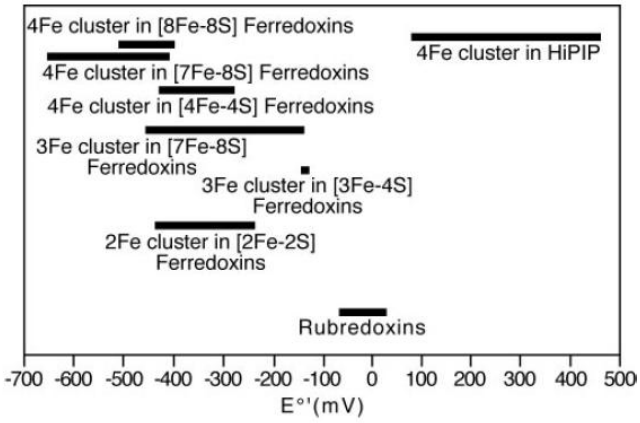

Figure 3.2: Ranges of redox potentials vs. SHE of various subclasses of iron-sulfur proteins (33). Reprinted with permission.

The redox potential can span from 300 to 800 mV for a specific type of a cluster which indicates that protein environment plays an important role in determining the redox

potential. In general, the redox potential value of a metalloptotein results from the intrinsic properties of the metal site combined with its interactions with the protein environment (34). Several factors have been identified to determine the redox potential value – the degree of cluster exposure to the protein surface and to the solvent, the proximity and orientation of the backbone and side-chain dipoles, number and the extent of NH-S hydrogen-bonding interactions, and number and position of hydrophobic residues surrounding the cluster (35).

3.3.1 $[Fe_4S_4] \leftrightarrow [Fe_3S_4]$ Cluster Interconversion

The conversion or degradation of iron-sulfur clusters into other structural type is usually a response to exposure to oxygen or NO, chemical oxidation or reduction, changes in pH, denaturation or site-directed mutations of specific residues. Also, this kind of response can provide a sensory mechanism for regulating gene expression in response to external stimuli (32).

The interconversion between cubane $[Fe_4S_4]$ and cuboidal $[Fe_3S_4]$ cluster is a well-known phenomenon and it occurs via loss or uptake of an iron ion. It is known to occur in certain class of iron-sulfur proteins. Aconitase has been particularly interesting for investigating cluster transformations. When isolated aerobically active $[Fe_4S_4]^{2+/+}$ form of aconitase results in inactive enzyme containing $[Fe_3S_4]^{+}$ cluster. However, under reducing conditions $[Fe_3S_4]^{0}$ cluster readily takes up Fe^{2+} to reform the catalytically active $[Fe_4S_4]^{2+/+}$ cluster (1). Cluster transformation reaction also occurs in some ferredoxins, such as ferredoxin II from *Desulfovibrio gigas* (*D.g.* FdII) (36), *Desulfovibrio africanus* FdIII (*D.a*. FdIII) (37) and *Pyrococcus furiosus* Fd (*P.f*. Fd) (30; 3).

The ease of cluster interconversion seems to be related to the presence of a non-cysteine lligand. In general, iron-sulfur proteins that undergo facile cluster conversion have one non-cysteine ligand coordinating the labile iron site in the $[Fe_4S_4]$ cluster. In a case of aconitase that ligand is water or OH^{-}**,** while for ferredoxins which also easily interconvert that ligand is aspartate (3; 30; 37; 1). Site-directed change of cluster coordinating aspartate to cysteine has been reported to impair the ease with which $[Fe_4S_4]$ converts to $[Fe_3S_4]$ (37). Also, thiolate (RS^{-}) is a stronger ligand for Fe^{2+} than carboxylate $RCOO^{-}$, therefore replacement of aspartate ligation by cysteine would be expected to lead to a more inert $[Fe_4S_4]$ cluster. By contrast to other systems, ferredoxin from *Desulfovibrio gigas* (*D.g.* Fd) has all-cysteine ligation of the iron-sulfur cluster but it still can easily interconvert (36).

3.4 *Pyrococcus furiosus* Ferredoxin and Its D14C Mutant

Pyrococcus furiosus (*P.f.*) is a hyperthermophilic archaeon that has a growth optimum at 100 °C and it was originally isolated from submarine volcanic areas (3). One of the first proteins purified from this organism is a small ferredoxin (Fd) that is used for electron transfer in metabolism (30). The *P.f.* ferredoxin is one of the most termostable ferredoxins ever characterized. It remains with unchanged activity and UV-vis absorption after 12 hours of incubation at 95 °C under anaerobic conditions (3). It functions as an electron acceptor for glyceraldehyde-3-phosphate oxidoreductase and pyruvate oxidoreductase and an electron donor for a membrane-bound hydrogenase complex and sulfide dehydrogenase (38). It consists of 66 amino acid residues and a single iron-sulfur

cluster in its active center (30). Three out of five cysteine residues in the protein coordinate the [Fe_4S_4] cluster, while the two remaining cysteine residues form a disulfide bond (39). The fourth ligand coordinating the [Fe_4S_4] cluster is aspartate (30). Aspartate ligation of an iron site as opposed to the usual all-cysteinyl ligation of a cluster makes this protein one of two ferredoxins containing a single [Fe_4S_4] cluster with this type of coordination. Under oxidizing conditions [Fe_4S_4] cluster readily converts to [Fe_3S_4] cluster where the labile iron is the one originally coordinated to the aspartate (30).

In early studies has been reported that *P.f.* Fd exist as a monomer (30), however, it has been suggested later that a monomer/dimer equilibrium exists depending of the protein solution ionic strength and that at physiological ionic strength, approximately 0.35 M NaCl, the protein is predominately a dimer (40).

In the following sections the differences between the native *P.f.* Fd and its D14C mutant concerning their spectroscopic and electrochemical properties will be pointed out.

3.4.1 Spectroscopic Properties

Figure 3.3 shows the ultraviolet-visible (UV-vis) absorption spectra of the [Fe_4S_4] and [Fe_3S_4] WT *P.f.* Fd and the [Fe_4S_4] D14C *P.f.* Fd. The absorbance maximum for [Fe_3S_4] WT *P.f.* Fd is at 408 nm, while both D14C Fd and WT Fd containing the [Fe_4S_4] cluster have the absorbance maxima at 390 nm (41; 42). Because of the additional Fe-S charge transfer band, the [Fe_4S_4] D14C Fd shows an increased absorbance ratio (A_{390}/A_{280}) compared to the [Fe_4S_4] WT Fd (0.73 vs. 0.57). This manifests in an increase in extinction coefficient of the D14C Fd as compared to WT Fd – ε_{390} = 20.2 mM^{-1} cm^{-1} vs. ε_{390} = 17.0 mM^{-1} cm^{-1}, respectively (41; 43).

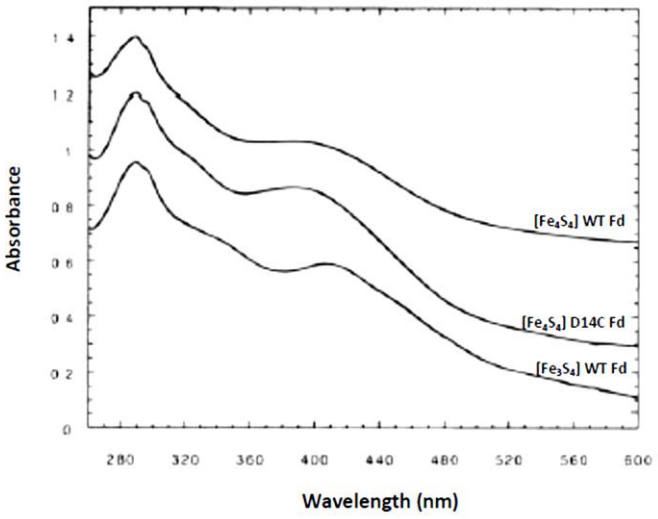

Figure 3.3: The UV-vis spectra of [Fe_4S_4] WT *P.f.* Fd, [Fe_3S_4] WT *P.f.* Fd and [Fe_4S_4] D14C *P.f.* Fd. Modified from (42). Reprinted with permission.

The [Fe_4S_4] cluster can be stabilized in two oxidation states: $[Fe_4S_4]^{2+}$ and $[Fe_4S_4]^{+}$. In the oxidized state two delocalized $Fe^{2.5+}$-$Fe^{2.5+}$ pairs are anti-ferromagnetically coupled forming a ground spin state S = 0. In the reduced form the delocalized pair $Fe^{2.5+}$-$Fe^{2.5+}$ is anti-feromagnetically coupled to the Fe^{2+}-Fe^{2+} pair forming a total spin S = 5/2 (33). The EPR spectra of dithionite-reduced form of [Fe_4S_4] WT *P.f.* Fd and [Fe_4S_4] D14C *P.f.* Fd

are shown in Figure 3.4. The reduced form of the $[Fe_4S_4]$ WT *P.f.* Fd exist as a mixture of S = 1/2 (20 %) and S = 3/2 (80 %) ground states (30). As seen from the Figure 3.4 (a) the reduced form of the $[Fe_4S_4]$ WT *P.f.* Fd has a broad rhombic signal centered at g ~ 1.94 which originates from S = 1/2 ground state, and a low-field resonances near g ~ 5 from S = 3/2 ground state. The reduced $[Fe_4S_4]$ D14C *P.f.* Fd gives much sharper signal at g ~ 1.94 (see Figure 3.4 (b)). This implies that the reduced $[Fe_4S_4]$ D14C *P.f.* Fd has a pure S = 1/2 ground state which is commonly seen in the $[Fe_4S_4]^+$ clusters with complete cysteinyl coordination (41; 44).

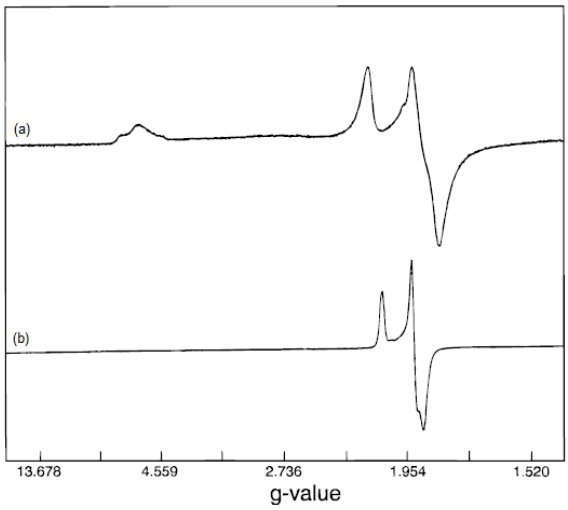

Figure 3.4: EPR spectra of the reduced forms of native and D14C mutant of *P.f.* Fd. The samples were (a) native *P.f.* Fd and (b) D14C mutant; T = 8 K; P = 10 mW; M = 0.2 mT; v = 9.57 GHz; G = $8 \cdot 10^3$. Modified from ref (41). Reprinted with permission.

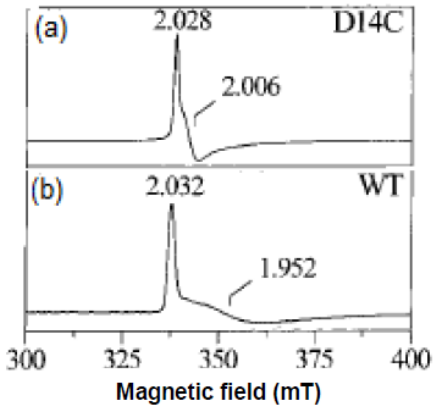

Figure 3.5: X-band EPR spectra of the $[Fe_3S_4]^+$ cluster in (a) D14C and (b) WT *P. f.* Fd; T = 4.2 K P = 1 mW; v = 9.60 GHz; and M = 0.63 mT. Modified from ref (43). Reprinted with permission.

The $[Fe_3S_4]$ cluster can be stabilized in two oxidation states: $[Fe_3S_4]^+$ and $[Fe_3S_4]^0$. In the oxidized state, the three high-spin Fe^{3+} atoms (S = 5/2) are antiferromagnetically coupled, forming a ground electronic state with S = 1/2. One-electron reduction gives an S = 2 state, resulting from the antiferromagnetic coupling between a delocalized $Fe^{2.5+}$-$Fe^{2.5+}$ pair (S = 9/2), that share the incoming electron, and a highspin Fe^{3+} site (S = 5/2). The EPR spectra of $[Fe_3S_4]^+$ cluster in WT and D14C mutant of *P. f.* Fd are shown in Figure 3.5. The ground state of the cluster is S = 1/2, however, the EPR spectra of the

two Fds exhibit differences in the width of the resonance; the D14C mutant has narrower resonance while the WT has much broader (43).

3.4.2 Electrochemical Properties

The formal potential of $[Fe_4S_4]$ D14C *P.f.* Fd is more negative than $[Fe_4S_4]$ WT *P.f.* Fd, as shown in Table 3.1. This is consistent and readily explained by the pK_a values of the residue 14, where Asp (4.0) < Cys (8.5). Therefore, Asp is a better electron withdrawing group compared to Cys and thus stabilizes the reduced cluster (41; 42). A reduction potential for the $[Fe_3S_4]$ form of D14C *P.f.* Fd has not been reported yet.

Table 3.1: Formal potentials of $[Fe_4S_4]$ and $[Fe_3S_4]$ WT *P.f.* Fd and $[Fe_4S_4]$ D14C *P.f.* Fd. Potentials are given in mV vs. SHE (42).

P.f. Fd variant	$E^{0'}$
$[Fe_4S_4]$ WT	-368
$[Fe_3S_4]$ WT	-203
$[Fe_4S_4]$ D14C	-426

3.5 Incorporation of Exogenous Metals in *Pyrococcus furiosus* Ferredoxin

Catalytically active iron-sulfur proteins have been found to be based on a $[Fe_4S_4]$ structural unit that lacks cysteinyl ligation at the specific site and/or with a specific iron replaced with with another transition metal. Aconitase is the best example of the former, while nitrogenise is the best example of the latter type of active site (1; 2). A great potential of heterometalic centers to participate in enzymatic catalysis has stimulated the synthesis of these novel, artificial heterometalic clusters. Holm and co-workes have synthesized and characterized numerous non-protein analogues of heterometallic $[M\text{-}Fe_3S_4]$ clusters (M = Ni, Nb, Mo, W, Re, V, Co, Zn, Tl, Cu, Ag) (45). The ability of biological $[Fe_3S_4]$ clusters to take up metal lead to the formation of $[M\text{-}Fe_3S_4]$ clusters in ferredoxins.

The first heterometallic cluster synthesis in a protein ever reported was in 1986 for the formation of a $[Co\text{-}Fe_3S_4]$ cluster in *D.g.* FdII (46). The stability of *P.f.* Fd as well the lability of the fourth iron has made this protein very attractive for studies involving the formation of heterometallic clusters $[M\text{-}Fe_3S_4]$, where M is a metal ion other than iron. $[M\text{-}Fe_3S_4]$ clusters in *P.f.* Fd have been constructed with various metal ions, mainly divalent, M = Cr^{2+}, Mn^{2+}, Co^{2+}, Ni^{2+}, Cu^{2+}, Zn^{2+}, Cd^{2+} and Tl^{+} (47; 48; 49; 50).

All clusters were created by incubation of the reduced $[Fe_3S_4]$ Fd with the metal ion and in some cases subsequent removal of excess metal and additives by size exclusion chromatography. The ground spin state of heterometallic cubane clusters $[MFe_3S_4]$ can be rationalized by anti-ferromagnetic coupling between the high-spin metal ion, M, and the appropriate cluster fragment, i.e. $[Fe_3S_4]^{+}$ (S = 1/2), $[Fe_3S_4]^{0}$ (S = 2) or $[Fe_3S_4]^{-}$ (S = 5/2) (49). As suggested, the redox chemistry is being confined in the cluster fragment (49; 50). The trend of formal potentials of $[M\text{-}Fe_3S_4]^{2+/+}$ clusters is shown in Figure 3.6. The heterometallic clusters with potential higher than $[Zn\text{-}Fe_3S_4]$ have heterometal capable of reduction over the physiological potential range with accessible $M^{2+/+}$ couple

and by withdrawing electrons they minimize the negative charge on the cluster fragment. The opposite affect are having metals which are only capable of oxidation over the physiological potential range (49; 47).

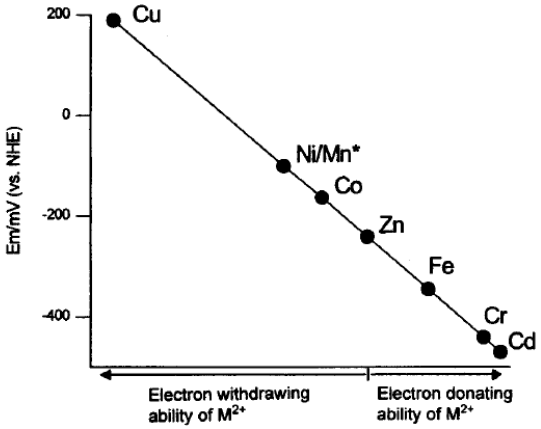

Figure 3.6: Plot of the formal potential of $[M\text{-}Fe_3S_4]^{2+/+}$ in *P.f.* Fd as a function of the metal M. *Only lower limits are available for the midpoint potentials of $[Ni\text{-}Fe_3S_4]^{2+/+}$ and $[Mn\text{-}Fe_3S_4]^{2+/+}$ as oxidation at higher potentials leads to a loss of M (47). Reprinted with permission.

4 Mass Spectrometric Analysis

During the last decade, mass spectrometry (MS) has progressed rapidly and has emerged as a major analytical tool in molecular-level biological research. Today, MS is the most sensitive method for the structural characterization of biomolecules. It is nowadays a widespread technique with a key role in numerous fields such as biochemistry, pharmacology, biotechnology, microbiology, and etc. This development is a direct consequence of the introduction of the "soft ionization" methods of electrospray ionization (ESI) and matrix-assisted laser-desorption-ionization (MALDI). These ionization methods have made it possible to ionize large, thermally labile biomolecules and transfer them to the gas phase without dissociation. Furthermore, biomolecules can nowadays be analysed in the mega-Dalton (MDa) range.

4.1 Introduction to Mass Spectrometry of Intact Metalloproteins

Four basic components are standard in all mass spectrometers: a sample inlet, an ionization source, a mass analyzer and an ion detector. A mass spectrometer determines the mass of a molecule by measuring mass-to-charge ratio (*m/z*) of the molecular ions. Once formed, ions are electrostatically directed into a mass analyzer where they are separated according to *m/z* and finally detected. The result of molecular ionization, ion separation, and ion detection is a spectrum.

4.1.1 Electrospray Ionization (ESI)

Mass spectrometer measures the mass-to-charge ratio of ionized molecules in the gas phase. Therefore, the analytes need to be ionized and transferred into the gas phase prior to analysis. A variety of ionization techniques are used for mass spectrometry. Some ionization techniques are very energetic (e.g. electron ionization, chemical ionization, field ionization) and cause extensive fragmentation of analyte molecules. Other techniques are softer (e.g. electrospray ionization, matrix-assisted laser-desorption-ionization, plasma desorption, fast atom bombardment) and only produce ions of the molecular species. These soft ionization techniques are revolutionizing methods that have made MS one of the most important tools to analyse large biomolecules. In this section the focus will be on the soft ionization technique ESI as the source to generate the gas-phase ions. In particular, ESI has proven to be the most appropriate method for analysis of intact proteins and non-covalent protein complexes.

Electrospray ionization is an atmospheric-pressure ionization method that produces small charged droplets from a liquid medium by applying an electric field. The process itself originates from the work of Dole et al. in 1968 (51) but it was Fenn's group that coupled ESI with MS in 1984 (52). In 2002 J. B. Fenn was awarded for his achievement with the Nobel Prize in Chemistry.

There are three major steps in the ESI process (53; 54; 55). The first step is production of charged droplets from an analyte dissolved in a solvent. Second step is shrinkage of charged droplets by solvent evaporation and repeated droplet fissions ultimately leading to very small, highly charged offspring droplets capable of producing gas-phase ions. The third step is the mechanism by which gas-phase ions are produced.

In conventional electrospray a diluted solution of analyte is pumped through a thin capillary at a low flow rate (µL/min). A high voltage (2-5 kV) is applied to the capillary, and depending of the analyte, the applied voltage can be positive or negative. The potential difference is applied between the capillary and the counted electrode (the inlet of the mass spectrometer). Figure 4.1 illustrates the ESI process in the positive ion-mode where, by applying positive voltage, positively charged ions accumulate at the liquid surface at the end of the capillary while negatively charged ions migrate towards the positive capillary wall.

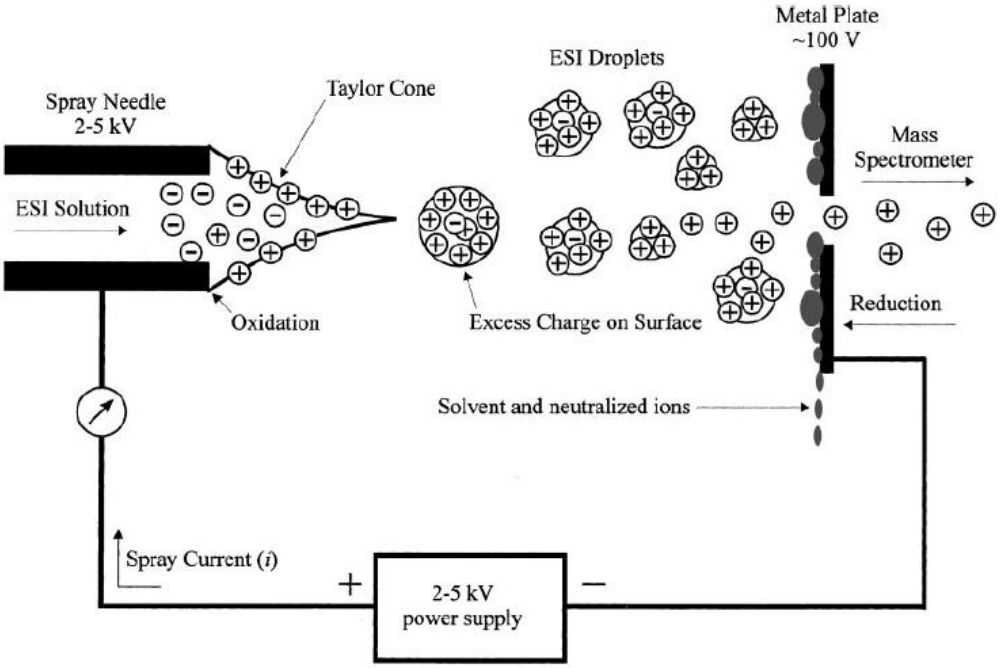

Figure 4.1: A schematic overview of electrospray ionization process (56). Reprinted with permission.

The accumulated positive charge at the tip leads to destabilization of the surface because the positive ions are drawn downfield but cannot escape from the liquid. Due to the repulsive coulombic forces between the positive ions, the liquid surface is drawn out such that a cone-like shape forms, which is called a Taylor cone (53). Under the high electric field, the repulsive forces become stronger than the surface tension at the tip of the cone, and a liquid mist of charged droplets is ejected. Both a pressure and a potential gradient will direct droplets towards the inlet of mass spectrometer.

As the solvent from the droplet evaporates, the droplets decrease in size while the charge remains the same. They will shrink until the radii are sufficiently close to the Rayleigh limit:

$$q = 8\pi(\varepsilon_0 \gamma R^3)^{½} \tag{4.1}$$

where q is a charge and R is radius of a droplet, ε_0 is the permittivity of the vacuum, γ is the surface tension of the solvent (55). When the Coulombic repulsion between the charges exceeds the cohesive force of the surface tension, the droplets become unstable and undergo Coulombic fission into smaller offspring droplets (55). The emitted stream of offspring droplets caries about 2 % of the mass of the parent droplet but about 15 % of the parent's charge, and the radius is roughly one-tenth of the radius of the

parent (53). This process continues until the droplets with diameter in the nanometer range are generated, and thus they become gas-phase ions emitters (53).

The ESI source functions as an electrolysis cell. In the positive ion-mode oxidation reactions occur at the liquid-metal interface of the capillary tip while reduction reactions occur at the negative counter electrode (see Figure 4.1) (57). These electrochemical reactions, which maintain the charge balance, allow continuous production of charged droplets (57).

The formation of gas-phase ions from the small, highly charged droplets is not yet fully understood. However, two mechanisms have been proposed: Dole's theory, referred to as the charge-residue model (CRM) (51), and Iribarne and Thompson's theory, the ion-evaporation model (IEM) (58). The CRM suggests that the solvent evaporates and the droplet breaks up until it contains a single analyte ion. Solvent evaporation from a charged droplet will lead to conversion of the droplet to a gas-phase ion by retaining the charge of the droplet (51). Iribarne and Thompson suggested alternative mechanism in which they proposed that droplets with radius less than 10 nm can allow direct emission of gas-phase ions, and the charge state of the ion will depend on the number of the charges that are transferred from the droplet surface to the ion (58). The exact mechanism of a gas-phase ion formation from the charged droplet is still under debate. However, experimental results suggest that the formation of gas-phase ions from small molecules occurs through IEM, while CRM may account for the formation of ions from large globular proteins (55; 59; 60).

The conventional electrospray operates typically at a flow rate of 1 – 10 µL/min, and the diameters of initially formed droplets are in µm size (53). In general, the ESI process shows a very poor tolerance for buffers and salts present in the solutions which are most often used for protein storage and during protein purification. They are largely non-volatile and during ESI cause suppression of ionization or/and intensive adduct formation. Since its introduction ESI has gone under major developments. Miniaturisation of the ESI source has been one of the key steps in its development towards higher sensitivity and tolerance to salts (61; 62). The first ESI source without continuous flow was developed in 1994 operating at low nL/min flow rates, and it is called nano-electrospray (nano-ESI) (62). Another modification that has made ESI source more tolerant to salts is the Z-spray configuration (63).

4.1.1.1 Nano-electrospray (nano-ESI)

The nano-ESI source was designed by Wilm and Mann (62) in 1994. In this approach the sample is sprayed from metal-coated capillaries, with an orifice diameter of 1 – 2 µm, which are installed with a backing gas pressure to aid flow stability. Basically, the flow is determined by the ESI process itself (62). This resulted in very low flow rates of 20 – 50 nL/min. As a direct consequence, smaller sample volumes are required – typically 1 – 2 µL. In contrast to the conventional ESI source, the primary droplets size are much smaller – in (62) authors assume a value of < 200 nm.

Due to the production of smaller droplets, the ionization efficiency that is achieved by nano-ESI source is estimated to be app. two orders of magnitude higher than using the

conventional ESI source (62). Also, the tolerance towards salt contamination (buffers, etc.) has proven to be higher by one order of magnitude (64).

4.1.1.2 Z-spray configuration

In this set-up the spraying device is mounted at the perpendicular angle to the inlet of the mass spectrometer resembling a flattened Z-shape, and hence the name Z-spray (63).
In a conventional ESI source the ions generated travel along an approximately straight line trajectory (see Figure 4.2(a)) from formation to entering the analyzer. Ions are also being accompanied by a small number of neutral molecules which will strike the edges of the skimmer and accumulate here. The idea in a Z-spray configuration is for ions and neutral molecules to follow different paths. Ions will be drawn into the mass analyzer after most of the solvent has evaporated, while neutral molecules will travel in a straight line and hence not be analyzed (see Figure 4.2(b)) (63). With the Z-spray design the instrumental sensitivity and performance remain constant over longer period of time.

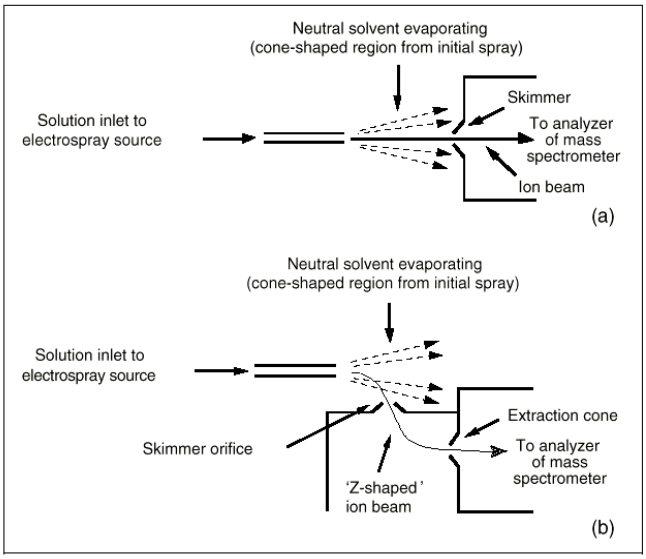

Figure 4.2: (a) The trajectory of analyte ions from a conventional ESI. (b) The trajectory of analyte ions from a Z-spray source (63). Reprinted with permission.

4.1.1.3 Appearance of ESI Mass Spectra and Data Interpretation

The ESI process produces multiply charged ions of the same protein molecule due to protonation of the basic sites (in positive ion-mode) or deprotonation of acidic sites (in negative ion-mode) denoted as $(M + zH)^{z+}$ and $(M - zH)^{z-}$, respectively (65). The data in a spectrum are presented as a relative population of different charge states of the molecule separated according to their *m/z*-ratio. This spectrum is often referred to as multiply charged or *m/z* spectrum. An example of multiply charged spectrum is given in Figure 4.3. From this spectrum it is possible mathematically to calculate the molecular mass of the analyte molecule by using a simple algorithm for two adjacent peaks differing by one charge state:

$$m_1 = \frac{M - z_1 M_{H^+}}{z_1} \qquad (4.2)$$

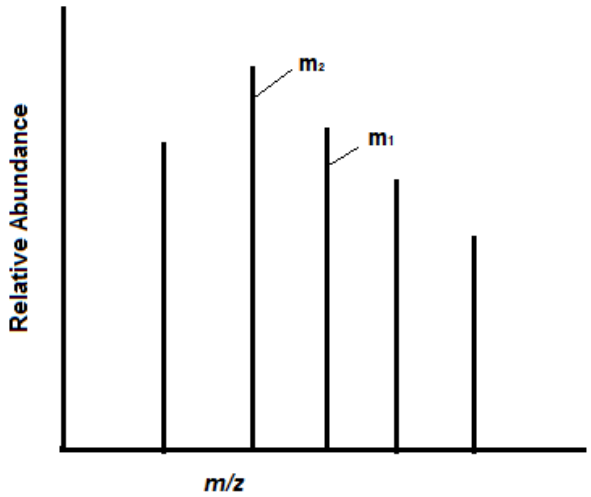

Figure 4.3: A hypothetical multiply charged spectrum.

$$m_2 = \frac{M - z_2 M_{H^+}}{z_2} = \frac{M - (z_1+1) M_{H^+}}{z_1 + 1} \tag{4.3}$$

where m_1 and m_2 are *m/z* values of two adjacent peaks in the spectrum with the charge states z_1 and z_2 where $z_2 = z_1 + 1$, the molecular mass of an analyte is M and M_{H^+} is the mass of a proton. Solving the equations 4.2 and 4.3 for z_1 gives equation 4.4 for negative ion mode:

$$z_1 = \frac{m_2 + M_{H^+}}{m_2 - m_1} \tag{4.4}$$

Substitution of this value in equations 4.2 or 4.3 gives the value for the molecular mass of an analyte, M. This process can then be repeated for different pairs of adjacent charge states from the spectrum differing by one charge state, and hereafter the mass is determined by averaging these masses. Using this algorithm the *m/z* for the multiply charged ion is converted to the mass of the zero-charged molecule (66). This common algorithm assumes that all charge present on an ion is due to an excess of protons in positive ion-mode or a deficit of protons in a negative ion-mode. This assumption is true for the apo-proteins while for the metalloproteins additional considerations need to be taken into account (see section 4.1.1.4).

4.1.1.4 Interpretation of ESI Spectra for Metalloproteins

Metalloproteins are very interesting targets for mass spectrometric analysis since the stoichiometry and oxidation state of the metal or metal-cluster can be determined from mass spectrometric data even though the information that are sought are determined by measuring a relatively small change in a molecular mass of the protein. As mentioned in section 4.1.1.3, the molecular mass for a protein is calculated assuming that all ionizable sites in its amino acid sequence are neutral. This rule is not acceptable in a case of metalloproteins since they contain a metal or a metal-cluster in an oxidation state other than zero, and using this rule would result in calculating molecular masses for metaloprotein that vary with the oxidation state of a metal or a metal-cluster (66; 67; 68). To avoid this problem, some basic terms/principles has to be defined in order to properly assign a molecular mass from the mass spectrometric data.

The first term is the **calculated mass** which is defined as the sum of the average molecular masses of all amino acids present in the protein sequence plus the average atomic mass of a metal or a metal-cluster components (as if they have an oxidation state zero) present in the metalloprotein (69). By calculating the molecular mass in this manner it is also assumed that no disulfide bonds are present. The second term is the **apparent mass** which is calculated directly from experimental data using the algorithm given by equation 4.2 and 4.3 assuming that all the charge present on an ion is due to an excess or a deficit of protons depending on whether it is a positive or a negative ion-mode, respectively (66). These equations overestimate the number of protons providing the charge to the ion. By calculating the difference between the calculated and the apparent mass this method allows determination of the oxidation state of the metal or metal-cluster and the number of disulfide bonds present in the metalloprotein (66). The apparent mass will be lower than the calculated by the mass of the protons equal in number to the oxidation state of the metal center minus the mass of two protons for each disulfide bond present (66). The third term is the mass that takes the oxidation state of the metal or metal-cluster and the number of disulfide bonds present into account; it is named the **expected mass**. This is the mass that should be compared with the apparent mass in order to properly assign the molecular mass of the metalloprotein from the mass spectrometric data.

4.1.1.5 Important Experimental Variables

As mentioned previously, gentleness of the ESI process allows analysis and detection of intact proteins and non-covalent protein complexes. From an experimental point of view, the successful ESI mass spectrometric analysis includes maintaining the solution conditions such that the protein keeps its native, folded state, and efficient desolvation of charged droplets generated by the ESI process (70).

Most common buffers which are used during protein purification or storage contain salts which are not volatile. Therefore, during the ESI process these salts cause suppression or/and extensive adduct formation. As mentioned earlier, the use of nano-ESI has provided an improvement in sensitivity for salt containing solutions over that obtained for conventional ESI (64). However, high salt concentration can cause background that interferes with the detection of an analyte, which sometimes can be so severe that it completely masks the analyte signal (56). Also, glycerol and detergents present in a protein solution are normally not compatible with the ESI process. Therefore, most of the protein solutions need to be buffer exchanged prior MS analysis. This step is probably the most critical one which will determine whether the analysis will be successful or not (71). Organic solvents, such as methanol or 1:1 water:acetonitrile are used for studying small molecules and in proteomics. However, for studying intact proteins this kind of conditions are not acceptable since they would denature the protein (71; 72). Therefore, the use of appropriate solvents (usually water), pH values and ionic strength are necessary to maintain the protein intact. The most commonly used volatile, aqueous buffered solution is ammonium acetate with a pH of 6 – 8 since both ammonia and acetic acid are volatile and evaporate readily during the ESI process (73). It has also been reported that addition of high levels of ammonium acetate can improve the analyte signal by reducing the effect of non-volatile buffer components (73; 74). The concentration of ammonium acetate solution used for buffer exchange can vary – a starting range from 100 mM to 1 M is typical, although its ability to overcome the presence of contaminating

buffer salts has led to a routine use of up to 1 M to 3 M ammonium acetate (71). However, there are certain facts to consider when increasing the ammonium acetate concentration. It has been observed that by increasing its concentration the intensity of the higher protein ions charge states in *m/z* spectrum decreases while the intensity of the lower charge states increases (74). This can be explained due to the conformational effect at high ionic strength or the competition for charge between the protein and ammonium acetate. Interestingly enough, sodium adducts formation, arising from sodium which is almost always present in the protein solutions as a contaminant, increases with decreasing the charge state of a protein ion (74). This has been explained assuming that different charge states are formed from droplets that have undergone different extents of evaporation. High charge state protein ions originate from the early stages of the chain of droplet evaporation/fission when the concentration of sodium at that stage is low and similar to the one of the bulk solution. Lower charge states originate from droplets that have gone extensive evaporation and therefore have increased sodium concentration (64).

Desolvation of droplets generated by ESI is a critical parameter for direct observation of intact proteins and non-covalent protein complexes. The aim is to find the optimal conditions that strip away water and buffer components without causing protein subunits to dissociate. Obtaining higher peak intensities, narrower peak widths and a reduced number of adducts per charge state brings the observed *m/z* value of the protein ion charge state closer to its theoretical value. Broader peaks in the mass spectrum complicate the measurement of molecular mass. Physical methods used to remove solvated molecules include heating the capillary inlet and by gas phase collisions in the interface region downstream from the atmospheric pressure (70). In addition to desolvation, collisions in the transfer ion guide also affect the focusing of ions improving the transmission to the analyzer. As mentioned in section 4.1.1, gas-phase ions are generated at atmospheric pressure and introduced into the vacuum region by acceleration acquiring large amount of energy (75). This will result in broaden ion beams leading to the loss of transmission. Using the higher pressure in the initial stages of the instrument will result in more collisions with the gas molecules eventually resulting in focusing of the ion beam. This phenomenon is known as collision cooling (75).

4.1.2 Time-of-Flight Mass Analyzer

When ions have been formed in the source, they are transmitted to the analyzer region where they are separated according to their mass-to-charge ratio. There are a number of mass analyzers available today: magnetic sector, time-of-flight (TOF), quadrupole, ions traps, orbitrap, and ion cyclotron cells with Fourier transformation. All mass analyzers use static or dynamic electric or magnetic fields that can be alone or combined. The basic differences between the various types of mass analyzer lie in the manner in which such fields are used to achieve separation.

At present, the mass spectrometric analysis of biomacromolecules is mainly the domain of the TOF mass spectrometry. Its large application is not only due to theoretically unlimited *m/z*-range but also because of the high sensitivity, resolution and speed of TOF analysis. The focus in this section will be on the TOF mass analyzers since this system presents an ideal candidate for coupling with the ESI source.

The first concept of TOF analyzer was described by Stephens in 1946 (76) while in 1955 Wiley and McLaren published the paper with description of a linear TOF mass spectrometer which later became the first commercial instrument (77).

The operating principle of the TOF analyzer involves measuring the time it takes for an ion to travel from an ion source to a detector. Ions are formed in the source and hereafter accelerated towards the field-free region, acquiring the same amount of kinetic energy ($E_k = \frac{mv^2}{2}$). When they enter the field-free region they are separated according to their velocity which is a function of their *m/z* values. Their *m/z* ratios are determined by measuring the time it takes for an ion to reach the detector. When leaving the source, an ion with the mass m and a charge $q = ze$ is accelerated by potential V_a. Since the potential energy of an ion is equal to kinetic energy, the mass-to-charge ratio is related to the ions flight time by the following:

$$\frac{mv^2}{2} = zeV_a \tag{4.5}$$

$$v = \left(\frac{2zeV_a}{m}\right)^{½} \tag{4.6}$$

where e is the charge of an electron, V_a is the acceleration voltage, m is the mass of an ion and z is the number of charges. The time needed for an ion to travel the distance L through the field-free region, also called the drift time, is given by the equation 4.7:

$$t = \frac{L}{v} = L\left(\frac{m}{2zeV_a}\right)^{½} \tag{4.7}$$

This equation shows that *m/z* is proportional to the drift time of an ion, and that the light ions will reach the detector earlier than heavy ions even if they carry the same number of charges. This equation also implies that there is no theoretical limit to the upper *m/z* value that can be detected – it is a matter of how long it takes for an ion to arrive at the detector. In practice however, the sensitivity needed to detect a very slow moving large molecular weight compound limits the TOF-MS to 1-2 million Da or so (78).

The resolving power of the TOF analyzer has always been problematic. In theory all ions leaving the source with the same *m/z* should have the same kinetic energy. Also, the position from where the ions start when they are pulsed out of the source should be the same. However, in practise this is not the case and thus decrease in resolving power of the TOF analyzer is observed. In order to improve the resolving power an ion mirror can be used to reflect ions with the same *m/z* values that have different energies. An ion mirror, also known as a reflectron, is an electric field that can refocus and reflect ions towards the detector. Ions with more kinetic energy and hence more velocity will penetrate into the reflectron more deeply than ions with lower kinetic energy. Ions with the same *m/z* value are then focused. In addition, incorporation of the reflectron increases the flight path which also has a positive effect on resolving power. Today commercially available TOF analyzers can be a V-shaped with one reflectron or a W-shaped with additional ion mirror (see Figure 4.4) which doubles the instrument's

resolution. However, increased resolution is at the expense of sensitivity – the instrument in a W-mode has 3 times less sensitivity than in a V-mode (65).

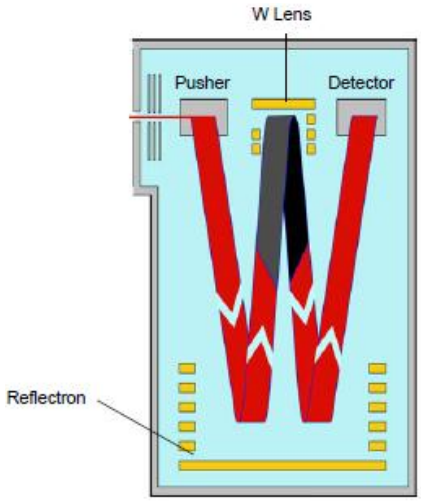

Figure 4.4: Ion – optics in a W-mode (79).

Another important consideration of the TOF mass spectrometer is its requirement for high vacuum. Since ion beams generated in the ions source need to travel a distance of 1 to 2 meter to reach the detector there is a high probability of ions encountering neutral molecules (65). In order to decrease the number of these interactions and number of neutral species, a higher vacuum is required in the TOF mass spectrometer than in other instruments. This is achieved by using a turbo pump.

The TOF analyzers have a pulsed nature and they are directly compatible with pulsed ionization techniques such as MALDI. In order to take the advantage of TOF analyzers it would be very useful to combine them with continuous ionization techniques such as ESI. It is now well established that the orthogonal injection, also known as orthogonal acceleration (oa), is the best technique for coupling continuous ionization sources with TOF analyzers (65). Beam of ions generated in the ion source of these instruments travel in a direction perpendicular to the axis of the flight path of the TOF. Most instruments that have orthogonal acceleration also have the reflectron, too.

4.2 Instrumentation

Mass spectrometric analysis of intact metalloproteins was performed on a LCT Premier mass spectrometer (Waters). The schematic overview of the instrument is given in Figure 4.5. The LCT Premier features a Z-Spray source with nano-ESI ionization, and the oa-TOF mass analyzer with the *m/z* range up to 30 000 (79). Ions generated in the source are transferred to the analyzer via two ion guides and a hexapole which do not allow mass selection of the ions but only transmit and focus the whole ion beam. They also serve as an interface region between the high pressure at the ESI source front end and the high vacuum of the TOF region (79).

The vacuum system is made of three vacuum pumps – two rotary pumps maintaining the pressure in the ion source and ion guide one and also providing a backing for the turbo pump which pumps the ion guide two, the hexapole and the TOF region. From the

pusher to the detector ions are separated in mass according to their flight times. Dual microchannel plate detector assembly (MCP detector) is used as a detector (79). The instrument offers and option of operating in a V- or a W-mode and each of them in a negative or a positive ion-mode. The instrument is controlled and data acquired using the MassLynx™ v4.1 software system provided with the instrument (79).

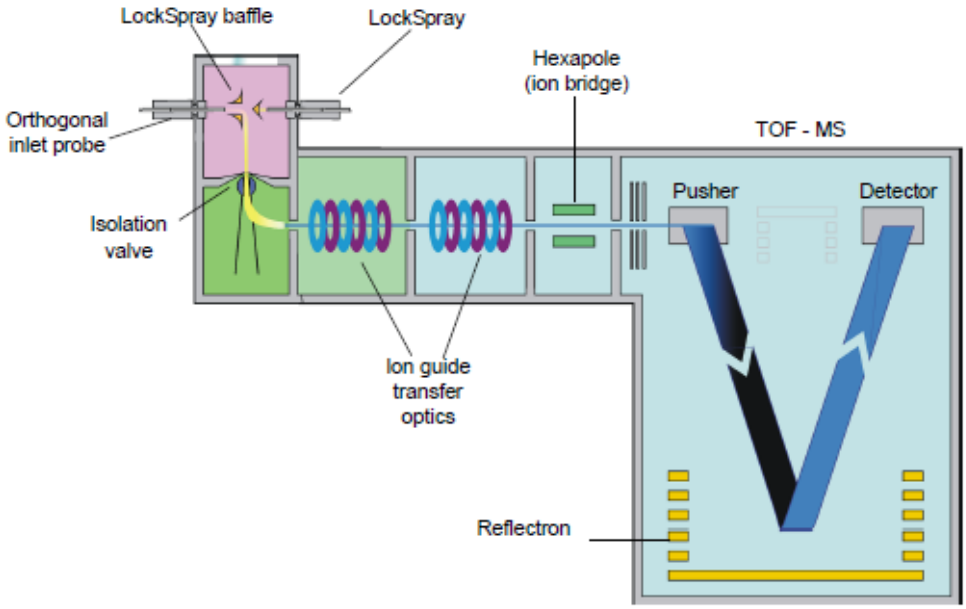

Figure 4.5: Schematic overview of LCT Premier mass spectrometer (Waters) in a V-mode (79).

4.3 Mass Spectrometric Measurements

All spectra from this project were recorded using the LCT Premier mass spectrometer (described in section 4.2) in negative ion-mode. The instrument was calibrated using 2 mg/ml NaI in 50% isopropanol solution in the *m/z* range from 600 to 4000. All protein samples were sprayed from Au/Pd-coated capillaries (Proxeon). In all experiments the following instrumental parameters were used: the source temperature was maintained at 50 °C, applied capillary voltage was typically between 800 and 900 V while applied cone voltage was 50 V with the cone gas maintained at 20 L/h. The software MassLynx™ v4.1 (Waters) equipped with the MaxEnt1 algorithm was used to produce mass spectra from the observed *m/z*-data.

4.3.1 Sample Preparation

Prior to mass spectrometric analysis all protein samples were desalted, and the buffer was exchanged into 100 mM NH_4Ac using the Micro Bio-Spin P-6 Chromatography Columns (Bio-Rad). Samples were diluted to protein concentration of approximately 20 µM. In the case of $[Fe_3S_4]$ D14C *P.f.* Fd, purified using the procedure given in section 5.2.3, the protein was sprayed from 100 mM NH_4Ac/HAc pH 5.8. All protein samples containing artificial ferredoxins were prepared inside the glove box. Also, metal-coated capillaries were loaded inside the glovebox.

4.3.2 Data Acquisition and Analysis

Data were acquired using the MassLynx™ v4.1 software system. Due to the limited resolving power of the instrument average mass was used both for the expected and the

apparent mass. Due to adduct formation observed for the lower charge state protein ions, for calculating the mass spectrum from the obtained *m/z* data in the experimental data presented in the following chapters only the high charge state protein ions are taken into account (see section 4.1.1.4). The apparent mass was calculated from the obtained data using the principle described in section 4.1.1.3. As explained in section 4.1.1.3, the apparent mass is calculated for the zero-charged molecule where all the charges present are assumed to be due to the deficit in protons (in a negative ion-mode) which is not true for metalloproteins. Therefore, the apparent mass needs to be compared with the expected mass which takes into account the oxidation state of the metal or metal-cluster and the number of disulfide bonds present. To determine the expected mass the oxidation state of the metal cluster and the number of disulfide bonds needs to be subtracted from the calculated mass. The expected masses of all ferredoxins which were analyzed by mass spectrometry in this project are given in the Table 4.1.

Table 4.1: Calculated and expected average molecular masses for both WT *P.f.* Fd and its variant D14C containing different clusters.

Name	Calculated mass (Da)	Corrections	Expected mass (Da)
apo-WT *P.f.* Fd	7167.08	for S-S -2.02	7165.06
[Fe_4S_4] WT *P.f.* Fd	7518.73	for S-S -2.02; -1.01/-2.02 for the cluster	7515.70/7514.69
[Fe_3S_4] WT *P.f.* Fd	7462.88	for S-S -2.02; 0/-1.01 for the cluster	7460.86/7459.85
[Zn-Fe_3S_4] WT *P.f.* Fd	7528.27	for S-S -2.02; -1.01/-2.02 for cluster	7525.24/7524.23
[Ag-Fe_3S_4] WT *P.f.* Fd	7570.75	for S-S -2.02; -1.01/-2.02 for the cluster	7567.72/7566.71
apo-D14C *P.f.* Fd	7155.08	for S-S -2.02	7153.06
[Fe_4S_4] D14C *P.f.* Fd	7506.73	for S-S -2.02; -1.01/-2.02 for the cluster	7503.70/7502.69
[Fe_3S_4] D14C *P.f.* Fd	7450.89	for S-S -2.02; 0/-1.01 for the cluster	7448.87/7447.86
dimer-[Fe_3S_4] D14C *P.f.* Fd	14901.78	for S-S (-2.02)*3; (-1.01)*2 for the clusters	14893.70
[Zn-Fe_3S_4] D14C *P.f.* Fd	7516.27	for S-S -2.02; -1.01/-2.02 for the cluster	7513.24/7512.23
[Ag-Fe_3S_4] D14C *P.f.* Fd	7558.75	for S-S -2.02; -1.01/-2.02 for the cluster	7555.72/7554.71

5 Expression, Purification and Mass Spectrometric Analysis of WT *Pyrococcus furiosus* Ferredoxin and Its D14C Mutant

5.1 Introduction

This chapter describes the aerobic cultivation of *E.coli* cells over-expressing the WT and the D14C *P.f.* ferredoxin, the subsequent protein purification, and characterization by mass spectrometric analysis. This chapter also describes oxidation of $[Fe_4S_4]$ to $[Fe_3S_4]$ in D14C *P.f*. Fd since this form is used as a starting material for the synthesis of the heterometallic cluster containing ferredoxins described in chapter 7 and 8. Procedures for aerobic protein expression and purification of ferredoxins have been developed in the Metalloprotein Chemistry and Engineering Group (80; 81; 82). This new method for expression and purification enabled crystallization of $[Fe_3S_4]$ WT *P.f*. Fd and both $[Fe_4S_4]$ and $[Fe_3S_4]$ D14C *P.f*. Fd. The X-ray crystallographic structure for $[Fe_3S_4]$ WT *P.f*. Fd was determined to 1.5 Å (4), and to 1.7 Å and 2.8 Å for $[Fe_4S_4]$ and $[Fe_3S_4]$ D14C *P.f*. Fd, respectively (82). The descriptions of the procedures are given in this report since large amounts of both ferredoxins were used in this project for the synthesis of the modified ferredoxins and their characterization. Since the procedure for the expression and purification of D14C *P.f*. Fd is very similar to the one used for WT *P.f*. Fd, these procedures are given here together. However, in order to have a better overview, the purification results of WT *P.f.* Fd and D14C *P.f.* Fd are separated into two sections.

All proteins from this project were recombinantly expressed in *E. coli* BL21(DE3) cells (Novagen) using the expression system base on pET vectors. The *E. coli* strains over-expressing WT *P.f.* Fd (HC298) and its D14C mutant (HC1067) were created by previous members of the Metalloprotein Chemistry and Engineering Group. I was involved in cell cultivation, harvesting and purification of WT *P.f.* Fd. However, most of the cell cultivation and harvesting of WT *P.f.* Fd were performed by Laboratory Technician Stefanie Boy. Cell cultivation, harvesting and purification of the D14C *P. f.* Fd were performed by student Jordi Espín Martí. The initial studies on purification of D14C *P.f*. Fd variant were carried out and described by Ph.D. student Monika Nøhr Løvgreen in her Master Thesis and to be published in her Ph.D. Thesis (81; 82).

All experiments in this chapter were performed under aerobic conditions. All chemicals used throughout this project were of analytical grade, and water used was 18.2 MΩcm QPAK Milli-Q (Millipore). The pre-packed columns and column material used for home-packed columns used for protein purification were purchased from GE Healthcare. Stirred Amicon ultrafiltration cell with a YM3 membrane (MWCO 3000) was used for concentrating the protein samples and buffer exchange throughout the experiments from this chapter. All aerobically performed protein purifications were carried out on an ÄKTA^{TM} Purifier 100 (GE Helthcare) with the exception of the initial purification step.

5.2 Experimental

5.2.1 Expression of the WT and the D14C *Pyrococcus furiosus* Ferredoxin

The following procedure is for six times 650 ml cell culture of *E. coli* HC298 strain over-expressing the WT, and *E. coli* HC1067 strain over-expressing the D14C *P.f.* Fd. In order to avoid the contamination of cells all instruments that came in contact with the cells

were sterilized. The cells were cultivated in Terrific Broth (TB) media supplied with carbenicillin as a selection marker.

Cells from a glycerol stock were streaked on an agar plate containing Luria Broth (LB) with 100 µg/mL ampicillin (LB/amp). A single colony was selected and added to 50 mL Terrific Broth with 50 µg/mL carbenicillin (TB/carb) in a 300 mL triple baffled shake flask. Two 50 mL pre-cultures were prepared per six times 650 mL large-scale cultures. The pre-cultures were incubated at 37 °C with shaking (250 rpm) until the optical density at 600 nm (OD_{600}) was 0.6-1.0. Pre-cultures were stored at 4 °C overnight. Each pre-culture was then transferred to a 50 mL sterile plastic tube, and centrifuged at 3000 rpm for 10 minutes at 4 °C. The supernatants were decanted off and discarded, and the pellets were re-suspended in 23 mL TB/carb. From this mixture, 6.5 mL was transferred into 650 mL TB/carb in 2 L triple baffled shake flask to give a total of six 650 mL large-scale cultures. The cultures were incubated at 30 °C with shaking (250 rpm) until OD_{600} was 2.4. Isopropyl-β-D-thiogalactopyranoside (IPTG) was added from a 200 mM stock solution to a final concentration of 0.1 mM, and the incubation of the cells was continued at 30 °C for 16 hours. Hereafter, the cells were harvested.

The cell cultures from each flask were transferred to Beckmann centrifuge tubes and centrifuged at 3900 rpm for 15 minutes at 4 °C. The supernatants were decanted off and discarded, while the sedimented cells were re-suspended in 25 ml ice-cold 20 mM Tris/HCl pH 8.0, and poured into 50 mL plastic tubes. The plastic tubes were centrifuged at 3900 rpm for 15 minutes at 4 °C, the supernatants were discarded and the cell pellets were stored at -80 °C until further use.

5.2.2 Purification of the WT and the D14C *Pyrococcus furiosus* Ferredoxin

Six tubes of cells from 650 ml of culture each, prepared as described in section 5.2.1, were thawed on ice. The cells in each tube were re-suspended in approximately 30 mL 20 mM Tris/HCl pH 8.0. 80 µL freshly prepared 1 M $Na_2S_2O_4$ solution was added to each tube to keep the protein in the reduced form. Hereafter, the cells were lysed by sonication (Satorius Labsonic P at 80 % amplitude) three times for 40 seconds while kept on ice during and in between sonication. Upon sonication cells were incubated for 10 minutes at 70 °C, and then centrifuged for 20 minutes at 4 °C at 13500 rpm. The clear supernatant was decanted off, and diluted four times with 20 mM Tris/HCl pH 8.00, 2 mM $Na_2S_2O_4$ solution.

The protein solution was loaded onto a 16/10 Q Sepharose Fast Flow column (CV ~ 200 mL) previously equilibrated with 20 mM Tris/HCl pH 8.0 buffer. The column was first washed with 2 CV 20 mM Tris/HCl pH 8.0 and 2 CV 20 mM Tris/HCl, 0.15 M NaCl pH 8.0. The protein of interest was eluted isocratically with 20 mM Tris/HCl, 0.4 NaCl pH 8.0. Hereafter, the volume of the protein solution was reduced by ultrafiltration. The protein solution was filtered (0.45 µm) and a maximum of 9 ml was loaded onto a HiLoad 26/60 Supredex 75 column previously equilibrated with 20 mM Tris/HCl, 0.15 M NaCl pH 8.0, and eluted using the same buffer. Fractions containing ferredoxin were collected, and the buffer was exchanged into 20 mM Tris/HCl pH 8.0 by ultrafiltration. A maximum of 15 mg of protein was loaded onto a 16/10 Source 30Q column equilibrated with 20 mM Tris/HCl pH 8.0. The protein was eluted using a linear salt gradient from 0.15 to 0.3 M NaCl in 20 mM Tris/HCl pH 8.0 over 10 CV in a case of WT P.f. Fd, while in a case of

D14C P.f. Fd elution of the protein was achieved using a linear salt gradient from 0.15 to 0.4 M NaCl in 20 mM Tris/HCl pH 8.0 over 17 CV. Fractions containing ferredoxin were collected and the buffer was exchanged into 20 mM Tris/HCl pH 8.0 by ultrafiltration, and the volume of the protein solution was reduced to a final concentration of 5 mg/mL. The protein concentration was determined by UV-vis spectrophotometry using the following molar extinction coefficients: ε_{390} = 17 $mM^{-1}cm^{-1}$ for $[Fe_4S_4]$ WT *P.f.* Fd, ε_{408} = 18 $mM^{-1}cm^{-1}$ for $[Fe_3S_4]$ WT *P.f.* Fd (30), and ε_{390} = 20.2 $mM^{-1}cm^{-1}$ for $[Fe_4S_4]$ D14C *P.f.* Fd (41).The purified protein sample was analyzed by mass spectrometry as described in section 4.3.1. Protein was frozen and stored at -20 °C in portions of 1 mL until further use.

5.2.3 Oxidation to and Purification of $[Fe_3S_4]$ D14C *Pyrococcus furiosus* Ferredoxin

Oxidation was performed on the protein purified as described in section 5.2.2. The protein sample was thawed, and the protein solution was exchanged into 20 mM BisTris/HCl pH 5.8 buffer by ultrafiltration. 15 times molar excess of potassium ferricyanide (3.29 mg dissolved in 1 mL of Milli-Q water) and 1.5 times molar excess of EDTA (0.37 mg dissolved in 1 mL of Milli-Q water) was added to the solution containing 5 mg of $[Fe_4S_4]$ D14C *P.f.* Fd. The final volume of the protein solution was adjusted to 5 mL using 20 mM BisTris/HCl pH 5.8 buffer. Protein solution was left over night at room temperature with gentle stirring. The excess reagent was removed by ultrafiltration using 20 mM BisTris/HCl pH 5.8 buffer to remove the ferricyanide. Subsequently, the protein solution was filtered (0.45 µm) and loaded onto a 16/10 Source 30Q column equilibrated with 20 mM BisTris/HCl pH 5.8. The protein was eluted using a linear salt gradient from 0.15 to 0.4 M NaCl in 20 mM BisTris/HCl pH 5.8 over 17 CV. Fractions containing ferredoxin were collected and the buffer was exchanged into 20 mM BisTris/HCl pH 5.8 by ultrafiltration, and the volume of the protein solution was reduced to a final concentration of 5 mg/mL. The purified protein sample was analyzed using mass spectrometry (see section 4.3.1). The protein concentration was determined by UV-Vis spectrophotometry using the molar extinction coefficients ε_{408} = 18 $mM^{-1}cm^{-1}$ for $[Fe_3S_4]$ D14C *P.f.* Fd (30). The protein was frozen and stored at - 20 °C in portions of 1 mL until further use.

5.2.4 Dimerization of Oxidized D14C *Pyrococcus furiosus* Ferredoxin

Dimerization experiment was performed using the protein sample prepared as described in section 5.2.3. The protein solution was exchanged into 20 mM Tris/HCl pH 8.0 by ultrafiltration, filtered (0.45 µm) and hereafter loaded onto a 16/10 Source 30Q column equilibrated with 20 mM Tris/HCl pH 8.0. The protein of interest was eluted using a linear salt gradient from 0.15 to 0.4 M NaCl in 20 mM Tris/HCl pH 8.0 over 17 CV. Fractions corresponding to the observed two peaks were collected, protein samples were concentrated and buffer exchanged to 20 mM Tris/HCl pH 8.0 by ultrafiltration. The purified protein samples were analyzed using mass spectrometry (see section 4.3.1). Afterwards, the samples were mixed and left over night at 4 °C. The same purification procedure was performed the day after.

5.3 Results and Discussion

Since the initial anion exchange step in the purification procedures for both WT *P.f.* Fd and D14C *P.f.* Fd were not performed on HPLC, the brown colored protein was collected based on visually estimated elution. Protein purifications performed on HPLC system in

aerobic conditions were monitored at three wavelengths – 280 nm, 390 nm, and 408 nm. Both WT *P.f.* Fd and D14C P.f. Fd were purified using the procedure given in section 5.2.2.

5.3.1 Purification and Mass Spectrometric Analysis of WT *Pyrococcus furiosus* Ferredoxin

Chromatograms for the purification of WT *P.f.* Fd on a 26/60 Superdex 75 and a 16/10 Source 30Q are shown in Figure 5.1 and Figure 5.2, respectively. The collected fractions are marked with black boxes.

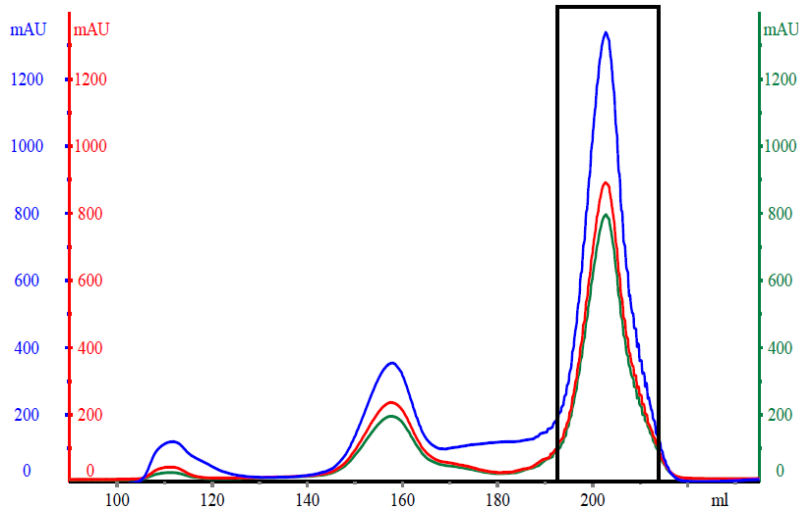

Figure 5.1: Chromatogram for the purification of WT *P.f.* Fd on a 26/60 Superdex 75 column. X-axis: elution volume; blue line: absorption at 280 nm; red line: absorption at 390 nm; green line: absorption at 408 nm.

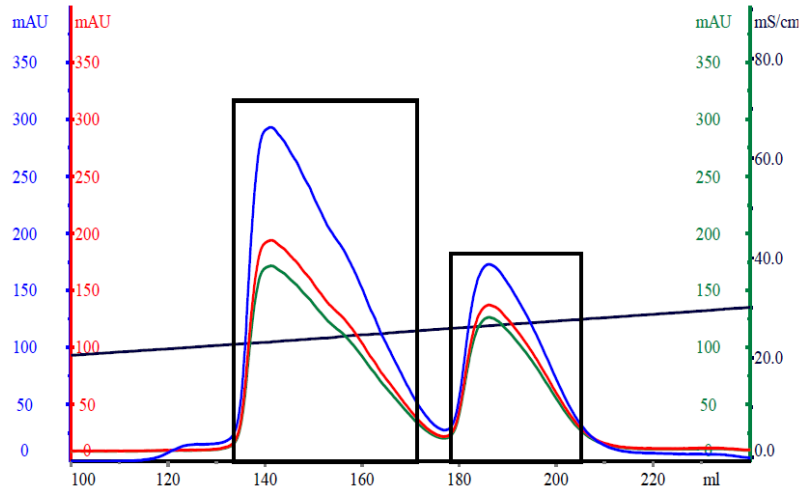

Figure 5.2: Chromatogram for the purification of WT *P.f.* Fd on a 16/10 Source 30Q column. X-axis: elution volume; blue line: absorption at 280 nm; red line: absorption at 390 nm; green line: absorption at 408 nm; black line: conductivity.

From the purification on a 16/10 Source 30Q column two peaks were observed, as expected due to the cluster interconversion (see section 3.3.1), with absorption at all three wavelengths (see Figure 5.2). The first peak elutes at ~ 23.9 mS/cm, and the second at ~ 26.5 mS/cm.

Upon volume reduction and buffer exchange by ultrafiltration, protein samples from both peaks were analyzed by UV-vis spectrophotometry (see Figure 5.3). The protein from the first peak shows an absorption maximum at 390 nm characteristic for Fd containing an [Fe_4S_4] cluster, while an absorption maximum at 408 nm is observed for the second peak characteristic for Fd containing an [Fe_3S_4] cluster (see section 3.4.1) (30). The yield of the purified WT *P.f.* Fd in average was ~ 8 mg/L cell culture.

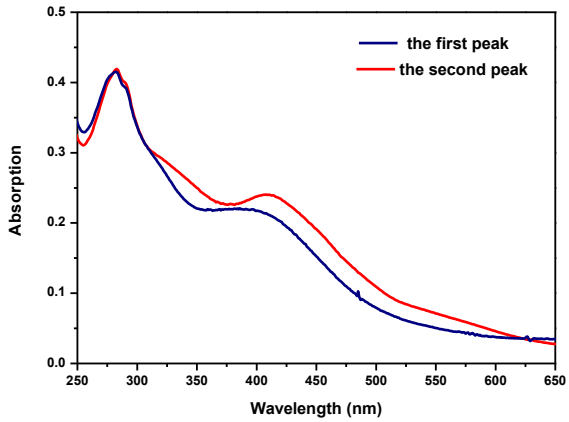

Figure 5.3: UV-vis spectra of the protein from the first (blue line) and the second (red line) chromatographic peak in Figure 5.2. UV-vis spectra are normalized according to the absorbance at 280 nm.

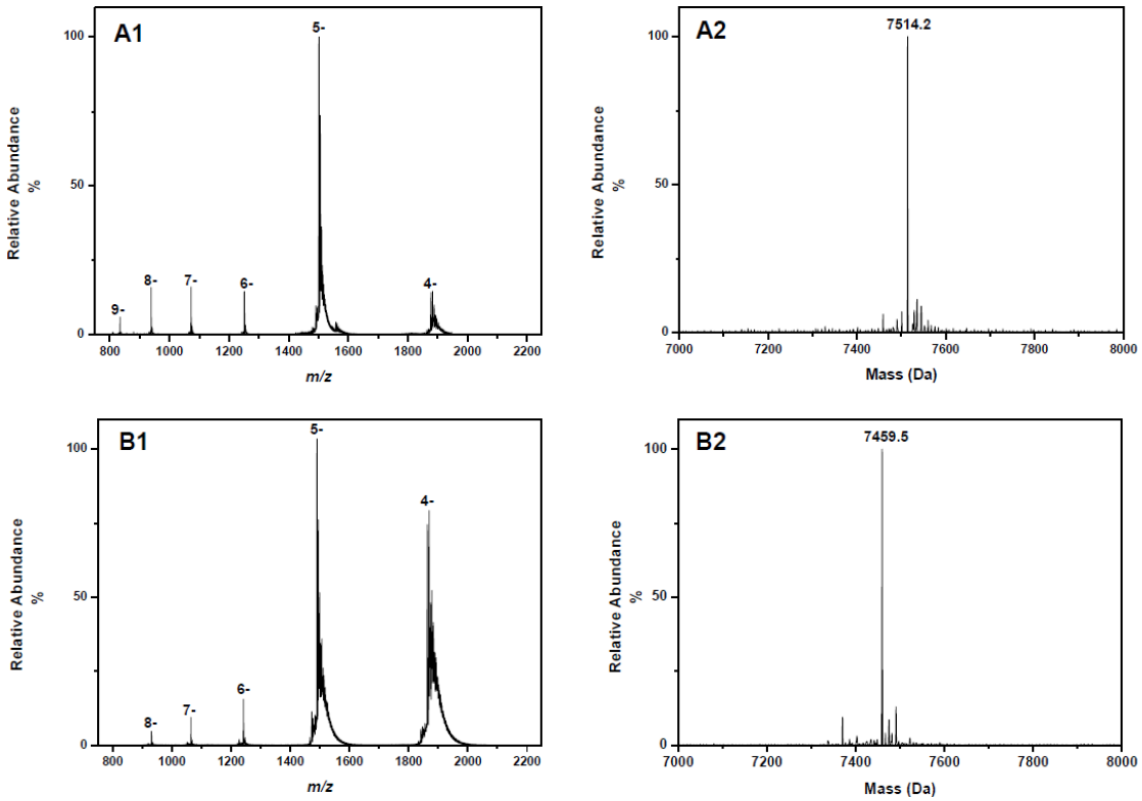

Figure 5.4: Mass spectrometric analysis spectra of purified WT *P.f.* Fd. (A1) *m/z*- and (A2) mass spectrum of the protein from the first peak, and (B1) *m/z*- and (B2) mass spectrum of the protein from the second chromatographic peak in Figure 5.2.

The protein samples from the purification were analyzed by mass spectrometry as described in section 4.3.1. The Figure 5.4 shows negative ion-mode mass spectra for

purified *P.f.* Fd. A1 is the *m/z*-spectrum of the protein from the first chromatographic peak in Figure 5.2. It shows a distribution of six protein charge states – from 9- to 4-, with charge state 5- being the dominating. The *m/z*-range from 800 to 1300 was used for calculating the mass spectrum (as described in section 4.3.2). The apparent mass from mass spectrum A2 is 7514.2 Da. The apparent mass matches the expected mass for WT *P.f.* Fd containing an $[Fe_4S_4]$ cluster in 2+ oxidation state and with one disulfide bond (Cys21-Cys48) (see Table 4.1). The *m/z*-spectrum for the protein from the second chromatographic peak is shown in spectrum B1. The *m/z*-range from 800 to 1300 was used for calculating the mass spectrum (see section 4.3.2). The apparent mass from the spectrum B2 is 7459.5 Da matching the expected mass for WT *P.f.* Fd containing an $[Fe_3S_4]$ cluster in 1+ oxidation state and with one disulfide bond (Cys21-Cys48) (see Table 4.1). Hereby, the mass spectrometric data have confirmed that aerobic purification of WT *P.f.* Fd produces intact both $[Fe_4S_4]$ and $[Fe_3S_4]$ ferredoxins in their oxidized forms and both containing an intact disulfide bond.

5.3.2 Purification and Mass Spectrometric Analysis of $[Fe_4S_4]$ D14C *Pyrococcus furiosus* Ferredoxin

Chromatograms for the purification of D14C *P.f.* Fd on a 26/60 Superdex 75 column and a 16/10 Source 30Q are shown in Figure 5.5 and 5.6, respectively. The chromatogram for the purification on of D14C *P.f.* Fd a 26/60 Superdex 75 column is very similar to the chromatogram for WT *P.f.* Fd purification (Figure 5.1).

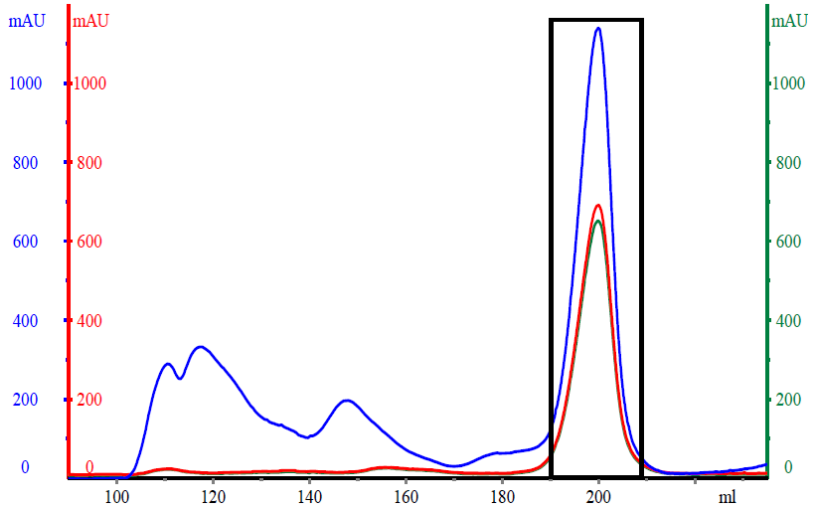

Figure 5.5: Chromatogram for the purification of D14C *P.f.* Fd on a 26/60 Superdex 75 column. X-axis: elution volume; blue line: absorption at 280 nm; red line: absorption at 390 nm; green line: absorption at 408 nm.

Ferredoxin elutes as a major peak with absorption at all three wavelengths. From the purification on a 16/10 Source 30Q the major peak is observed with absorption at all three wavelengths and it elutes at ~ 25.8 mS/cm. The peak was analyzed by UV-vis spectophotometry after volume reduction and buffer exchange by ultrafiltration. The UV-vis spectrum (see Figure 5.7) shows an absorption maximum at 390 nm which is characteristic for Fd containing an $[Fe_4S_4]$ cluster (30). The yield of the purified $[Fe_4S_4]$ D14C *P.f.* Fd was ~ 12 mg/L cell culture.

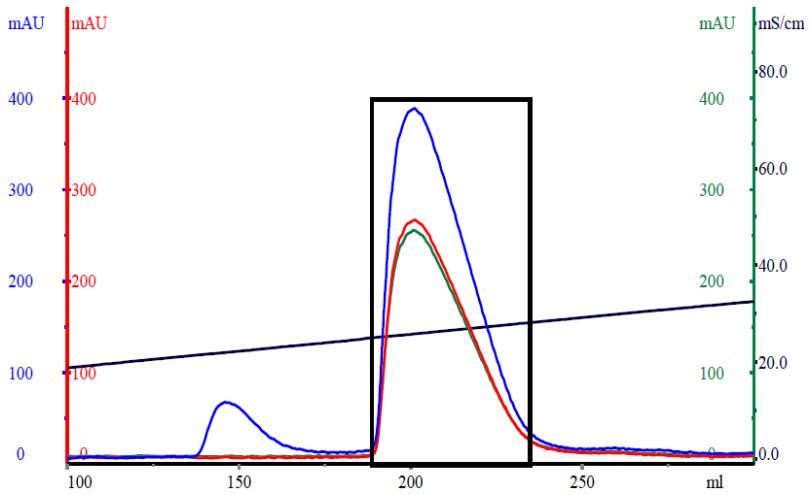

Figure 5.6: Chromatogram for the purification of D14C *P.f.* Fd on a 16/10 Source 30Q column. X-axis: elution volume; blue line: absorption at 280 nm; red line: absorption at 390 nm; green line: absorption at 408 nm; black line: conductivity.

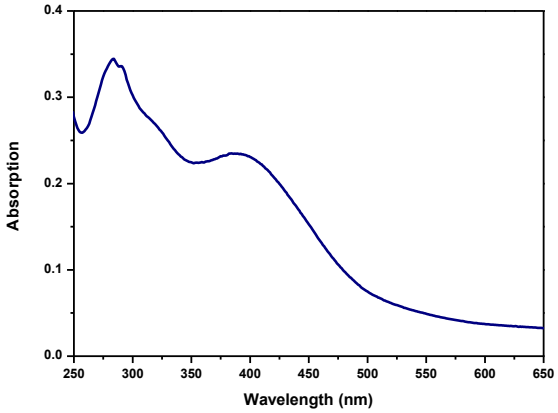

Figure 5.7: UV-vis spectrum of the protein from the chromatographic peak in Figure 5.6.

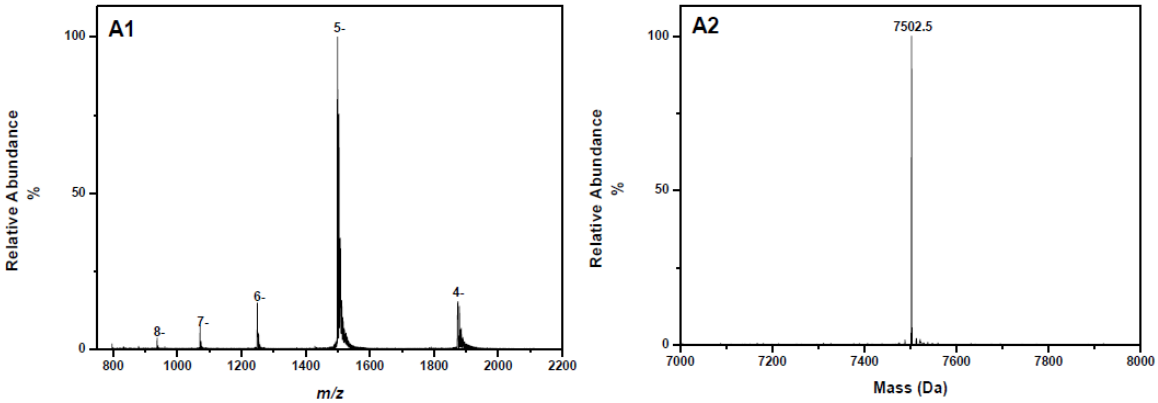

Figure 5.8: Mass spectrometric analysis spectra of purified D14C *P. f.* Fd. (A1) *m/z*- and (A2) mass spectrum of the protein from the chromatographic peak in Figure 5.6.

The purified D14C *P.f.* Fd was analyzed by mass spectrometry (see section 4.3.1), and negative ion-mode spectra are shown in Figure 5.8. The spectra A1 and A2 present the *m/z* and the mass spectrum of the protein from the chromatographic peak in Figure 5.6, respectively. The *m/z*-spectrum A1 shows the same distribution of the protein charge state, as seen in the case of WT *P.f.* Fd (see Figure 5.4, spectra A1 and B1). The *m/z*-range from 800 to 1300 was used for calculating the mass spectrum (see section 4.3.2).

The apparent mass of 7502.5 Da matches the expected mass for D14C *P.f.* Fd containing [Fe_4S_4] cluster in 2+ oxidation state and with one disulfide bond (Cys21-Cys48) (see Table 4.1), and hereby it confirms that aerobic purification of D14C *P.f.* Fd in 20 mM Tris/HCl pH 8.0 produces only the [Fe_4S_4] form of the protein as opposed to WT *P.f.* Fd where aerobic purification results in both the [Fe_4S_4] and the [Fe_3S_4] forms of the protein being isolated (see section 5.3.1).

Furthermore, the [Fe_4S_4] cluster from D14C *P.f.* Fd appears to be much more stable compared to the [Fe_4S_4] from WT *P.f.* Fd. If stored for several months at -20 °C and afterwards re-purified (using the final anion exchange step described in section 5.2.2) the sample of [Fe_4S_4] WT *P.f.* Fd resulted in more than 50 % of it being converted to the [Fe_3S_4] form. The same kind of behavior was not observed for the [Fe_4S_4] cluster from the D14C variant – no conversion to the [Fe_3S_4] form was detected, and the [Fe_4S_4] claster remained intact (chromatograms not shown). However, this kind of behavior for the [Fe_4S_4] cluster from the D14C mutant is not surprising since it has been reported before that mutating the coordinating aspartate to cysteine impair the ease with which [Fe_4S_4] converts to [Fe_3S_4] (see section 3.3.1) (37).

5.3.3 Oxidation to, Purification and Mass Spectrometric Analysis of [Fe_3S_4] D14C *Pyrococcus furiosus* Ferredoxin

Conversion of [Fe_4S_4] to [Fe_3S_4] D14C *P.f.* Fd is necessary since this form of the protein is used as the starting material for the synthesis of artificial ferredoxins described in chapter 7 and 8. Oxidation of [Fe_4S_4] to [Fe_3S_4] D14C *P.f*. Fd results in a free Cys14, which corresponds to Asp14 in [Fe_3S_4] WT *P.f*. Fd (4; 82). As previously observed, the oxidation of [Fe_4S_4] D14C *P.f.* Fd at pH 7.8 (similar to the procedure reported by Duderstadt *et al*. (43)) followed by anion exchange at the same pH produces multiple peaks (81). Therefore, pH of the oxidation reaction was changed to pH 5.8 (82). At pH 5.8 free Cys14 is expected to be fully protonated and the protein elution is a single peak was expected (82).

The chromatogram from the purification at pH 5.8 on a 16/10 Source 30Q column, using the procedure described in section 5.2.3, is shown in Figure 5.9. A single peak is observed from the chromatogram eluting at ~ 23.8 mS/cm compared to the usual [Fe_4S_4] D14C *P.f.* Fd elution at ~ 25.8 mS/cm.

Upon volume reduction and buffer exchange by ultrafiltration the peak was analyzed by UV-vis spectophotometry. Figure 5.10 shows the UV-vis spectra of [Fe_4S_4] D14C *P.f.* Fd before and after oxidation. The UV-vis spectrum for the sample after oxidation shows a shift in absorption maximum from 390 nm towards higher wavelengths compared to the [Fe_4S_4] D14C *P.f.* Fd before oxidation. The purified protein was analyzed by mass spectrometry in order to confirm that the conversion from [Fe_4S_4] to [Fe_3S_4] D14C *P.f.* Fd has been successful. The Figure 5.11 shows the negative ion-mode mass spectra of the purified protein.

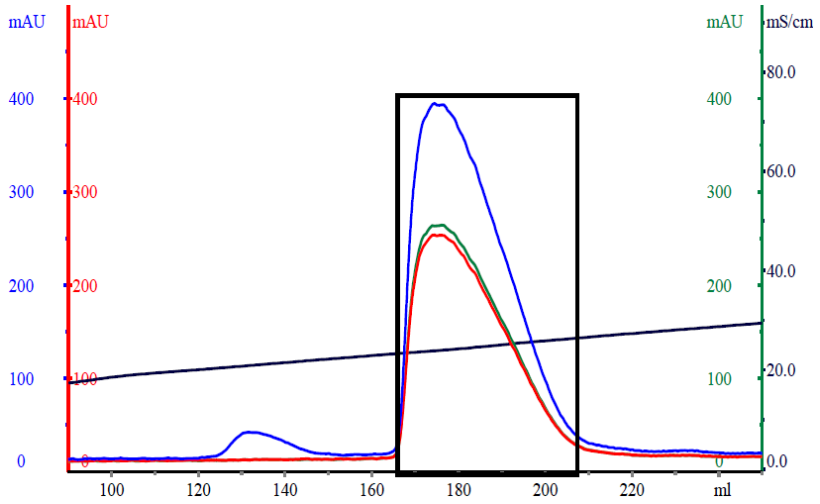

Figure 5.9: Chromatogram for the purification of [Fe_3S_4] D14C *P.f.* Fd on a 16/10 Source 30Q column. X-axis: elution volume; blue line: absorption at 280 nm; red line: absorption at 390 nm; green line: absorption at 408 nm; black line: conductivity.

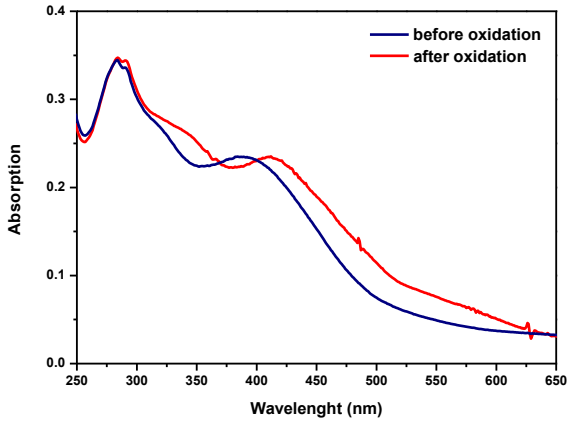

Figure 5.10: UV-vis spectra of [Fe_4S_4] D14C *P.f.* Fd before (blue line) and after (red line) oxidation described in section 5.2.3. UV-vis spectra are normalized according to the absorbance at 280 nm.

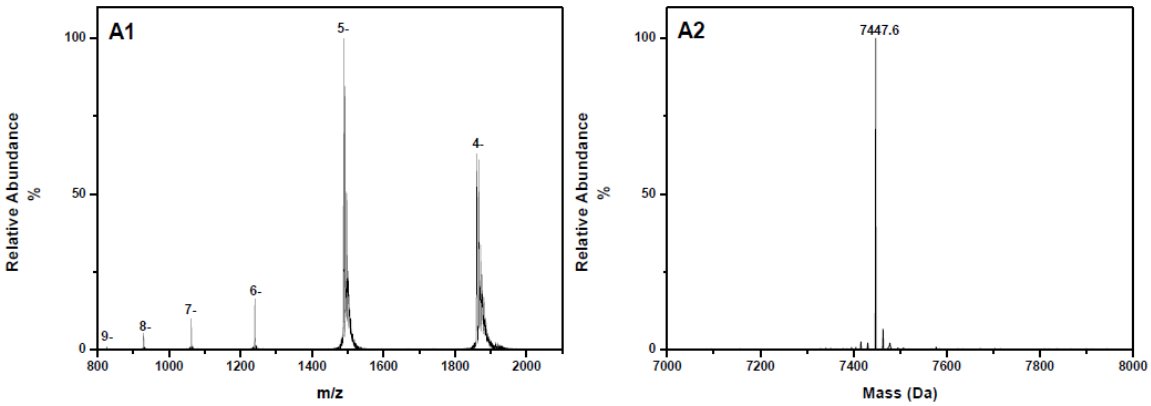

Figure 5.11: Mass spectrometric analysis spectra of the protein from the chromatographic peak in Figure 5.9. (A1) *m/z*- and (A2) mass spectrum.

From the *m/z*-spectrum A1 the range from 800 to 1300 was used for calculating the mass spectrum (see section 4.3.2). The apparent mass 7447.6 Da (spectrum A2) matches the expected mass for D14C *P.f.* Fd containing [Fe_3S_4] cluster in 1+ oxidation

state and with one disulfide bond (Cys21-Cys48) present (see Table 4.1) which confirms the successful conversion of the [Fe_4S_4] form to the [Fe_3S_4] form of D14C *P.f.* Fd.

5.3.4 Dimerization of Oxidized D14C *Pyrococcus furiosus* Ferredoxin and Its Mass Spectrometric Analysis

As observed from section 5.3.3, oxidation of [Fe_4S_4] to [Fe_3S_4] D14C *P.f.* Fd at pH 5.8 and subsequent anion exchange at the same pH (according to the procedure given in section 5.2.3) produces a single peak (see Figure 5.9) containing a single species – [Fe_3S_4] D14C *P.f.* Fd. However, it was observed that oxidation of [Fe_4S_4] D14C *P.f.* Fd at pH 8.0 followed by anion exchange at the same pH produces multiple peaks (81). Since at pH 8.0 a free Cys14 in [Fe_3S_4] D14C *P.f.* Fd is expected to be partly deprotonated, it was suspected that at this pH a formation of a disulfide bonded dimer ferredoxin occurs (82). Therefore, re-purification of [Fe_3S_4] D14C *P.f.* Fd (see section 5.3.3) was performed at pH 8.0 as described in section 5.2.4. The chromatogram from the re-purification at pH 8.0 on a 16/10 Source 30Q column is shown in Figure 5.12.

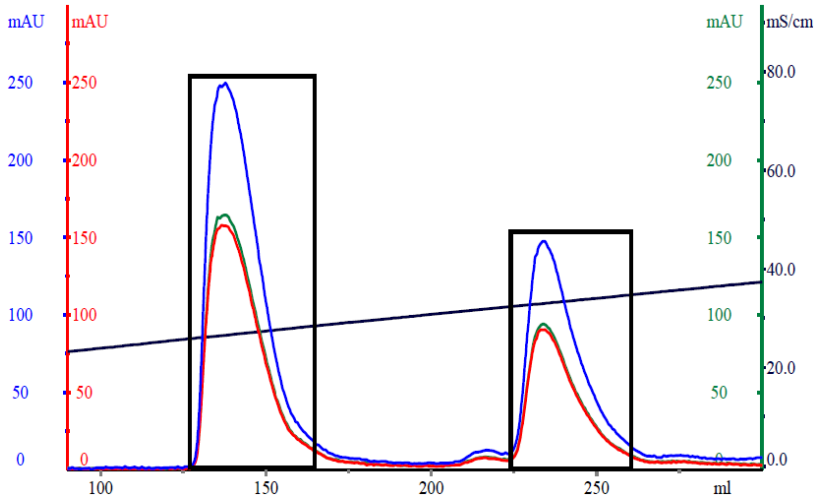

Figure 5.12: Chromatogram for the re-purification of [Fe_3S_4] D14C *P.f.* Fd at pH 8.0 on a 16/10 Source 30Q column. X-axis: elution volume; blue line: absorption at 280 nm; red line: absorption at 390 nm; green line: absorption at 408 nm; black line: conductivity.

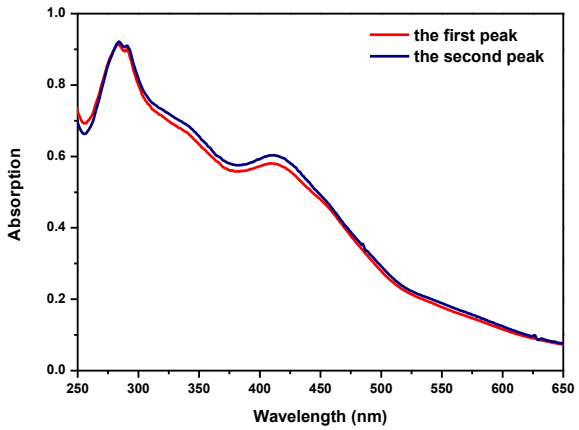

Figure 5.13: UV-vis spectra of the protein samples from the first (red line) and from the second (blue line) chromatographic peak in Figure 5.12. UV-vis spectra are normalized according to the absorbance at 280 nm.

Elution in two peaks with absorption at all three wavelengths is observed from the chromatogram. The first peak elutes at ~ 26.5 mS/cm, and the second at ~ 32.7 mS/cm. Upon volume reduction and buffer exchange the peaks were analyzed by UV-vis spectophotometry, see Figure 5.13.

No visible changes in the UV-vis spectrum for the protein samples from the first and the second chromatographic peak can be observed – they both show the absorption maxima at 408 nm typical for $[Fe_3S_4]$ clusters. Figure 5.14 shows the mass spectra in negative ion-mode for both protein samples. The spectra A1 and A2 here present the *m/z*- and the mass spectrum of the protein from the first chromatographic peak (see Figure 5.12), respectively. Hereby, the presence of $[Fe_3S_4]^+$ D14C *P.f.* Fd with apparent mass 7447.6 Da is confirmed (see Table 4.1). The protein from the second chromatographic peak (see Figure 5.12) was identified to be a disulfide bonded dimer $[Fe_3S_4(Cys\text{-}S)\text{-}(S'\text{-}Cys')Fe'_3S_4]^{2+}$ D14C *P.f.* Fd. (see Figure 5.14, spectra B1 and B2). The *m/z*-range from 1200 to 2000 was used for calculating the mass spectrum. The apparent mass of disulfide bonded dimer is 14893.1 Da (see Figure 5.14, spectrum B2) which matches the expected mass for a dimer of D14C *P.f.* Fd (see Table 4.1) containing two metal clusters $[Fe_3S_4]$ in 1+ oxidation state each, and three disulfide bonds – two Cys21-Cys48 disulfide bonds and intermolecular Cys14-Cys14' disulfide bond.

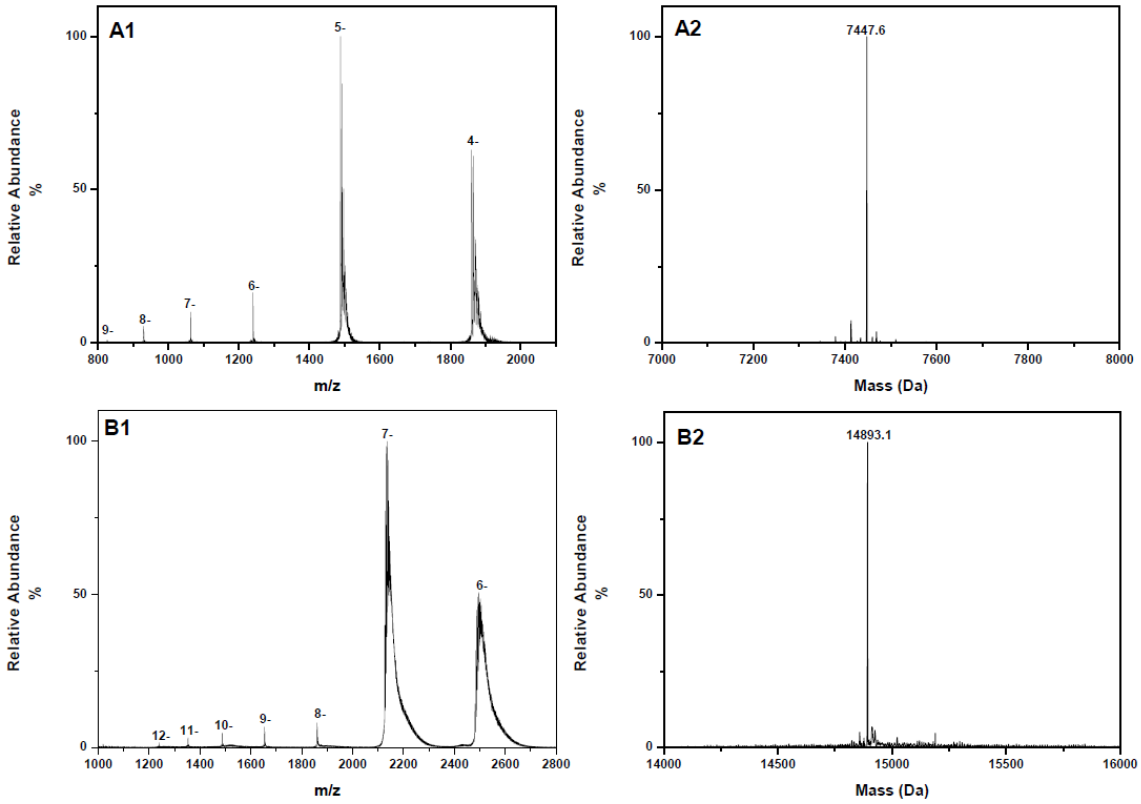

Figure 5.14: Mass spectrometric analysis spectra of the protein samples from the chromatographic peaks in Figure 5.12. (A1) *m/z*- and (A2) mass spectrum of the protein from the first, and (B1) *m/z*- and (B2) mass spectrum of the protein from the second chromatographic peak.

Based on the mass spectrometric data when $[Fe_4S_4]$ D14C *P.f.* Fd is oxidized and subsequently chromatographically purified at pH 5.8 formation of only one species is observed – $[Fe_3S_4]$ D14C *P.f.* Fd. Re-purification of $[Fe_3S_4]$ D14C *P.f.* Fd at pH 8.0

results in a formation of two species – the monomer and the dimer consisting of two D14C *P.f.* Fds containing the [Fe_3S_4] cluster with an additional intermolecular disulfide bond. Thus, as previously assumed in ref (82), [Fe_3S_4] D14C *P.f.* Fd shows a pH dependent equilibrium between a monomer containing protonated and deprotonated Cys14 residue, and a formation of disulfide bonded dimer (an illustration given in Figure 5.15). The pK_a value of Cys14 was estimated to 8.8 using PROPKA (83; 84). The disulfide bonded dimer is formed when two monomers with deprotonated Cys14 residue form intermolecular disulfide bond. The reaction occurs under aerobic conditions, in the presence of oxygen as an oxidant.

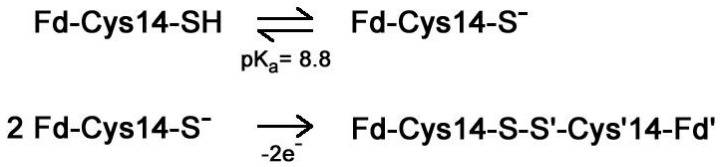

Figure 5.15: pH dependent equilibrium of D14C [Fe_3S_4] *P.f.* Fd between protonated and deprotonated monomers, and formation of a disulfide bonded dimer from deprotonated monomers (82)**.**

Over night incubation of the protein solution containing the mixture of the monomer and disulfide bonded dimer of [Fe_3S_4] D14C *P.f.* Fd at pH 8.0, under aerobic conditions has caused the difference in the ratio of amounts of the two species present. Fractions corresponding to the two peaks from the chromatogram in Figure 5.12 were mixed, and re-purified after overnight incubation at pH 8.0, at 4 °C, as described in section 5.2.4. Two overlaid chromatograms for the protein purification at pH 8.0 on a 16/10 Source 30Q before and after overnight incubation are shown in Figure 5.16.

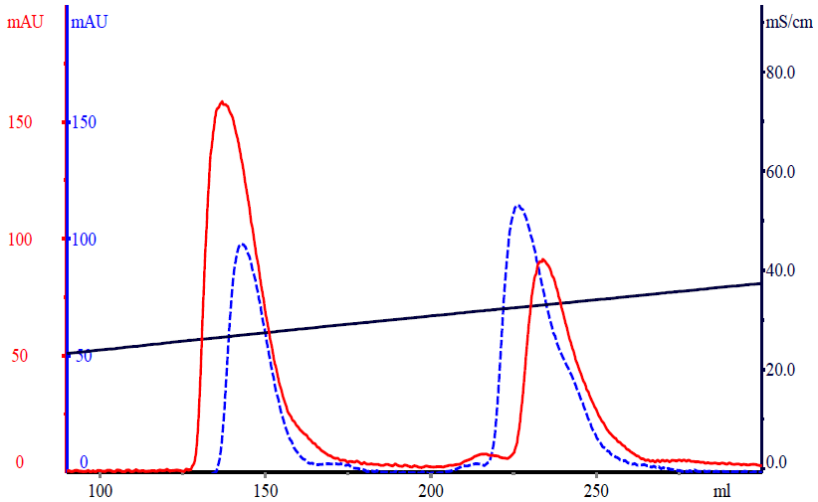

Figure 5.16: Chromatograms for the re-purification of [Fe_3S_4] D14C *P.f.* Fd at pH 8.0 on a 16/10 Source 30Q column at pH 8.00. X-axis: elution volume; Y-axis: absorption at 280 nm for the protein purified before (red line) and after (blue line) overnight incubation.

The chromatogram still shows two peaks but the ratio between them has changed. As, expected, the amount of a disulfide bonded dimer has increased due to prolongued oxygen exposure indicating the effect of oxygen on the dimer formation. When carried out under anaerobic conditions the oxidation of [Fe_4S_4] to [Fe_3S_4] D14C *P.f.* Fd was performed successfully at pH 7.8 with 15-fold excess of ferricynide but the formation of a disulfide bonded dimer was not reported (43). However, the dimer formation would be

expected under these conditions because ferricyanide, with its formal potential of +410 mV (85), should be efficient enough oxidizing agent to cause its formation.

5.4 Conclusions

E. coli cells recombinantly expressing WT *P.f.* Fd were successfully aerobically cultivated. Aerobic purification of WT *P.f.* Fd consisting of an initial anion exchange, size exclusion and final anion exchange chromatographical step produces two forms of ferredoxin – $[Fe_4S_4]$ and $[Fe_3S_4]$ ferredoxin. UV-vis spectrophotometry and mass spectrometric analysis were used to confirm the presence of purified $[Fe_4S_4]^{2+}$ and $[Fe_3S_4]^{+}$ *P.f.* Fd.

D14C *P.f.* Fd was successfully recombinantly expressed in *E. coli* cells. The cells were aerobically cultivated, and hereafter the protein was aerobically purified. Purification procedure consisting of an initial anion exchange, size exclusion and final anion exchange chromatographical step produces the ferredoxin containing an $[Fe_4S_4]^{2+}$ cluster characterized by UV-vis spectrophotometry and mass spectrometric analysis. Replacement of aspartate ligation by cysteine in the D14C variant has lead to a more inert $[Fe_4S_4]$ cluster as compared to the one from the WT *P.f.* Fd. Oxidation of $[Fe_4S_4]$ to $[Fe_3S_4]$ D14C *P.f.* Fd was successfully carried out at pH 5.8 by overnight incubation under aerobic conditions of the $[Fe_4S_4]$ Fd form using 15 times molar excess of potassium ferricyanide. The product of oxidation i.e. $[Fe_3S_4]$ D14C *P.f.* Fd has a free Cys14 residue, and it shows a pH dependent equilibrium between protonated and deprotonated monomer and a formation of disulfide bonded dimer in the presence of oxidant. At pH 5.8 only the protonated monomer is present. At pH 8.0 mass spectrometric analysis has confirmed the presence of two species – the monomer and the dimer consisting of two $[Fe_3S_4]$ D14C *P.f.* Fds with an additional intermolecular disulfide bond.

6 Anaerobic Re-purification and Electrochemical Characterization of WT *Pyrococcus furiosus* Ferredoxin and Its D14C Mutant

6.1 Introduction

This chapter describes the anaerobic re-purification of aerobically purified WT *P.f.* Fd and its D14C mutant (see chapter 5), and electrochemical characterization of these proteins using a bulk solution cyclic voltammetry. Electrochemical characterization of both $[Fe_4S_4]$ and $[Fe_3S_4]$ cluster containing WT *P.f.* Fd and its D14C mutant are used in this project as a reference for the electrochemical characterization of the heterometallic ferredoxins described in chapter 7 and 8. The conditions used in this study are based on a previous study of electrochemical properties of WT *P.f.* Fd described by Jytte Kristensen in her Ph.D. Thesis (86).

Redox properties of both $[Fe_4S_4]$ and $[Fe_3S_4]$ WT *P.f.* Fd have been previously studied using bulk redox titrations monitored by EPR spectroscopy (3; 87) and also using electrochemical techniques such as a differential pulse voltammetry, and bulk and film cyclic voltammetry (40; 41; 86; 88; 89; 90; 91).

The redox potential of $[Fe_4S_4]$ D14C *P.f.* Fd was determined by differential pulse voltammetry (41), while the redox properties of $[Fe_3S_4]$ D14C *P.f.* Fd have not been reported before.

6.2 Anaerobic Re-purification of WT *Pyrococcus furiosus* Ferredoxin and Its D14C Mutant

All experiments in this chapter were performed under anaerobic conditions. For this purpose an Anaerobic Flexible Vinyl Coy Chamber (Coy Laboratories) with a nitrogen/hydrogen atmosphere (2-4 % hydrogen) was used. The chamber was equipped with an ÄKTA^{TM} Prime (GE Helthcare) HPLC system enabling monitoring of protein purifications at 280 nm, a spectrophotometer (NanoDrop ND-1000, NanoDrop Technologies), a magnetic stirrer, and a Vivacell 70 (Sartorius Stedum Biotech) with a 5000 MWCO membrane used for concentration or changing buffers of purified protein samples. Also, the anaerobic chamber was equipped with cables suitable for connecting the electrodes in the electrochemistry setup with a potentiostat (see section 6.3.1.1). In all experiments, the oxygen concentration was below the detection limit of the gas analyzer.

Aerobically purified samples of a mixture containing $[Fe_4S_4]$ and $[Fe_3S_4]$ WT *P.f.* Fd, and of $[Fe_3S_4]$ D14C *P.f.* Fd were re-purified inside the glove box prior the electrochemical experiments in order to ensure pure samples and remove potential traces of oxygen. Aerobically purified $[Fe_4S_4]$ D14C *P.f.* Fd, due to its stability (see section 5.3.2), was not re-purified. It was transferred inside the glove box and buffer exchanged several times prior the electrochemical experiment in order to remove traces of oxygen. The procedure used for re-purification of both ferredoxins is based on the final anion-exchange step in aerobic purification of these ferredoxins (see section 5.2.2). Since the purification procedures are very similar, they are given together in the experimental section, while the results are separated in to two sections to have a better overview.

6.2.2 Experimental

Frozen aerobically purified protein sample was transferred into the glove box, thawed and loaded onto a 16/10 Source 30Q column equilibrated with 20 mM Tris/HCl pH 8.0 for the re-purification of a mixture of $[Fe_3S_4]$ and $[Fe_4S_4]$ WT *P.f.* Fd. For the re-purification of $[Fe_3S_4]$ D14C *P.f.* Fd the column was equilibrated with 20 mM BisTris/HCl pH 5.8. The protein of interest was eluted using a linear salt gradient from 0.15 to 0.3 M NaCl in 20 mM Tris/HCl pH 8.0 or in 20 mM BisTris/HCl pH 5.8 over 10 CV for WT *P.f.* Fd and D14C *P.f.* Fd, respectively. Fractions containing ferredoxin were collected and the buffer was exchanged into 20 mM Tris/HCl pH 8.0 using a Vivacell 70 with a 5000 MWCO membrane. The protein concentration was determined by UV-vis spectrophotometry using the following molar extinction coefficients: ε_{390} = 17 $mM^{-1}cm^{-1}$ for $[Fe_4S_4]$ WT *P.f.* Fd, ε_{408} = 18 $mM^{-1}cm^{-1}$ for $[Fe_3S_4]$ WT *P.f.* Fd (30), ε_{390} = 20.2 $mM^{-1}cm^{-1}$ for $[Fe_4S_4]$ D14C *P.f.* Fd and ε_{408} = 18 $mM^{-1}cm^{-1}$ for $[Fe_3S_4]$ D14C *P.f.* Fd (41).

6.2.3 Results

6.2.3.1 Re-purification of $[Fe_4S_4]$ and $[Fe_3S_4]$ WT *P.f.* Fd

A chromatogram for the re-purification of a mixture of $[Fe_4S_4]$ and $[Fe_3S_4]$ WT *P.f.* Fd on a 16/10 Source 30Q is shown in Figure 6.1. The collected fractions are marked with black boxes.

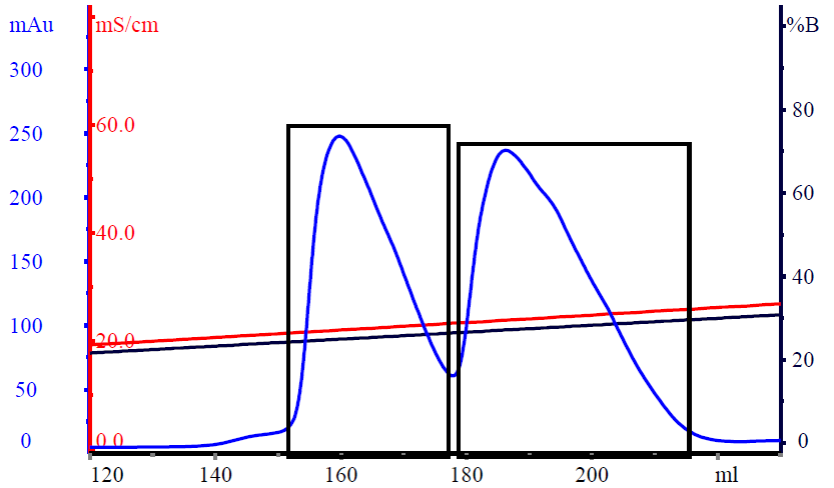

Figure 6.1: Chromatogram for the re-purification of a mixture of $[Fe_4S_4]$ and $[Fe_3S_4]$ WT *P.f.* Fd on a 16/10 Source 30Q column. X-axis: elution volume; blue line: absorption at 280 nm; red line: conductivity; black line: NaCl concentration given as percent of 1 M NaCl.

The chromatogram is in agreement with the one obtained from aerobic purification (see section 5.3.1). Two peaks are observed – the first peak eluting at ~ 22.1 mS/cm and the second at ~ 23.9 mS/cm. After volume reduction and buffer exchange into 20 mM Tris/HCl pH 8.00 both protein fraction were analyzed by UV-vis spectrophotometry and mass spectrometry (data not shown). As it was expected, the protein from the first chromatographic peak is identified to contain $[Fe_4S_4]$ cluster, and $[Fe_3S_4]$ cluster from the second peak. Both of them are purified in the oxidized form. The obtained data were in agreement with aerobically purified WT *P.f.* Fds (see section 5.3.1).

6.2.3.2 Re-purification of $[Fe_3S_4]$ D14C *P.f.* Fd

A chromatogram from the re-purification of $[Fe_3S_4]$ D14C *P.f.* Fd on a 16/10 Source 30Q is shown in Figure 6.2. The collected fractions are marked with a black box. The chromatogram obtained is in agreement with the one from aerobic purification of $[Fe_3S_4]$

D14C *P.f.* Fd. One major peak is observed eluting at ~ 20.3 mS/cm. After volume reduction of collected fractions and subsequent buffer exchange into 20 mM Tris/HCl pH 8.0, the protein was analyzed using UV-vis spectrophotometry and mass spectrometry (data not shown). Hereby, the presence of [Fe_3S_4] D14C *P.f.* Fd in an oxidized form was confirmed. These data were in agreement with those from aerobically purified [Fe_3S_4] D14C *P.f.* Fd (see section 5.3.3).

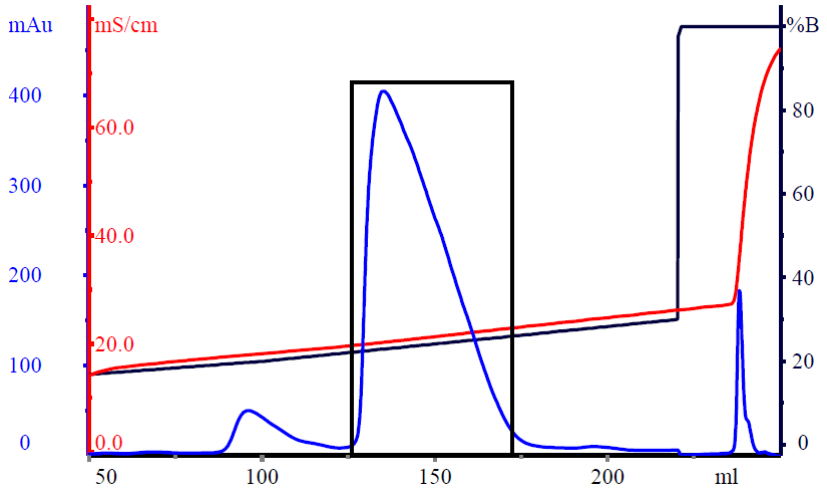

Figure 6.2: Chromatogram for the re-purification of [Fe_3S_4] D14C *P.f.* Fd on a 16/10 Source 30Q column. X-axis: elution volume; blue line: absorption at 280 nm; red line: conductivity; black line: NaCl concentration given as percent of 1 M NaCl.

6.3 Electrochemical Characterization of WT *Pyrococcus furiosus* Ferredoxin and Its D14C Mutant

In order to have a better overview, the results from electrochemical characterization of WT *P.f.* Fd and its D14C mutant are separated into two sections. The setup used for anaerobic electrochemistry is described in section 6.3.1.1 as well as preparation of the electrodes prior the experiment. All experiments were conducted in 20 mM Tris/HCl pH 8.0 buffer at 25 ± 2 °C. Neomycin is used as a promoter in all experiments (88), (89), (40). Mass spectrometric analysis was performed for [Fe_4S_4] and [Fe_3S_4] D14C *P.f.* Fd after the electrochemical experiment to detect possible changes in protein samples since the formation of a robust neomycin-Fd complex has been reported before for [Fe_3S_4] WT *P.f.* Fd (88).

6.3.1 Experimental

Concentrated protein samples in 20 mM Tris/HCl pH 8.0 were diluted prior to experiment using the same buffer to the final protein concentration of 40 µM which was determined by UV-vis spectrophotometry. The final volume of the protein solution in the electrochemical cell was 5 ml. Neomycin sulfate powder was added to the solution during experiments without further purification by dissolution in a small volume of the buffer solution and transferring this to the cell. It was added to the final concentration of 5 mM. The voltammograms were recorded over the region from 244 mV to -756 mV vs. SHE for various scan rates. After the electrochemical characterization, the D14C *P.f.* Fd protein samples were concentrated using a Vivacell 70 with a 5000 MWCO membrane,

washed twice with 20 mM Tris/HCl pH 8.0 to remove the excess promoter and prepared for the mass spectrometric analysis using the procedure described in section 4.3.1.

6.3.1.1 The Setup for Anaerobic Electrochemistry

The setup for the electrochemistry performed inside the anaerobic chamber was based on the in-house setup for electrochemical experiments (88). This setup is based on the one used for electrochemical studies of WT *P.f.* Fds by previous member of the Metalloprotein Chemistry and Engineering Group – Jytte Kristensen, and it is described in her Ph.D. Thesis (86). The main difference between these two systems is in the reference electrode. In this new setup, instead of a normal Ag/AgCl, a leak-free Ag/AgCl electrode was used.

It is a tree-electrode system with the electrochemical cell consisting of two chambers. The working electrode was an edge-plane pyrolytic graphite electrode (EPG) with d = 0.5 cm (Pine Instruments). Prior to each experiment the electrode was polished with SiC paper (2400 grid followed by 4000 grid), and then with ø = 1 µm and ø = 0.05 µm Al_2O_3 slurry. Afterwards, the electrode was ultrasonicated twice in water for 10 minutes to remove traces of Al_2O_3 slurry. With a sealed cap on the electrode surface, the electrode was transferred to the anaerobic chamber. The reference electrode used was a leak-free Ag/AgCl electrode (Harvard Apparatus, cat. no. 690023). The potential of the reference electrode was checked versus saturated calomel electrode (SCE) after each experiment. The counter electrode used in this setup was a home-made curled Pt-wire which was cleaned in a H_2-flame prior to use. Neomycin was added as a promoter to the protein solutions in all experiments (89), (88). All potentials were converted to E vs. SHE by addition of 0.244 V (92). The potentiostat used was an electrochemical analyzer/workstation, 700C Series (CH Instruments) controlled by the CH Instruments software.

6.3.2 Results and Discussion

6.3.2.1 $[Fe_4S_4]$ and $[Fe_3S_4]$ WT *P.f.* Fd

Figure 6.3 shows the cyclic voltammogram of $[Fe_4S_4]$ WT *P.f.* Fd.

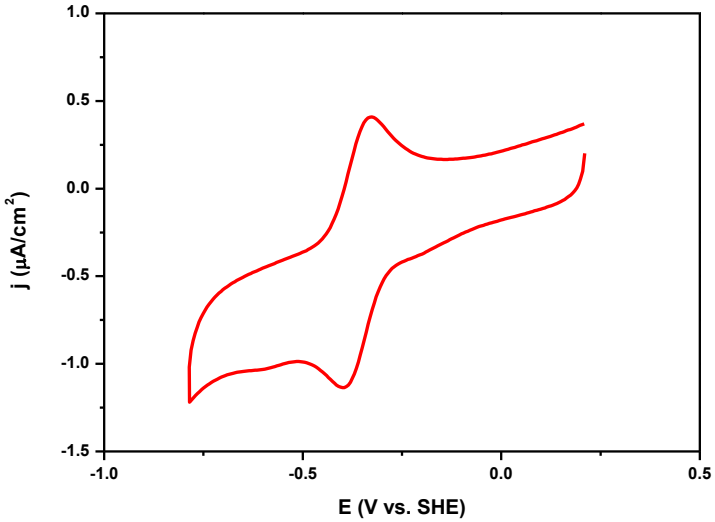

Figure 6.3: Cyclic voltammogram of 40 µM $[Fe_4S_4]$ WT *P.f.* Fd in 20 mM Tris/HCl pH 8.0 with 5 mM neomycin; scan rate 2 mV/s.

No signal was obtained in the absence of neomycin as a promoter, which agrees with previous observations (89; 91). Upon the addition of neomycin, one well-defined redox pair appeared. The formal potential was determined to -360 mV vs. SHE with the peak-peak separation of 60 mV at 2 mV/s scan rate. The signal is attributed to the $[Fe_4S_4]^{2+/+}$ redox couple (40). The voltammograms were stable up to 100 mV/s. The formal potential determined is in an agreement with the reported value for $[Fe_4S_4]^{2+/+}$ WT *P.f.* Fd using bulk solution cyclic voltammetry (89; 91).

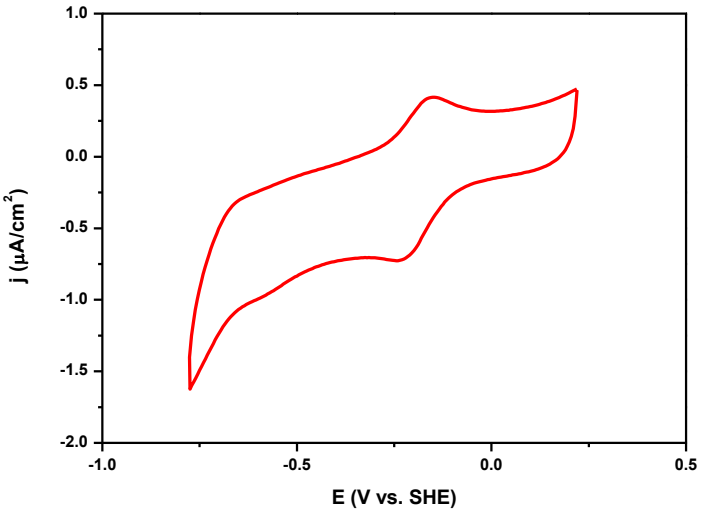

Figure 6.4: Cyclic voltammogram of 40 μM $[Fe_3S_4]$ WT *P.f.* Fd in 20 mM Tris/HCl pH 8.0 with 5 mM neomycin; scan rate 2 mV/s.

Figure 6.4 shows the cyclic voltammogram of $[Fe_3S_4]$ WT *P.f.* Fd. As expected, no redox couples were observed in the absence of neomycin (88; 89). One well-defined redox couple appeared upon addition of neomycin. The voltammograms remained stabile over various scan rates; from 2 mV/s upto 100 mV/s. The formal potential was determined to -189 mV vs. SHE with the peak-peak separation of 68 mV at 2 mV/s scan rate. The signal is attributed to the $[Fe_3S_4]^{+/0}$ couple (88; 89). Using these experimental conditions, the second redox couple assigned to $[Fe_3S_4]^{0/2-}$ couple reported in ref (89) was not observed. However, in ref (89) the cyclic voltammetry was performed under different experimental conditions such as pH, temperature and ionic strength. Also, in ref (88) the second redox couple was observed only after adding a second promoter. The cause of this was not further investigated in this study. The reduction potential determined for the $[Fe_3S_4]^{+/0}$ couple accords with the values reported before for a bulk solution cyclic voltammetry (88; 89), and also with those from the previous study of electrochemical properties of WT *P.f.* Fd described by Jytte Kristensen in her Ph.D. Thesis (86).

6.3.2.2 $[Fe_4S_4]$ and $[Fe_3S_4]$ D14C *P.f.* Fd

The cyclic voltammogram for $[Fe_4S_4]$ D14C *P.f.* Fd is shown in Figure 6.5. No signal was observed in the absence of neomycin. Upon adding up the promoter a well-defined redox signal appeared. The formal potential is determined to -431 mV vs. SHE with the peak-peak separation of 80 mV for 2 mV/s scan rate. This redox couple was assigned to the $[Fe_4S_4]^{2+/+}$ couple (41). The determined formal potential accords with the value previously reported for $[Fe_4S_4]^{2+/+}$ couple in D14C *P.f.* Fd using a differential pulse voltammetry (41).

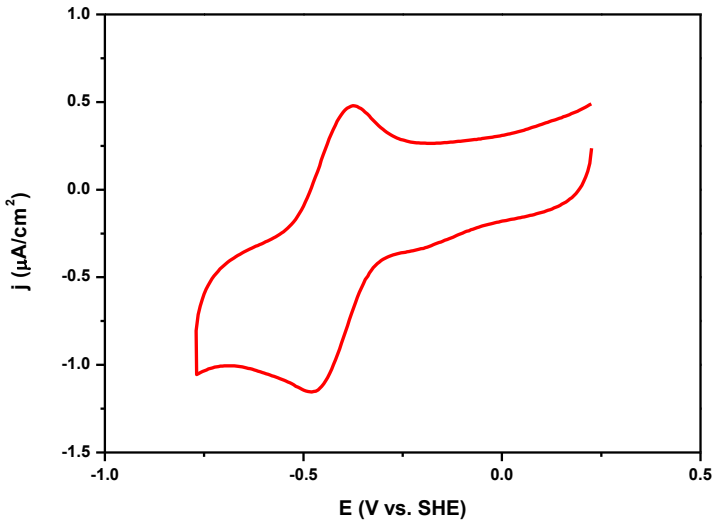

Figure 6.5: Cyclic voltammogram of 40 µM $[Fe_4S_4]$ D14C *P.f.* Fd in 20 mM Tris/HCl pH 8.0 with 5 mM neomycin; scan rate 2 mV/s.

The mass spectrum of the protein sample recorded after the electrochemistry experiment is shown in Figure 6.6.

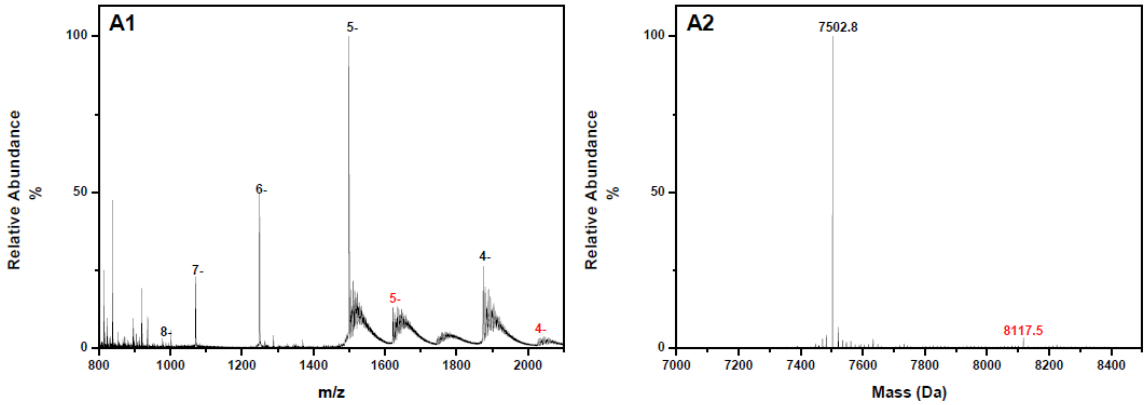

Figure 6.6: Mass spectrometric analysis spectra of $[Fe_4S_4]$ D14C *P.f.* Fd sample after the electrochemistry experiment. (A1) *m/z*- and (A2) mass spectra.

Two species are observed from the *m/z*-spectrum (spectrum A1). Five protein charge states are present for the dominating species (labelled in black), and only two protein charge states are present for the second species (labelled in red). A range from 1200 to 2100 of the *m/z*-spectrum was used for calculating the mass spectrum (see section 4.3.2). Two peaks are present in the mass spectrum – the apparent mass of the dominating species is 7502.8 Da which matches the expected mass for $[Fe_4S_4]^{2+}$ D14C *P.f.* Fd (see Table 4.1), and the second peak with an apparent mass of 8117.5 Da. The difference between these two masses is 615 Da which corresponds to the molecular mass of neomycin in neutral form. Thus, the formation of the complex between $[Fe_4S_4]^{2+}$ D14C *P.f.* Fd and neomycin in 1:1 ratio is observed, which was reported earlier for $[Fe_3S_4]$ WT *P.f.* Fd (88). The amount of the complex observed here is notably less than what was observed for $[Fe_3S_4]$ *P.f.* Fd in ref (88). This is most probably due to the differences in experimental conditions. In ref (88) protein sample was incubated in a solution with neomycin for 2-3 hours, then the protein sample was concentrated and buffer exchanged to water prior mass spectrometric analysis. Here, however, the protein

sample was prepared and analyzed by mass spectrometry immediately upon the electrochemistry experiment, as described in section 6.3.1. All protein samples, as described in section 4.3.1, were buffer-exchanged to NH_4Ac prior mass spectrometric analysis. Therefore, sample preparation could have influenced the change in the amounts of the observed species.

The cyclic voltammogram of $[Fe_3S_4]$ D14C *P.f.* Fd is shown in Figure 6.7.

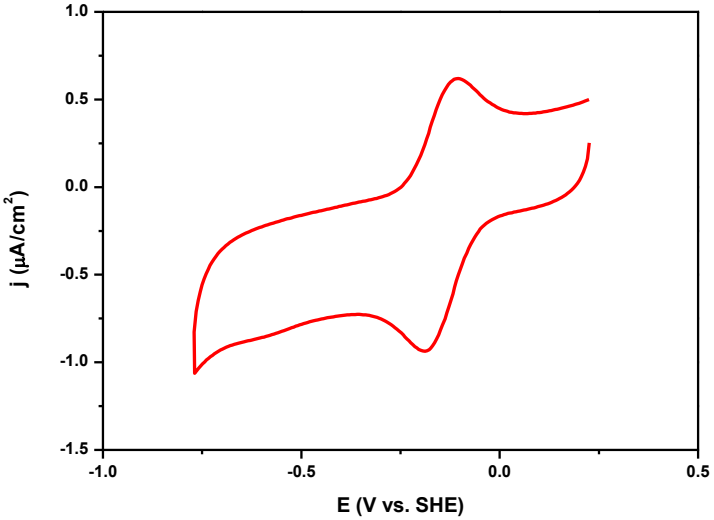

Figure 6.7: Cyclic voltammogram of 40 µM $[Fe_3S_4]$ D14C *P.f.* Fd in 20 mM Tris/HCl pH 8.0 with 5 mM neomycin; scan rate 2 mV/s.

As for the other forms, no signal was observed in the absence of neomycin. One well-defined redox couple appeared upon adding neomycin. The formal potential is determined to -155 mV vs. SHE. The signal was stabile over various scan rates; from 2 mV/s to 100 mV/s. The peak-peak separation is 80 mV at 2 mV/s scan rate, and the peak half-width of 76 mV indicates a one electron transfer couple. The peak current densities plotted versus the square root of the scan rate show linear dependency indicating the diffusion controlled system (data not shown).

Figure 6.8 shows the mass spectrum of the protein sample recorded after the electrochemistry experiment. Based on the mass spectrometric data, the formation of neomycin-$[Fe_3S_4]$ D14C *P.f.* Fd complex was observed here as well. From the *m/z*-spectrum is clear that two species are present (spectrum A1). The dominating species is labeled in black with 5 protein charge states present, while the second species is labeled in red with only two protein charge states present. The range of *m/z*-spectrum from 1400 to 2200 was used for calculating the mass spectrum A2. The dominating peak with the apparent mass 7447.9 Da matches the expected mass for $[Fe_3S_4]^+$ D14C *P.f.* Fd (see Table 4.1), and the second peak with apparent mass 8062.6 Da corresponds to the complex formed between $[Fe_3S_4]^+$ D14C *P.f.* Fd and neomycin (in neutral form) in 1:1 ratio. Based on the mass spectrometric data no other species were present in the protein solution. Even though the electrochemistry experiment was performed at pH 8.0 the formation of a disulfide bonded dimer under anaerobic conditions, as expected (see section 5.3.4), was not observed. The observed redox couple in Figure 6.7 is attributed to the monomer $[Fe_3S_4]^{+/0}$ D14C *P.f.* Fd.

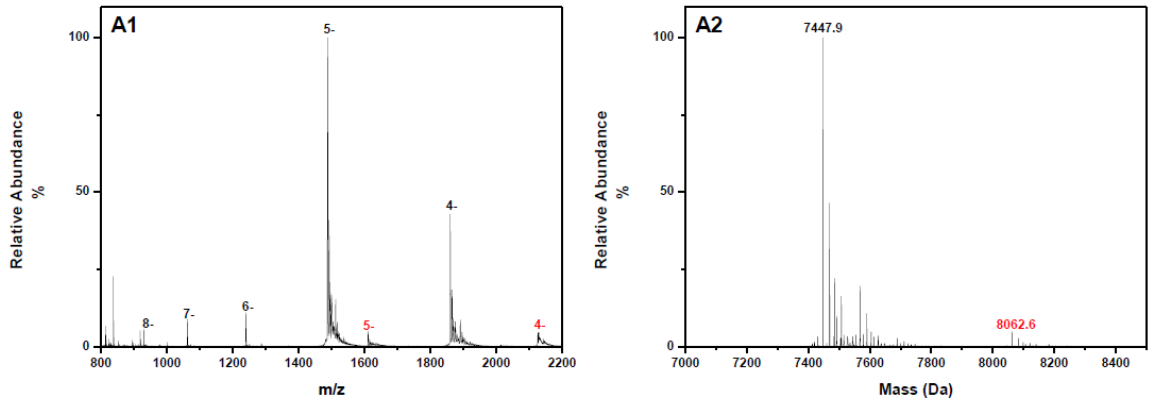

Figure 6.8: Mass spectrometric analysis spectra of [Fe_3S_4] D14C *P.f.* Fd sample after electrochemistry experiment was performed. (A1) *m/z* and (A2) mass spectra.

Hereby it was observed that neomycin has the same effect of the D14C variant as it has on WT *P.f.* Fd. The proposed mechanism of the promoting effect of neomycin suggested that *P.f.* Fd forms an intermediate complex with neomycin causing structural changes in the protein which open favorable electron transfer pathways and facilitate the access to the electrode surface (88). The observed protein-promoter complex formation from this section supports this mechanism.

Table 6.1 summarizes the obtained redox parameters for [Fe_4S_4] and [Fe_3S_4] WT *P.f.* Fd and its D14C mutant and as well as relevant literature data.

Table 6.1: Redox parameters of [Fe_3S_4] and [Fe_4S_4] WT *P.f.* Fd and D14C *P.f.* Fd in 20 mM Tris/HCl pH 8.0 with 5 mM neomycin; scan rate 2 mV/s. The literature reported data, given for comparison, are determined by a bulk solution voltammetry at pH 7.0. Potentials are given in mV vs. SHE.

P.f. Fd variant	E_a	E_c	ΔE	$E_{1/2}$	$E^{0'}$	$E^{0'}$ (42)
[Fe_4S_4] WT	-330	-390	60	61	-360	-368
[Fe_3S_4] WT	-155	-223	68	68	-189	-203
[Fe_4S_4] D14C	-391	-471	80	80	-431	-426
[Fe_3S_4] D14C	-117	-193	76	76	-155	-

The formal potential of [Fe_4S_4] D14C *P.f.* Fd is ~ 70 mV lower than for the [Fe_4S_4] WT *P.f.* Fd. This difference was explained comparing the pK_a values of the residue 14 (see section 3.4.2). Thus, Asp as a better electron withdrawing group compared to Cys stabilizes the reduced cluster (42). Therefore, the decrease in the formal potential was expected for the [Fe_4S_4] form of D14C *P.f.* Fd.

Compared to [Fe_3S_4] WT *P.f.* Fd the formal potential of [Fe_3S_4] D14C *P.f.* Fd has increased by ~ 35 mV. The electrochemistry experiment was performed at pH 8.0, and as previously discussed in section 5.3.4, at this pH Cys14 in [Fe_3S_4] D14C *P.f.* Fd, with pK_a value of 8.8, is only partly deprotonated. Compared to the [Fe_3S_4] WT *P.f.* Fd where Asp14 is fully deprotonated at pH 8.0, the charges on the [Fe_3S_4] cluster including ligands are different in these two variants: $[Fe_3S_4(CysS^-)_3(AspCOO^-)]^{3-}$ in WT *P.f.* Fd and $[Fe_3S_4(CysS^-)_3(Cys\text{-}SH)]^{2-}$ in D14C variant, and thus, because of more positive charge, the [Fe_3S_4] D14C *P.f.* Fd has a higher formal potential. Noteworthy is also the fact that

when compared to the ferredoxin II from *Desulfovibrio gigas* (*D.g.* FdII), and ferredoxin III from the D14C *Desulfovibrio africanus* FdIII (D14C *D.a*. FdIII), both having all-cysteine ligation of the $[Fe_3S_4]$ cluster, the formal potentials detemined for the $[Fe_3S_4]^{+/0}$ couple for all of them are within the same range; -155 mV for D14C *P.f*. Fd, -130 mV for *D.g*. FdII (93), and -125 mV for D14C *D.a*. FdIII (37).

6.4 Conclusions

Both WT *P.f*. Fd and its D14C variant were successfully anaerobically re-purified, and hereafter electrochemically characterized using a bulk solution cyclic voltammetry under anaerobic condition. The signals for both forms of WT *P.f*. Fd and D14C variant were well-defined and detected only in the presence of neomycin as a promoter. Based on the mass spectrometric data upon the electrochemical characterization both $[Fe_4S_4]$ and $[Fe_3S_4]$ D14C *P.f*. Fds have shown the formation of D14C *P.f.* Fd-promoter complex supporting the proposed mechanism of the promoting effect of neomycin

The formal potentials determined for $[Fe_4S_4]$ and $[Fe_3S_4]$ WT *P.f*. Fd, and for $[Fe_4S_4]$ D14C *P.f*. Fd accord with previously reported data. $[Fe_3S_4]$ D14C *P.f.* Fd is electrochemically characterized for the first time. A well defined redox couple was attributed to the $[Fe_3S_4]^{+/0}$. The determined formal potential is -155 mV vs. SHE.

.

7 Studies of Ferredoxins Containing [Zn-Fe_3S_4] Cluster

7.1 Introduction

This chapter describes the synthesis, purification, mass spectrometric analysis, electrochemical studies, and EPR spectroscopic studies of WT *P.f.* Fd and its D14C mutant containing the [Zn-Fe_3S_4] cluster. The synthesis, purification, and electrochemical characterization experiments were all performed under anaerobic conditions using the anaerobic chamber equipped as described in section 6.2.

The first synthesis of heterometallic [Zn-Fe_3S_4] cluster in ferredoxin was reported for *D.g.* FdII (94). Since then, the formation of [Zn-Fe_3S_4] cluster has also been reported for *D.a.* FdIII (95) and *P.f.* Fd (47). In previous studies of the [Zn-Fe_3S_4] cluster in WT *P.f.* Fd, the artificial ferredoxin was synthesized, desalted and subsequently characterized by EPR and Mössbauer spectroscopy, film voltammetry, and magenitic circular dichroism in order to determine magnetic, electronic and redox properties of the cluster (49; 47; 89). Reversible binding of cyanide and 2-mercaptoethanole as exogenous ligands at the Zn-site of the [Zn-Fe_3S_4] cluster in WT *P.f.* Fd was also reported (49).

This is the first multidisciplinary study of two ferredoxins containing the [Zn-Fe_3S_4] cluster. [Zn-Fe_3S_4] WT *P.f.* Fd and [Zn-Fe_3S_4] D14C *P.f.* Fd have been successfully synthesized and purified using various chromatographic techniques. Subsequently they were characterized by UV-vis spectrophotometry, mass spectrometric analysis, a bulk solution cyclic voltammetry, and EPR spectroscopy. Spin states were, however, not further investigated in this study.

7.2 Synthesis, Purification and Mass Spectrometric Characterization of Ferredoxins Containing [Zn-Fe_3S_4] Cluster

The protocol for the synthesis of [$ZnFe_3S_4$] cluster containing ferredoxins was developed based on previous reports for the synthesis of [$ZnFe_3S_4$] cluster in proteins (47; 49; 94). These procedures are all based on incubation (for 30 minutes) of reduced [Fe_3S_4] *P.f.* Fd with excess of metal ions followed by desalting.

The procedure used in this project for the synthesis and purification of ferredoxins containing the [Zn-Fe_3S_4] cluster is the same for both WT and D14C *P.f.* Fd and therefore these experimental procedures are given here together while the results and discussion sections are given separately.

7.2.1 Experimental

Aerobically purified protein sample (see section 5.2.2 and 5.2.3) containing 5 mg [Fe_3S_4] ferredoxin was transferred into the glove box, thawed and the protein solution was exchanged into 100 mM Mes/NaOH pH 6.3 using a Vivacell 70 (Sartorius Stedum Biotech) with a 5000 MWCO membrane. The protein sample was transferred to a glass vial supplied with a small magnet and diluted to 1.5 mL using the same buffer. 200 µL of 20 mM $Na_2S_2O_4$ was added and the solution was incubated for 10 min at room temperature with gentle stirring. 0.63 mg of $Zn(NO_3)_2 \cdot 6H_2O$ (5-fold molar excess) was dissolved in 300 µL Milli-Q water and added to the protein solution. The solution was incubated for 3 hours at room temperature with gentle stirring. The protein solution was

desalted using a PD – 10 column equilibrated with 20 mM Tris/HCl pH 8.0, and eluted using the same buffer. Hereafter, the protein sample was loaded onto a Q Sepharose Fast Flow column (CV ~ 3 mL) also equilibrated with 20 mM Tris/HCl pH 8.0. The column was first washed with 2 CV of 20 mM Tris/HCl pH 8.0, and the protein of interest was eluted isocratically using gravity chromatography with 20 mM Tris/HCl, 0.5 M NaCl pH 8.0. The protein solution was diluted 5 times using 20 mM Tris/HCl pH 8.0, and loaded onto a 16/10 Source 30Q equilibrated with the same buffer. The protein was eluted using a linear salt gradient from 0.1 to 0.4 M NaCl in 20 mM Tris/HCl pH 8.0 over 20 CV. Protein purification was performed on a HPLC system in anaerobic conditions and monitored at 280 nm. The fractions containing the protein of interest were collected and concentrated inside the glove box using a Vivacell 70 (Sartorius Stedum Biotech) with a 5000 MWCO membrane. The protein concentration was determined by UV-vis spectrophotometry, and the concentration for [Zn-Fe_3S_4] cluster containing ferredoxin was estimated using the molar extinction coefficient for [Fe_4S_4] WT *P.f.* Fd, ε_{390} = 17 $mM^{-1}cm^{-1}$ [30]. Afterwards, the protein sample was prepared for mass spectrometric analysis as described section 4.3.1.

7.2.2 Results and Discussion

Both ferredoxins behaved the same during the synthesis and the first two steps in the [Zn-Fe_3S_4] cluster containing ferredoxin protein purification. Therefore, only the final step of [Zn-Fe_3S_4] cluster containing ferredoxin purification will be discussed separately in this section.

Upon addition of $Na_2S_2O_4$ there was no visible change in the color of the protein solution. After addition of Zn^{2+} the color of the protein solution turned from brown to greenish brown. No precipitations were observed in the glass vial upon the 3 hours of incubation. A brown colored protein band was eluted from the PD – 10 column, and also a single brown colored band was eluted from the Q Sepharose Fast Flow column. No other colored speciess were observed. Since the initial anion exchange step using Q Sepharose Fast Flow column was not performed on HPLC, the brown colored protein was collected based on visually estimated elution.

7.2.2.1 [Zn-Fe_3S_4] WT *P.f.* Fd

Chromatogram for the purification of [Zn-Fe_3S_4] WT *P.f.* Fd on a 16/10 Source 30Q is shown in Figure 7.1. The collected fractions are marked with black boxes.

Three peaks, one major and two smaller peaks were observed from the purification – the first peak eluting at ~ 23.4 mS/cm, the second at ~ 24.9 mS/cm, and the third at ~ 27.6 mS/cm (see Figure 7.1) as compared to ~ 22.1 mS/cm for [Fe_4S_4] and ~ 23.9 mS/cm for [Fe_3S_4] WT *P.f*. Fd (see section 6.2.3.1). The concentrated fractions from each peak were analyzed by UV-vis spectrophotometry upon volume reduction. Figure 7.2 shows the normalized UV-vis spectra (according to the absorption at 280 nm) for the protein samples from all three chromatographic peaks. The spectrum of the protein from peak 1 shows an absorption maximum at 390 nm which is characteristic of [Fe_4S_4] cluster containing ferredoxin. The UV-vis spectra for the protein samples from the peaks 2 and 3 are bleached. In order to identify these three species, mass spectrometric analysis of these three samples was performed (as described in section 4.3.1).

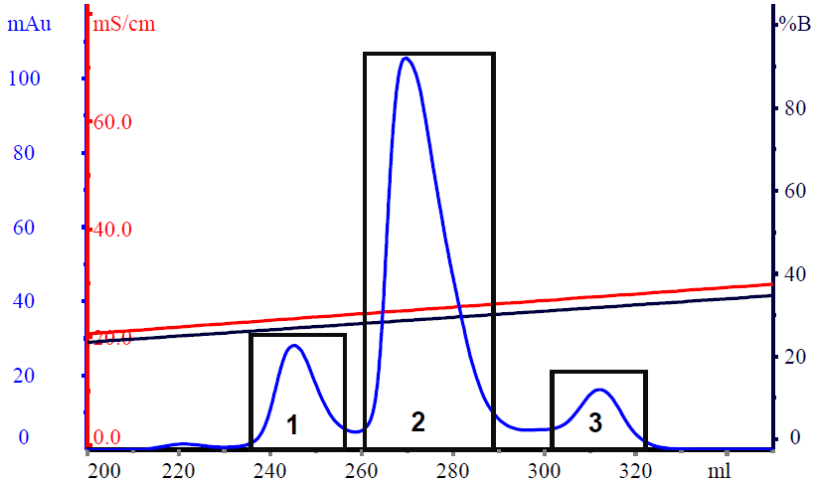

Figure 7.1: Chromatogram for the purification of [Zn-Fe_3S_4] WT *P.f.* Fd on a 16/10 Source 30Q column. X-axis: elution volume; blue line: absorption at 280 nm; red line: conductivity; black line: NaCl concentration given as percent of 1 M NaCl.

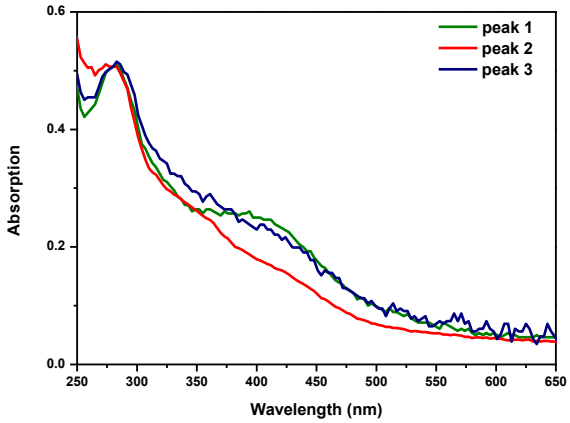

Figure 7.2: UV-vis spectra of the protein samples from the first (green), the second (red) and the third (blue) chromatographic peak in Figure 7.1. UV-vis spectra are normalized according to the absorbance at 280 nm.

Figure 7.3 shows the negative ion-mode mass spectra for all three samples. The *m/z*-spectra A1, B1 and C1 all show the presence of five protein charge states. Due to a low protein concentration and, in this case, not very efficient buffer exchange, the *m/z*-spectrum of the protein from the first chromatographic peak (spectrum A1) also shows some salt adducts present, especially for the low charge states. The *m/z*-range from 900 to 1300 was used for calculating the mass spectrum. The apparent mass from the spectrum A2 (see Figure 7.3) is 7514.5 Da which matches the expected mass for oxidized $[Fe_4S_4]^{2+}$ cluster containing WT *P.f.* Fd (see Table 4.1). This also confirms the assumption based on the UV-vis (see Figure 7.2). For calculating the mass spectrum for the protein from the second chromatographic peak the *m/z*-range from 800 to 1300 was used (see Figure 7.3, spectrum B1). The apparent mass is 7524.1 Da (see Figure 7.3, spectrum B2) which matches the expected mass for WT *P.f.* Fd containing [Zn-Fe_3S_4] cluster in 1+ oxidation state and one (Cys21-Cys48) disulfide bond (see Table 4.1). The protein sample from the third chromatographic peak has the apparent mass 7459.9 Da (see Figure 7.3, spectrum C2) which matches the expected mass for the oxidized $[Fe_3S_4]^{+}$ WT *P.f.* Fd (see Table 4.1). This is not in the agreement with the UV-vis spectrum in Figure 7.2 since the absorption maximum at 408 nm is not present here,

which is characteristic for $[Fe_3S_4]^+$ cluster. However, the concentration of the protein sample used for the mass spectrometric analysis was low, and even though the buffer exchange was performed (sample was sprayed from 100 mM NH_4Ac) it is obvious from its *m/z*-spectrum (spectrum C1) that there is still a lot of salt and buffer present in the sample. However, it was determined that the species present here contains the $[Fe_3S_4]$ cluster. Combining this fact with the UV-vis spectrum and the fact that this peak elutes app. ~ 3 mS/cm after oxidized $[Fe_3S_4]$ WT *P.f.* Fd (see section 6.2.3.1) leads to the conclusion that the $[Fe_3S_4]$ cluster is present in the reduced form.

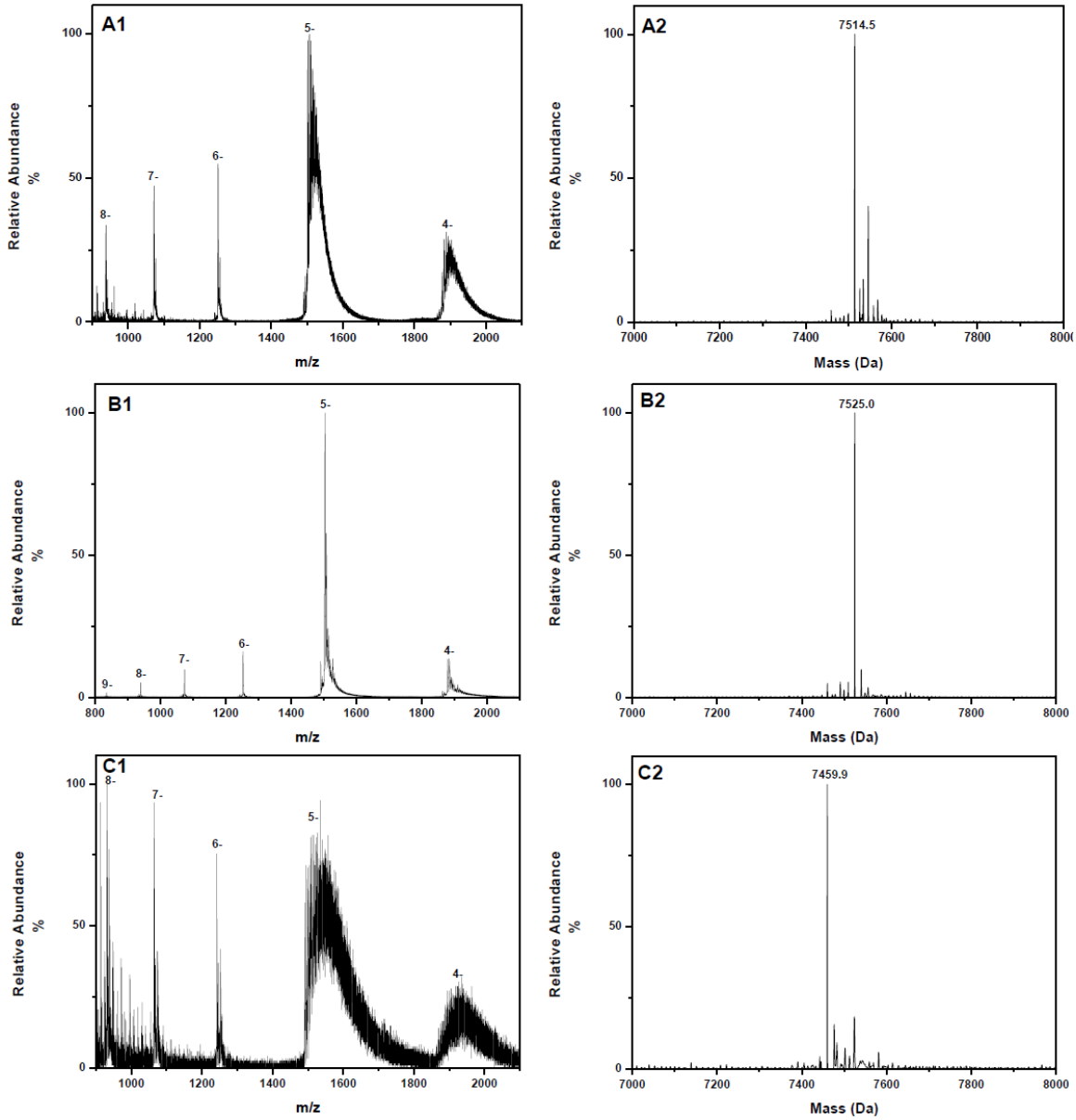

Figure 7.3: Mass spectrometric analysis spectra of the protein samples from the peaks from the chromatogram shown in Figure 7.1. (A1), (B1), (C1) – *m/z*- and (A2), (B2), (C2) – mass spectra of the samples from the first, second and third chromatographic peak, respectively.

These results clearly indicate that the major peak from the chromatographic purification belongs to $[Zn\text{-}Fe_3S_4]^+$ WT *P.f.* Fd. The yield of $[Zn\text{-}Fe_3S_4]$ WT *P.f.* Fd after purification and concentration was 1.7 mg (34.7 %) from 5 mg of $[Fe_3S_4]$ WT *P.f.* Fd.

7.2.2.2 [Zn-Fe_3S_4] D14C *P.f.* Fd

Figure 7.4 shows the chromatogram for the purification of [Zn-Fe_3S_4] D14C *P.f.* Fd on a 16/10 Source 30Q column. Only one peak is observed from the chromatogram eluting at ~ 25.5 mS/cm which is app. ~ 5 mS/cm higher than for oxidized [Fe_3S_4] D14C *P.f.* Fd (see section 6.2.3.2). The volume of the fractions corresponding to the peak was reduced, and the UV-vis spectrum was recorded (see Figure 7.5). The UV-vis spectrum appeared bleached. Mass spectrum of this species is shown in Figure 7.6.

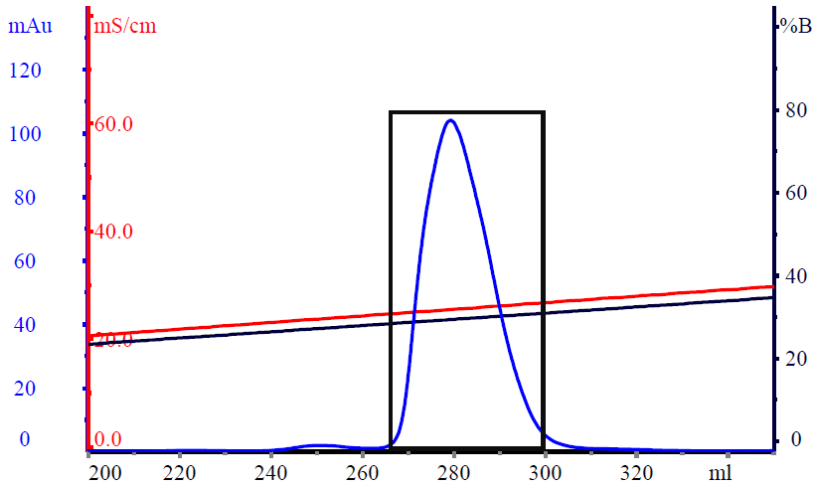

Figure 7.4: Chromatogram for the purification of [Zn-Fe_3S_4] D14C *P.f.* Fd on a 16/10 Source 30Q column. X-axis: elution volume; blue line: absorption at 280 nm; red line: conductivity; black line: NaCl concentration given as percent of 1 M NaCl.

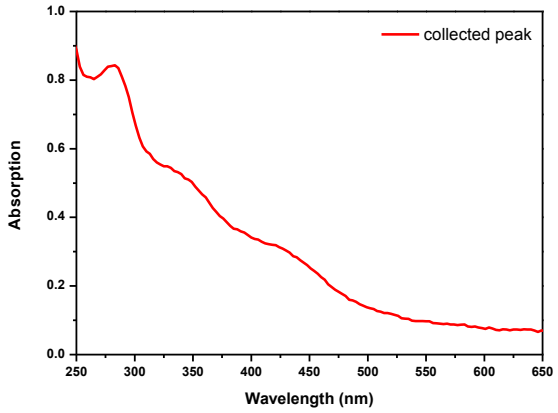

Figure 7.5: UV-vis spectrum of the protein sample from the chromatographic peak in Figure 7.4.

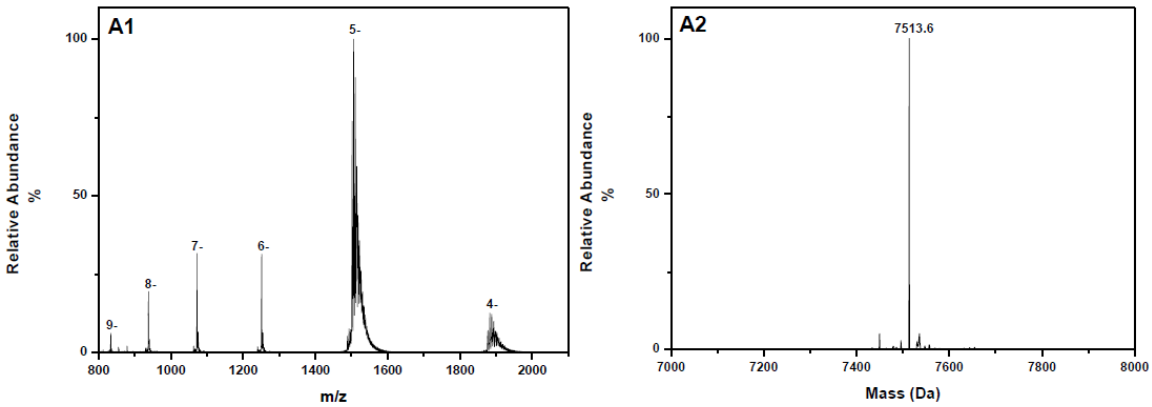

Figure 7.6: Mass spectrometric analysis spectra of the protein sample from the chromatographic peak in Figure 7.4. (A1) *m/z*- and (A2) mass spectra.

The mass spectrum A2 in Figure 7.6 shows that the purified peak contains almost exclusively one species. The apparent is 7513.6 Da which matches the expected mass for the novel [Zn-Fe_3S_4] D14C *P.f.* Fd containing the cluster in 1+ oxidation state with one (Cys21-Cys48) disulfide bond (see Table 4.1).

The yield of [Zn-Fe_3S_4]$^+$ D14C *P.f*. Fd was similar to the one observed for [Zn-Fe_3S_4] WT *P. f*. Fd – 1.8 mg (36 %) from 5 mg of [Fe_3S_4] D14C *P.f.* Fd.

7.3 Stability Studies of Ferredoxins Containing [Zn-Fe_3S_4] Cluster

Synthesized and purified ferredoxins containing [Zn-Fe_3S_4] cluster were tested towards different storage time, and towards oxygen exposure.

7.3.1 Experimental

Purified samples of [Zn-Fe_3S_4] cluster containing ferredoxins were concentrated and stored in 20 mM Tris/HCl pH 8.0, and hereafter kept at room temperature inside the glove box. The stability of [Zn-Fe_3S_4] cluster containing ferredoxins was tested by mass spectrometry.

Standard procedure was used to prepare the samples for the mass spectrometric analysis (see section 4.3.1). Mass spectra for the samples were recorded as listed:

A) on the day of the synthesis,
B) one week after the synthesis,
C) one month after the synthesis, and
D) 15 min after the sample had been exposed to oxygen.

7.3.2 Results and Discussion

Figure 7.7 shows the negative ion-mode spectra for both [Zn-Fe_3S_4] WT and [Zn-Fe_3S_4] D14C *P.f.* Fd after a month and after exposure to oxygen.

Freshly purified samples of [Zn-Fe_3S_4] WT and [Zn-Fe_3S_4] D14C *P.f.* Fd, as already seen in the section 7.2.2.1 and 7.2.2.1, contain [Zn-Fe_3S_4] cluster in the reduced form (1+ oxidation state). The samples remained unchanged after a week spent inside the glove box (data not shown). From the mass spectra recorded a month after a small portion of [Fe_3S_4] WT *P.f.* Fd (with apparent mass 7460.2 Da) in the [Zn-Fe_3S_4] WT *P.f.* Fd sample has appeared while [Zn-Fe_3S_4] D14C *P.f.* Fd sample has remained unchanged. Mass spectra of the samples were recorded after exposing them to oxygen for 15 min. The mass spectrum for the [Zn-Fe_3S_4] WT *P.f.* Fd sample indicates sensitivity of the cluster towards oxygen exposure. There are three major peaks present. The peak with the highest intensity has the apparent mass of 7459 Da corresponding to WT *P.f*. Fd containing oxidized [Fe_3S_4]$^+$ cluster. Two other peaks with the apparent masses 7513.6 Da and 7523.7 Da are observed. The peak with the apparent mass 7513.6 Da matches the expected mass for WT *P.f*. Fd containing oxidized [Fe_4S_4]$^{2+}$ cluster, while the peak with the apparent mass 7523.7 Da matches the expected mass for WT *P.f*. Fd containing oxidized [Zn-Fe_3S_4]$^{2+}$ cluster (see Table 4.1). The ratio between them is 2:1:1, respectively, meaning that oxygen exposure of [Zn-Fe_3S_4]$^+$ WT *P.f*. Fd resulted in > 75 % of the [Zn-Fe_3S_4] cluster being degraded into two species – 50 % to [Fe_3S_4]$^+$ and 25 % to

$[Fe_4S_4]^{2+}$ WT *P.f.* Fd, while the remaining 25 % was oxidized to $[Zn\text{-}Fe_3S_4]^{2+}$ WT *P.f.* Fd. For the $[Zn\text{-}Fe_3S_4]$ D14C *P.f.* Fd sample two major peaks are observed – the peak with the highest intensity with the apparent mass 7511.8 Da, and the second with the apparent mass 7447.9 Da. The ratio between these two peaks is 2:1, respectively. The peaks correspond to the expected mass for D14C *P.f.* Fd containing the oxidized $[Zn\text{-}Fe_3S_4]^{2+}$ cluster and oxidized $[Fe_3S_4]^{+}$ cluster, respectively (see Table 4.1), meaning that exposing this protein sample to oxygen for 15 min resulted in degradation ~ 33 % of the $[Zn\text{-}Fe_3S_4]^{+}$ to the $[Fe_3S_4]^{+}$ cluster.

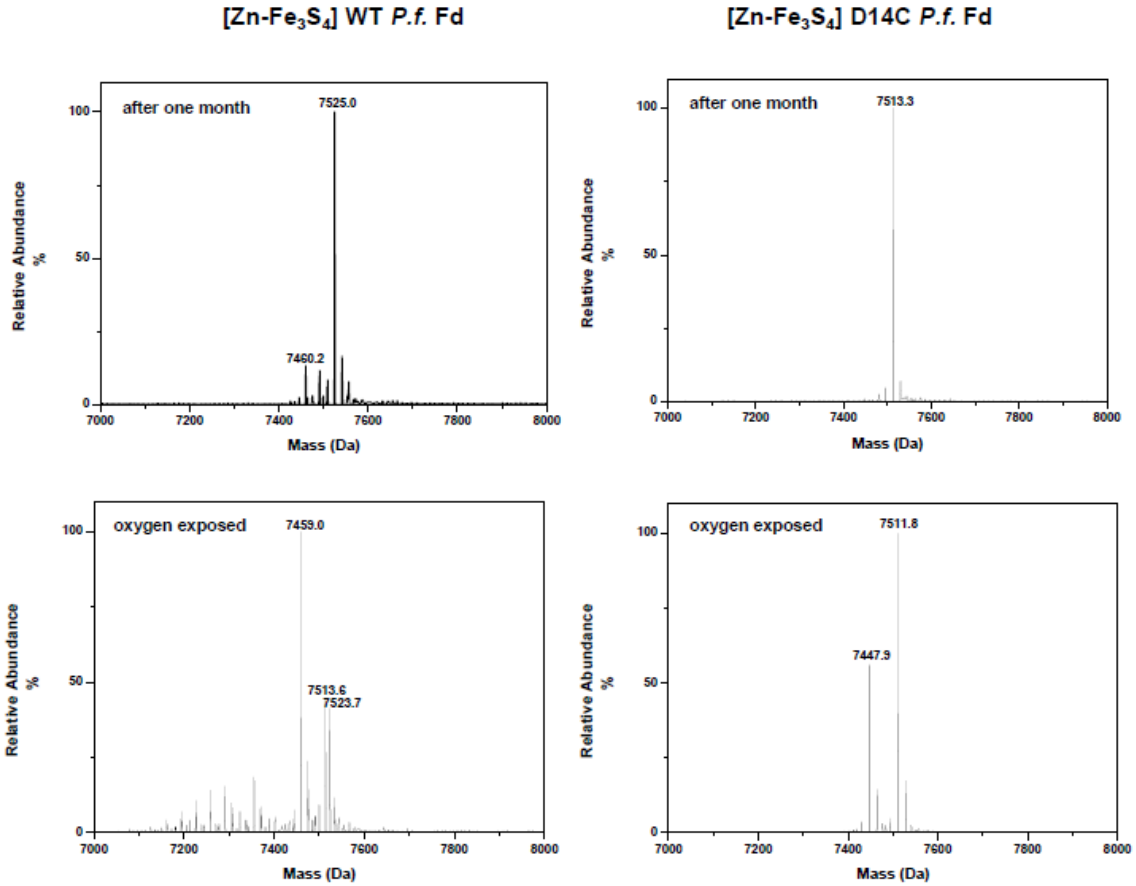

Figure 7.7: Mass spectra of the protein samples after a month and after exposure to oxygen. Left vertical lane is for $[Zn\text{-}Fe_3S_4]$ WT, and the right lane is for $[Zn\text{-}Fe_3S_4]$ D14C *P.f.* Fd samples.

Based on the mass spectrometric data for the oxygen exposed samples more than 75 % of the $[Zn\text{-}Fe_3S_4]$ cluster in WT *P.f.* Fd has been degraded to other species while ~ 70 % of the same cluster in D14C *P.f.* Fd remains intact. These observations suggest that the $[Zn\text{-}Fe_3S_4]$ cluster in the variant D14C is more inert towards oxygen exposure compared to the one in WT *P.f.* Fd, implying that increased stability of the heterometallic cluster in D14C variant stems from the replacement of aspartate ligation by cysteine. Thiolate (RS^-) is a stronger ligand for Zn^{2+} than carboxylate $RCOO^-$, and thus it has a stabilizing effect on the $[Zn\text{-}Fe_3S_4]$ cluster in D14C *P.f.* Fd.

7.4 Electrochemical Studies of Ferredoxins Containing $[Zn\text{-}Fe_3S_4]$ Cluster

The value for the formal potential of $[Zn\text{-}Fe_3S_4]^{2+/+}$ WT *P.f.* Fd has been previously reported using two independent methods – by dye-mediated EPR titrations (49), and

using film voltammetry (89). The formal potential for the [Zn-Fe_3S_4] cluster in the D14C variant has not been reported before.

Both [Zn-Fe_3S_4] WT and [Zn-Fe_3S_4] D14C *P.f.* Fds were characterized electrochemically using the setup described in section 6.3.1.1.

7.4.1 Experimental

The electrochemical experiments were performed the day after synthesis and purification of the [Zn-Fe_3S_4] cluster containing ferredoxins. Concentrated protein samples in 20 mM Tris/HCl pH 8.0 were left over night inside the glove box, and prior to the experiment the samples were diluted using the same buffer to the final protein concentration of 40 µM. Neomycin sulfate powder was added to the solution without further purification by dissolving it in a small volume of the protein solution and transferring this to the cell. The final concentration of neomycin in the protein solution was 5 mM. The electrodes were adequately prepared for the experiment (see section 6.3.1.1) and transferred into the glove box. Experiments were conducted at 25 ± 2 °C. Mass spectrometric analysis was used to characterize the protein samples before and after the electrochemistry using the procedure described in section 4.3.1.

7.4.2 Results and Discussion

7.4.2.1 [Zn-Fe_3S_4] WT *P.f.* Fd

Cyclic voltammogram of [Zn-Fe_3S_4] WT *P.f.* Fd is shown in Figure 7.9.

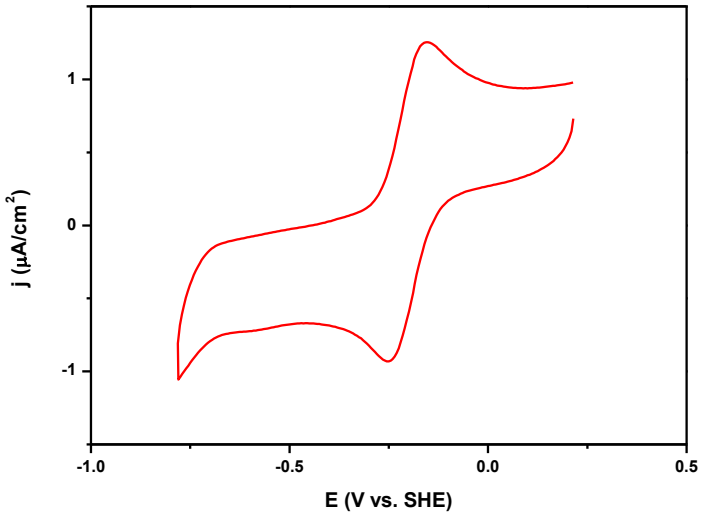

Figure 7.9: Cyclic voltammogram of 40 µM [Zn-Fe_3S_4] WT *P.f.* Fd in 20 mM Tris/HCl pH 8.0 with 5 mM neomycin; scan rate 2 mV/s.

The voltammograms were recorded over the region from 244 mV to -756 mV vs. SHE for various scan rates. No signal is obtained if neomycin is absent from the protein solution, as it was seen before for both [Fe_3S_4] and [Fe_4S_4] WT *P.f.* Fds (see chapter 6). Upon the addition of neomycin, one well-defined redox couple appeared. The formal potential determined is -206 mV. The voltammograms were stable up to 100 mV/s. The peak-peak separation at the scan rate 2 mV/s is 80 mV, and the peak half-width 57 mV suggesting one-electron transfer. Table 7.1 summarizes the redox parameters for [Zn-Fe_3S_4] WT *P.f.*

Fd, and those for $[Fe_3S_4]$ and $[Fe_4S_4]$ WT *P.f*. Fds previously determined in section 6.3.2.1.

Table 7.1: Redox parameters for $[Zn\text{-}Fe_3S_4]$, $[Fe_3S_4]$ and $[Fe_4S_4]$ WT *P.f*. Fd in 20 mM Tris/HCl pH 8.0 with 5 mM neomycin at 2 mV/s scan rate. Potentials are given in mV vs. SHE. Data for $[Fe_3S_4]$ and $[Fe_4S_4]$ WT *P.f*. Fd are experimental data from section 6.3.2.1.

	E_a	E_c	ΔE	$E_{1/2}$	$E^{0'}$
$[Zn\text{-}Fe_3S_4]$ WT *P.f*. Fd	-166	-246	80	57	-206
$[Fe_3S_4]$ WT *P.f*. Fd	-155	-223	68	68	-189
$[Fe_4S_4]$ WT *P.f*. Fd	-330	-390	60	61	-360

The formal potential obtained by EPR titrations at pH 7.6 for the $[Zn\text{-}Fe_3S_4]^{2+/+}$ couple in WT *P.f.* Fd is -241 ± 20 mV vs. SHE (49) while the value determined by film votammetry at pH 7.0 is -261 mV (89). The reported values are 40 to 60 mV more negative than the formal potential determined for the $[Fe_3S_4]^{+/0}$ WT *P.f*. Fd. In this study, however, the formal potential determined for the observed redox couple remains very close to the formal potential of the $[Fe_3S_4]^{+/0}$ couple from WT *P.f*. Fd (see Table 7.1).

The mass spectrometric data obtained after the electrochemistry experiment indicated change in the protein sample (see Figure 7.10). The mass spectrum of the protein sample before the electrochemistry experiment was identical to the one shown in section 7.2.2.1 containing exclusively reduced $[Zn\text{-}Fe_3S_4]^{+}$ WT *P.f*. Fd. Upon the electrochemistry experiment mass spectrometric data show presence of four different species. The *m/z*-spectrum A1 in Figure 7.10 shows the presence of two envelopes, each of them containing two species. Zoomed spectra (I) and (II) of the spectrum A1 (see Figure 7.10) offer a better overview.

The range from 1100 to 1700 from the *m/z*-spectrum was used for calculating the mass spectrum A2. The dominating peak with th apparent mass 7524.4 Da corresponds to the expected mass for WT *P.f*. Fd with $[Zn\text{-}Fe_3S_4]^{2+}$ cluster (see Table 4.1) while the peak with the apparent mass 7460.5 Da matches the expected mass for WT *P.f*. Fd containing reduced $[Fe_3S_4]^{0}$ cluster (see Table 4.1). The two peaks with the apparent masses 8139.1 and 8075.5 Da correspond exactly to the masses of neomycin complex formed with $[Zn\text{-}Fe_3S_4]^{2+}$ and $[Fe_3S_4]^{0}$ WT *P.f*. Fds in the 1:1 ratio, respectively.The formation of the protein-promoter complex accords with previously reported behavior for $[Fe_3S_4]$ WT *P.f.* Fd (88).

The mass spectrometric data show that ~ 33 % of $[Zn\text{-}Fe_3S_4]$ WT *P.f*. Fd has been degraded to $[Fe_3S_4]$ WT *P.f*. Fd during the electrochemical characterization suggesting that Zn^{2+} ion is being removed from the cluster upon cluster's oxidation. The sensitivity of the $[Zn\text{-}Fe_3S_4]$ cluster in WT *P.f*. Fd towards oxidation has been reported before (49; 89). Attempts to oxidize it with ferricyanide resulted in more than 50 % of it being degraded to the $[Fe_3S_4]$ cluster (49). Also, experiments conducted in order to determine the potential critical for metal-ion release from the $[M\text{-}Fe_3S_4]$ cluster resulted in complete degradation of the $[Zn\text{-}Fe_3S_4]$ cluster to the $[Fe_3S_4]$ after 10 minutes at 143 mV (89).

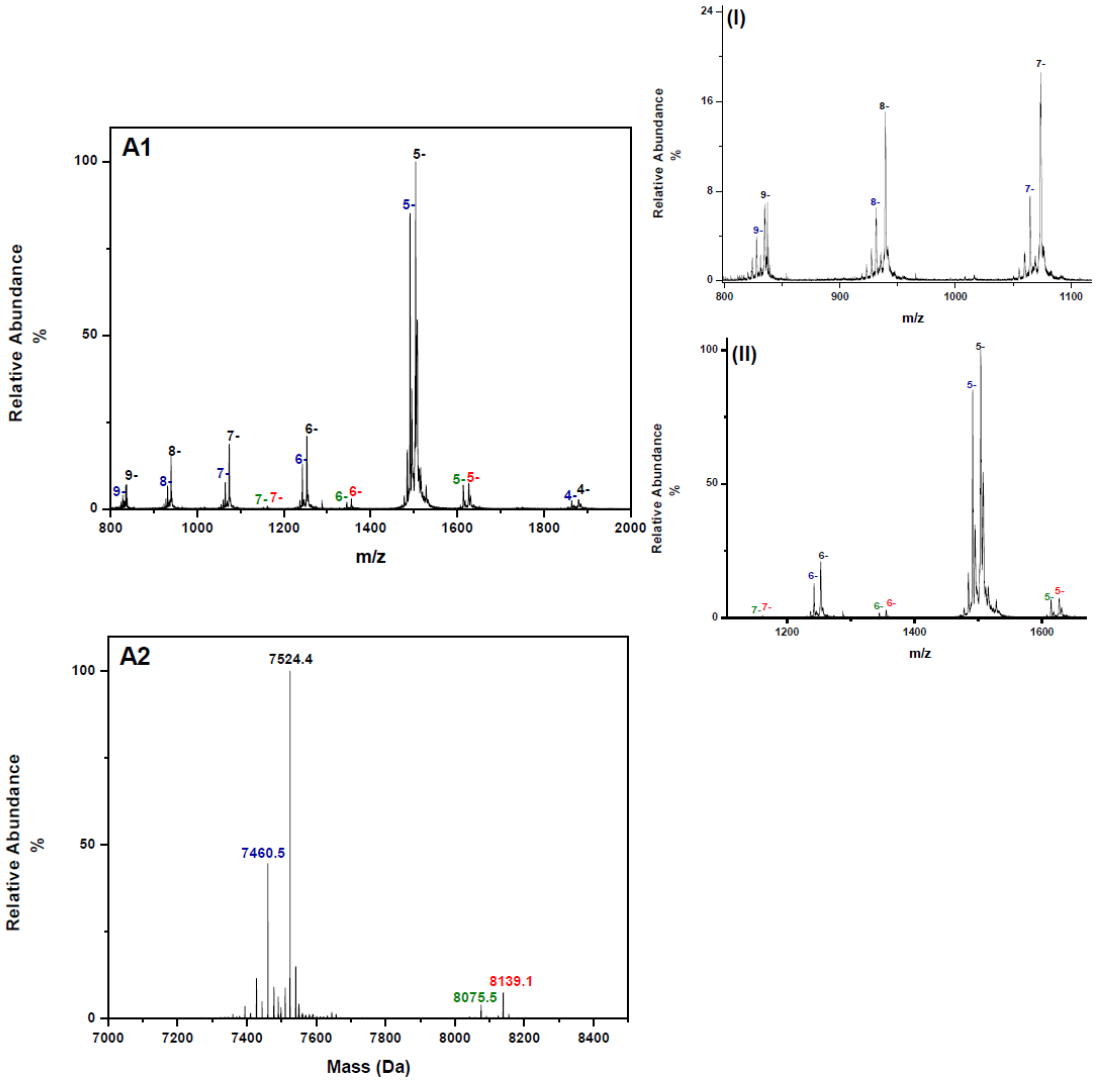

Figure 7.10: Mass spectrometric analysis spectra of [Zn-Fe_3S_4] WT *P.f.* Fd sample upon the electrochemistry experiment. (A1) *m/z*- and (A2) mass spectra. (I) zoomed spectrum A1 in the *m/z*-range from 800 to 1100 and (II) zoomed spectrum A1 in the *m/z*-range from 1100 to 1700.

The mass spectrometric analysis shows that degradation of the [Zn-Fe_3S_4] to the [Fe_3S_4] cluster in WT *P.f.* Fd occurs during the electrochemistry experiment, however, the votammograms were stable over various scan rates without any visible changes in the shape of the signal from the beginning of the experiment that could indicate the presence of some other species i.e. [Fe_3S_4] WT *P.f.* Fd in the system. Also, the current intensity of the signal obtained for the [Zn-Fe_3S_4] WT *P.f.* Fd is 4 to 5 times higher than the signal for the $[Fe_3S_4]^{+/0}$ couple in WT *P.f.* Fd. This difference is shown in Figure 7.11 where the voltammograms for the [Zn-Fe_3S_4] and [Fe_3S_4] WT *P.f.* Fd obtained under the same conditions and for the same protein concentrations are plotted together. The voltammogram shown for [Fe_3S_4] WT *P.f.* Fd is from the data obtained in section 6.3.2.1.

Despite the fact that there was no significant shift in the value for the formal potential compared to the $[Fe_3S_4]^{+/0}$ couple in WT *P.f.* Fd, it is argued here that the redox couple observed for [Zn-Fe_3S_4] WT *P.f.* Fd belongs to the $[Zn\text{-}Fe_3S_4]^{2+/+}$ couple with formal potential of -206 mV. This small difference in the formal potentials is assigned to redox inertness of Zn^{2+}. However, the effect of Zn^{2+} ion incorporation is quite notable from the

increased current intensity of the observed redox signal. Also, a fact that no significant changes in the voltammograms were observed during the electrochemistry experiment accords with it. A portion of [Fe_3S_4] WT *P.f.* Fd was, however, detected in the protein sample upon the electrochemistry experiment which is readily explained by the sensitivity of the [$ZnFe_3S_4$] cluster in WT *P.f.* Fd towards oxidation which has been reported before (49; 89). This portion of [Fe_3S_4] WT *P.f.* Fd could, however, give rise to a signal for the $[Fe_3S_4]^{+/0}$ couple, but the signal is most probably covered by the 5 times more intense signal arising from the $[Zn\text{-}Fe_3S_4]^{2+/+}$ couple.

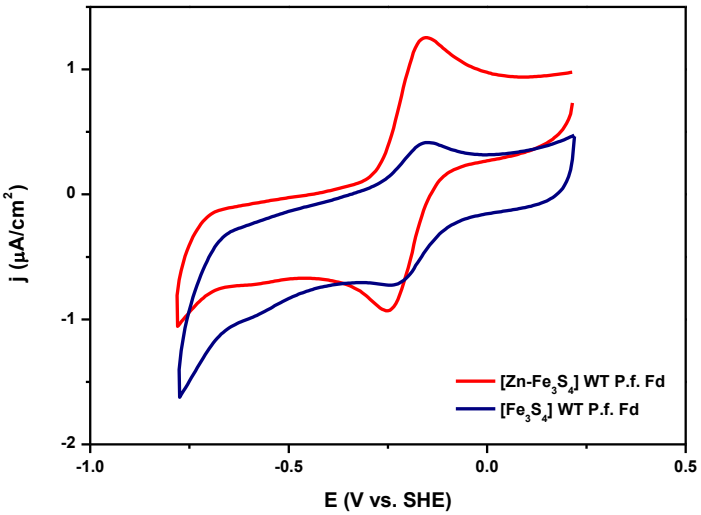

Figure 7.11: Cyclic voltammograms for [Zn-Fe_3S_4] WT *P.f.* Fd (red) and [Fe_3S_4] WT *P.f.* Fd (blue). Concentration of both proteins was 40 µM in 20 mM Tris/HCl pH 8.0 with 5 mM neomycin; scan rate 2 mV/s.

The difference between the values for the formal potential of the protein determined in this experimental setup compared to those obtained using EPR titrations (49) and film voltammetry (89) is attributed to arise due to different methods being used, including diffrent experimental conditions e.g. the pH value and the temperature. It is also important to point out that the protein sample used for electrochemical characterization in this study was sysnthesized, chromatographically purified and subsequently characterized prior to electrochemical measurements to containg only one species i.e. [$ZnFe_3S_4$] WT *P.f.* Fd. However, for the reported redox characterizations in ref (49; 89) only a raw protein sample purification consisting of buffer exchange procedure and/or gel filtration was used, thus, species other than [$ZnFe_3S_4$] WT *P.f.* Fd could be present in the samples.

7.4.2.2 [Zn-Fe_3S_4] D14C *P.f.* Fd

Cyclic voltammogram of [Zn-Fe_3S_4] WT *P.f.* Fd is shown in Figure 7.12. The voltammograms were recorded over the region from 244 mV to -1.256 V vs. SHE. No signal was observed in the absence of promoter. Upon its addition a well-defined redox couple was observed at higher potential values. The determined formal potential is -254 mV. The signal remained stable over various scan rates up to 60 mV/s. The peak-peak separation at the scan rate of 2 mV/s is 86 mV, and the peak half-width 70 mV suggesting one-electron transfer.

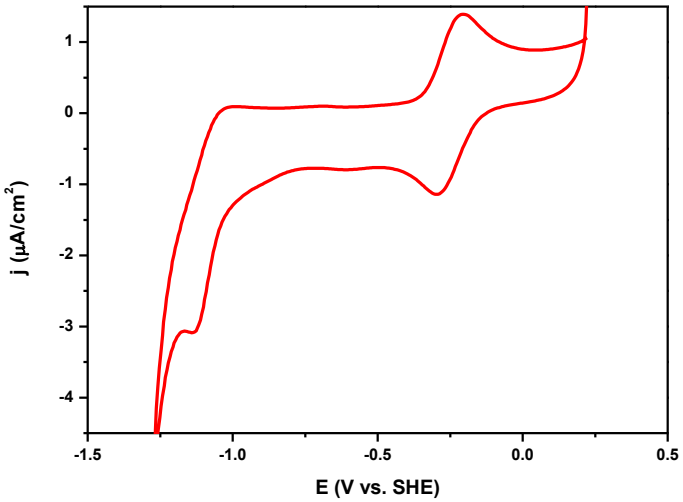

Figure 7.12: Cyclic voltammogram of 40 μM [Zn-Fe_3S_4] D14C *P.f.* Fd in 20 mM Tris/HCl pH 8.0 with 5 mM neomycin; scan rate 2 mV/s.

As observed for the [Zn-Fe_3S_4] cluster in WT *P.f.* Fd, the effect of the [Zn-Fe_3S_4] cluster to increase the current intensity of the redox signal compared to the [Fe_3S_4] cluster is visible here as well. In this case the current intensity was increased 2 to 3 times. Also, at lower potential value a cathodic peak is observed at ~ -1.13 V. Time constrains did not allow further investigation of the [Zn-Fe_3S_4] D14C *P.f.* Fd and assessment of the species observed at lower potential values. Thus, further insight into the redox properties of the [Zn-Fe_3S_4] D14C *P.f.* Fd is required.

Table 7.2 summarizes the redox parameters [Zn-Fe_3S_4] D14C *P.f.* Fd (only for the redox couple at higher potential value), and those for [Fe_3S_4] and [Fe_4S_4] D14C *P.f.* Fds previously determined in section 6.3.2.2.

Table 7.2: Redox parameters for [Zn-Fe_3S_4], [Fe_3S_4] and [Fe_4S_4] D14C *P.f.* Fd in 20 mM Tris/HCl pH 8.0 with 5 mM neomycin at 2 mV/s scan rate. Potentials are given in mV vs. SHE. Data for [Fe_3S_4] and [Fe_4S_4] D14C *P.f.* Fd are experimental data from the section 6.3.2.2.

	E_a	E_c	ΔE	$E_{1/2}$	$E^{0'}$
[Zn-Fe_3S_4] D14C *P.f.* Fd	-211	-297	86	70	-254
[Fe_3S_4] D14C *P.f.* Fd	-117	-193	76	76	-155
[Fe_4S_4] D14C *P.f.* Fd	-391	-471	80	80	-431

The mass spectrum of the protein sample obtained prior the electrochemical characterization is identical to the one recorded upon the synthesis and purification containing the reduced [Zn-Fe_3S_4]$^+$ D14C *P.f.* Fd (see section 7.2.2.2, Figure 7.6).

The mass spectrometric data for the sample upon the electrochemistry experiment show the presence of two species (see Figure 7.13). For calculating the mass spectrum A2, the range from 1100 to 1700 from the *m/z*-spectrum is used. The dominating peak with th apparent mass 7513.3 Da corresponds to the expected mass for D14C *P.f.* Fd with [Zn-Fe_3S_4]$^+$ cluster (see Table 4.1). The apparent mass of the second peak is ~ 615 Da higher corresponding to the mass of complex formed between [Zn-Fe_3S_4] D14C *P.f.* Fds

and neomycin in 1:1 ratio. It confirms the formation of protein-promoter complex here as well. No degradation of the [Zn-Fe_3S_4] cluster was observed.

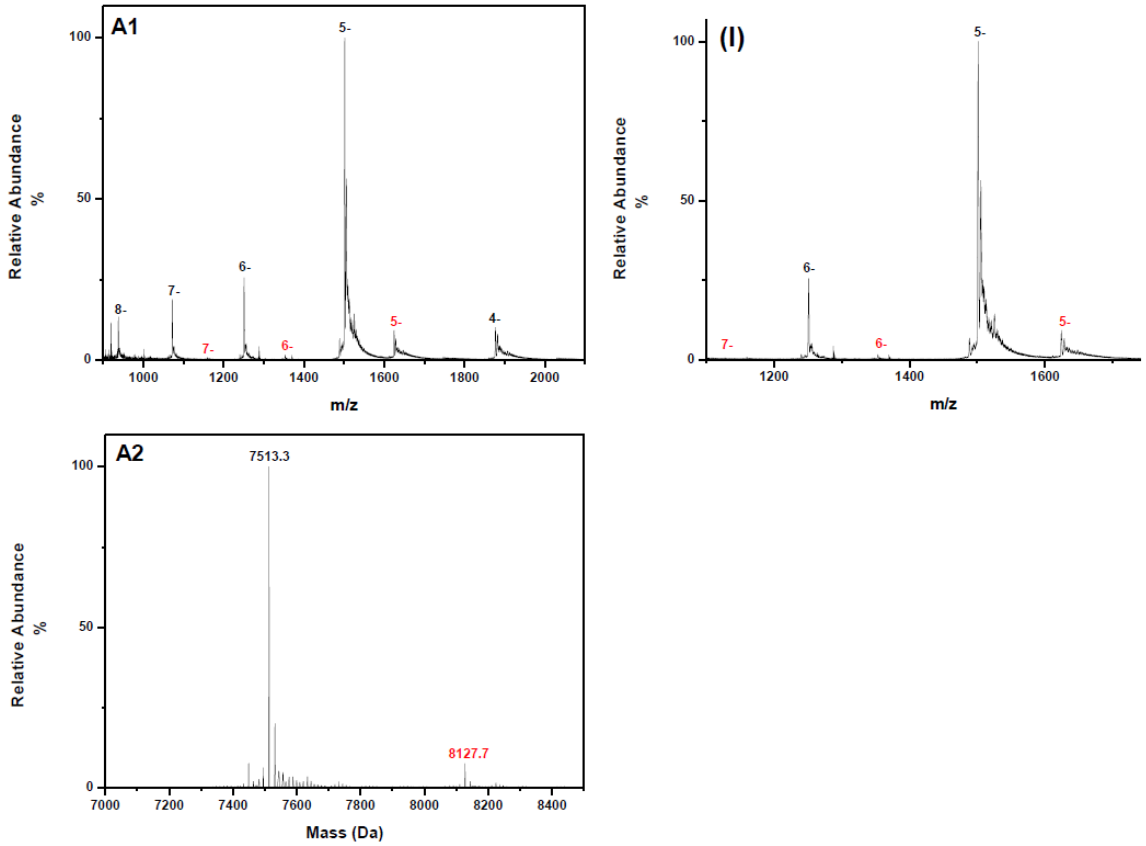

Figure 7.13: Mass spectrometric analysis spectra of [Zn-Fe_3S_4] D14C *P.f.* Fd sample upon the electrochemistry experiment. (A1) *m/z*- and (A2) mass spectra. (I) zoomed spectrum A1 in the *m/z*-range from 1100 to 1700.

As seen from the Table 7.2, the midpoint potential determined for [Zn-Fe_3S_4]$^{2+/+}$ D14C *P.f.* Fd couple is -254 mV. It is ~100 mV lower than the formal potential for the [Fe_3S_4]$^{+/0}$ couple, and ~180 mV higher than the formal potential for the [Fe_4S_4]$^{2+/+}$ couple in D14C *P.f.* Fd. As previously suggested [M-Fe_3S_4]$^{2+/+}$ cluster can be rationalized as a M^{2+} fragment coupled to a [Fe_3S_4]$^{0/-1}$ fragment (49; 50). According to this the [Fe_3S_4] fragment cycles between the [Fe_3S_4]^0 and [Fe_3S_4]$^-$ oxidation states in [M-Fe_3S_4] ferredoxins, while the [Fe_3S_4] ferredoxin cycles between the [Fe_3S_4]$^+$ and [Fe_3S_4]^0 states. Based on this model and the obtained data for the formal potentials (see Table 7.2), the incorporated Zn^{2+} stabilizes the reduced [Fe_3S_4]$^-$ state much more than the Fe^{2+} in the [Fe_4S_4] cluster. Also, based on this model the formal potentials for the [Fe_3S_4] and [Zn-Fe_3S_4] arise from two different redox couples. If compared to the trend observed for the WT *P.f.* Fd where potential for the [M-Fe_3S_4]$^{2+/+}$ couples increases in the order M = Fe < Zn, the same pattern is observed for the D14C variant.

7.5 EPR Spectroscopic Studies of Ferredoxins Containing [Zn-Fe_3S_4] Cluster

The first EPR spectroscopic characterization of [$ZnFe_3S_4$] cluster-containing ferredoxin has been reported for all-cysteinyl coordinated cluster in *D.g.* Fd (94). The ground spin states of the reduced and oxidized cluster were determined; S = 5/2 for the reduced

$[ZnFe_3S_4]^+$ cluster, and S = 2 for the oxidized $[ZnFe_3S_4]^{2+}$ cluster (47; 49). The $[ZnFe_3S_4]$ cluster in D14C *P.f.* Fd has not been characterized before however, similar features are expected as for the same cluster in *D.g.* Fd.

All EPR measurements in this section and section 8.5 were carried out at Delft University of Technology (TU Delft) by Professor Wilfred R. Hagen during my visit to his labs. X-band EPR spectra were recorded on a Bruker ECS 106 spectrometer with a home-built cooling flow system for liquid helium. The recorded spectra were analyzed using WR Hagen Visual Software programs (96). Quantification of intensity was performed by double integration. For molar quantification a copper standard was used (10 mM $CuSO_4$ in 10 mM HCl, 2 M $NaClO_4$).

7.5.1 Experimental

Samples of [Zn-Fe_3S_4] cluster containing WT *P.f.* Fd and its variant D14C were synthesized using the procedures given in section 7.2 and 7.3. Both protein samples were buffer exchanged to 20 mM Tris/HCl pH 8.0 and concentrated using a Vivacell 70 (Sartorius Stedum Biotech) with a 5000 MWCO membrane, and prepared, inside the glove box, for EPR measurements. Two sets of each protein sample were prepared – one “as-purified” protein sample, and one dithionite reduced sample (reduced with 10 mM dithionite from a freshly prepared solution of 1M $Na_2S_2O_4$ in 1M Tris/HCl pH 8.0). 200 µL of each sample was transferred into rubber-sealed quartz tubes, taken out of the glove box, and frozen in liquid nitrogen. Hereafter, the rubber lid was removed, frozen samples placed into the dry shipper (liquid nitrogen temperature, -196 °C), and shipped to TU Delft.

However, due to unexpected circumstances during the shipping process, samples were thawed and oxygen exposed prior arrival to TU Delft. Since most of the heterometalic-cluster-containing ferredoxins are oxygen sensitive some degradation of the samples was expected. However, these samples were used for EPR spectroscopic measurements.

The originally reduced sample, which arrived thawed, was frozen again in liquid nitrogen, and the EPR spectra were recorded. In further discussion this sample will be referred as the “oxygen exposed” sample. Afterwards, the sample was thawed, transferred to the glove box, and the “re-reduced” sample was prepared by re-reducing it with dithionate from a freshly prepared solution of 1M $Na_2S_2O_4$ in 1M Tris/HCl pH 8.0 to the final concentration of 10 mM $Na_2S_2O_4$ then incubated inside the glove box for 15 minutes, rubber-sealed, taken out of the glove box, and frozen in liquid nitrogen. Hereafter, the EPR spectra were recorded.

Upon EPR spectroscopic characterization frozen protein samples were shipped back in a dry shipped to our labs and the mass spectrometric analysis was performed (using the procedure described in section 4.3.1).

7.5.2 Results and Discussion

7.5.2.1 [Zn-Fe_3S_4] WT *P.f.* Fd

Figure 7.14 shows X-band EPR spectra in a perpendicular mode for the oxygen exposed and the re-reduced sample of [Zn-Fe_3S_4] WT *P.f.* Fd. The EPR spectrum of the oxygen

exposed sample (see Figure 7.14 A) shows a resonance signal at around 3400 Gauss (g ~ 2.02) which is typical for the S =1/2 system from the $[Fe_3S_4]^+$ cluster (30). This suggests that the [Zn-Fe_3S_4] cluster was degraded by the loss of Zn ion due to oxygen exposure. This was previously observed from the stability studies of [Zn-Fe_3S_4] WT *P.f.* Fd (see section 7.3); three species are detected from the mass spectrum upon its oxygen exposure – $[Fe_3S_4]$, $[Fe_4S_4]$ and [Zn-Fe_3S_4] WT *P.f.* Fd.

The EPR spectrum of the re-reduced protein sample is shown in Figure 7.14 B. Several species are observed from the spectrum. There are resonance signal observed at around 790 Gauss (g ~ 8.8) and 1350 Gauss (g ~ 5.1), and at around 3300, 3415 and 3600 Gauss (g ~ 2.1, 2.02 and 1.9, respectively). The resonance signal at g ~ 2.02 is typical for the S =1/2 system from the $[Fe_3S_4]^+$ cluster (30). The g-values g ~ 2.1 and 1.9 are characteristic for the reduced cluster $[Fe_4S_4]^+$ cluster (30) with the mixed S = 1/2 and S = 3/2 spin system. The resonance signals at g ~ 8.8 and g ~ 5.1 are typical for S = 5/2 system which is the ground spin state for the [Zn-Fe_3S_4]$^+$ cluster (47; 94). This suggests that upon the reduction some [Zn-Fe_3S_4]$^+$ cluster was re-built by incorporation of Zn-ion into the reduced $[Fe_3S_4]^0$ cluster.

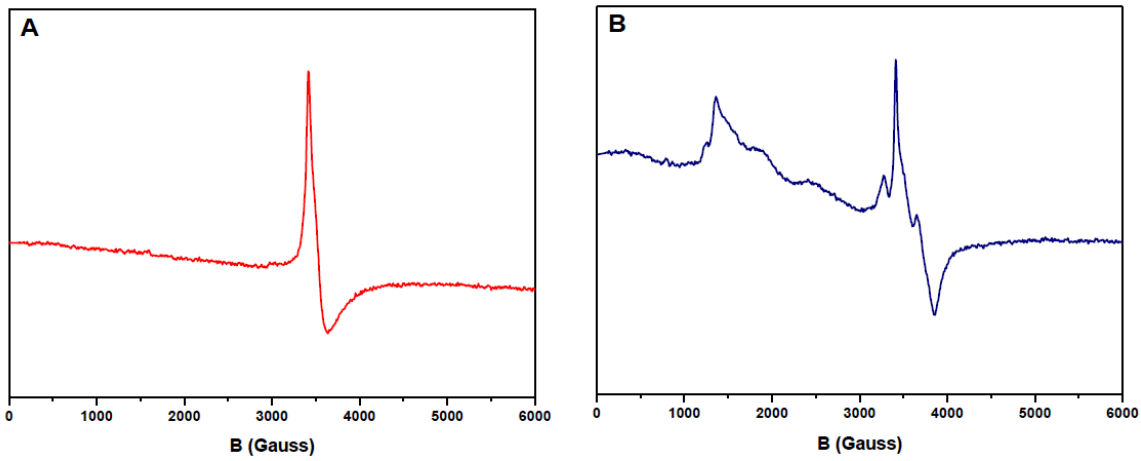

Figure 7.14: X-band EPR spectra in a perpendicular mode of 245 µM [Zn-Fe_3S_4] WT *P.f.* Fd in 20 mM Tris/HCl pH 8.0. (A) oxygen exposed sample, T = 10 K, v = 9.65 GHz, P = 2 dB, G = $1{\cdot}10^4$, and (B) re-reduced sample with 10 mM $Na_2S_2O_4$, T = 7.9 K, v = 9.65 GHz, P = 2 dB, G = $1{\cdot}10^5$.

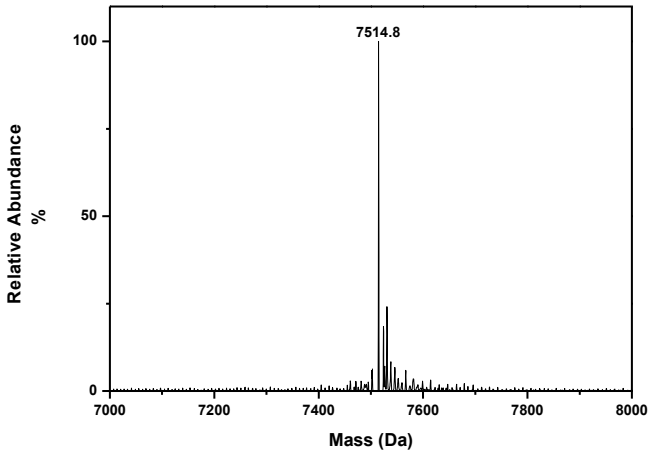

Figure 7.15: Mass spectrometric analysis spectrum of the [Zn-Fe_3S_4] WT *P.f.* Fd sample after EPR measurements.

However, the mass spectrum of the protein sample (see Figure 7.15) shows a presence of one species – $[Fe_4S_4]$ WT *P.f.* Fd. This is not consistent with the information gained from the EPR measurements but it can be attributed to the fact that a great part of the $[Zn\text{-}Fe_3S_4]$ cluster was already degraded due to oxygen exposure prior the EPR measurements when the mixture of three species was formed (see section 7.3), and under the reducing conditions the formation of the $[Fe_4S_4]$ cluster seems to be the favored process.

7.5.2.2 $[Zn\text{-}Fe_3S_4]$ D14C *P.f.* Fd

X-band EPR spectra in a perpendicular mode for the oxygen exposed and re-reduced sample of $[Zn\text{-}Fe_3S_4]$ D14C *P.f.* Fd are shown in Figure 7.16. The EPR spectrum of the oxygen exposed sample (Figure 7.16 A) shows the resonance signal at around 3400 Gauss (g ~ 2.02) which is typical for the S = 1/2 system from the $[Fe_3S_4]^+$ cluster (30) suggesting that the $[Zn\text{-}Fe_3S_4]$ cluster was degraded to the $[Fe_3S_4]^+$ cluster by the loss of Zn ion.

The EPR spectrum for the re-reduced sample (Figure 7.16 B) shows resonance signals at around 750 and 800 Gauss (g ~ 9.2 and 8.6, respectively) and at around 1300, 1450 and 1650 Gauss (g ~ 5.3, 4.8 and 4.2, respectively). These signal are typical for S = 5/2 system. The spectrum looks very similar and with similar parameters to the EPR spectra reported before for the $[Zn\text{-}Fe_3S_4]^+$ cluster in *D.g.* Fd (94) and in *P.f.* Fd (49). The differences are attributed to slightly different experimental conditions.

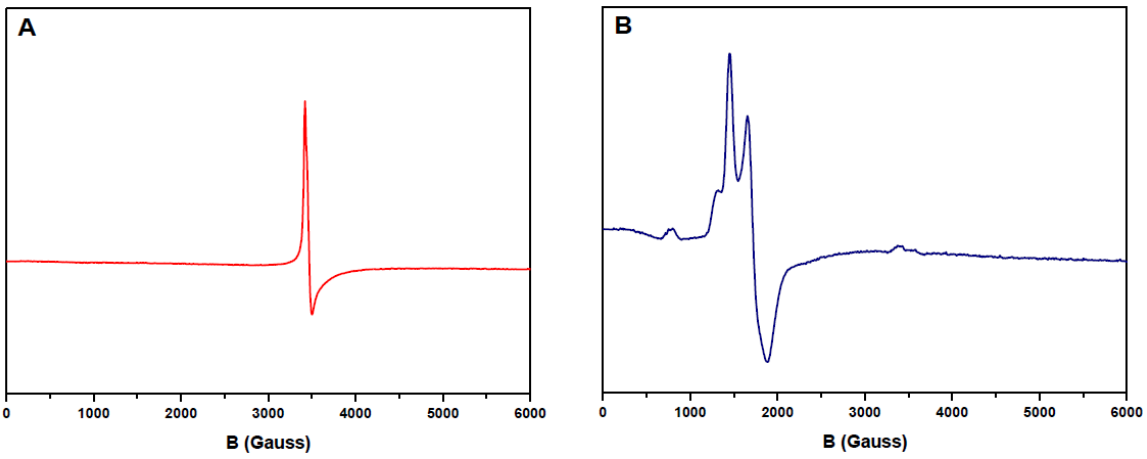

Figure 7.16: X-band EPR spectra in a perpendicular mode of 386 µM $[Zn\text{-}Fe_3S_4]$ D14C *P.f.* Fd in 20 mM Tris/HCl pH 8.0. (A) oxygen exposed sample, T = 10 K, v = 9.65 GHz, P = 2 dB, G = $1\cdot10^4$, and (B) re-reduced sample with 10 mM $Na_2S_2O_4$, T = 9.2 K, v = 9.65 GHz, P = 2 dB, G = $1\cdot10^5$.

Also, a very small signal is observed at around 3400 Gauss (g ~ 2.02) coming from traces of $[Fe_3S_4]^+$ Fd present present in the sample (see section 7.5.1). This also suggests that the most of the $[Zn\text{-}Fe_3S_4]$ cluster was re-built upon the reduction of the protein sample. Compared to the $[Zn\text{-}Fe_3S_4]$ cluster from WT *P.f.* Fd, the amount of the re-built cluster in the D14C variant is significantly bigger, again, suggesting the stabilizing effect of the cysteine 14 residue.

The mass spectrometric data (see Figure 7.17) are consistent with the EPR data – the species observed from the mass spectrum is D14C *P.f.* Fd containing the reduced

cluster [Zn-Fe_3S_4]$^+$. No [Fe_3S_4]$^+$ Fd is observed from the mass spectrum even though it can be seen from the EPR data which is attributed to the high sensitivity of the EPR technique.

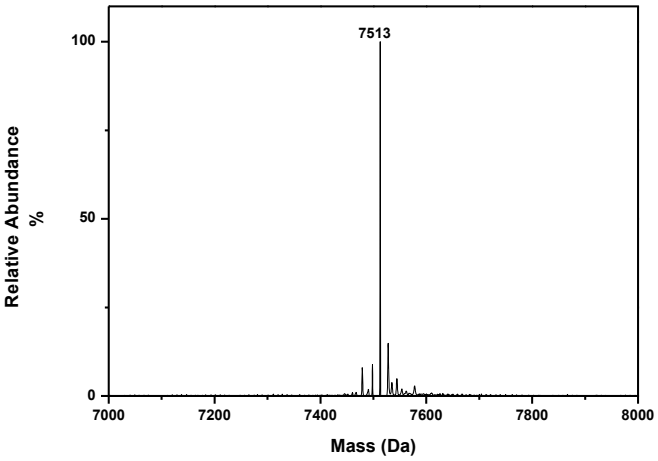

Figure 7.17: Mass spectrometric analysis spectrum of [Zn-Fe_3S_4] D14C *P.f.* Fd sample after EPR measurements.

7.6 Conclusions

Both the WT *P.f.* Fd and its variant D14C containing [Zn-Fe_3S_4] cluster were successfully synthesized and chromatographically purified under anaerobic conditions. The artificial ferredoxins were characterized by intact metalloprotein mass spectrometric analysis, electrochemistry and EPR spectroscopy.

Mass spectrometric data showed that the proteins were synthesized in a form containing the reduced cluster [Zn-Fe_3S_4]$^+$ and that a good separation was achieved during the purification procedure. Stability studies have shown that these artificial ferredoxins were stabile over a longer period of time in anaerobic conditions at room temperature while its exposure to oxygen causes cluster degradation. The [Zn-Fe_3S_4] cluster in the WT *P.f*. Fd appeared to be more oxygen sensitive than in the D14C *P.f*. Fd suggesting that Cys14 has a stabilizing effect on the [Zn-Fe_3S_4] cluster.

Both ferredoxins containing [Zn-Fe_3S_4] cluster were electrochemically characterized using a bulk solution cyclic voltammetry under anaerobic conditions with neomycin as a promoter. One well defined redox pair was observed in electrochemical characterization of each protein, and it was assigned to the [Zn-Fe_3S_4]$^{2+/+}$ couple. The formal potentials determined for the [Zn-Fe_3S_4] cluster in the WT *P.f.* Fd and in the D14C *P.f.* Fd are -206 mV and -254 mV vs. SHE, respectively.

The EPR spectroscopy has confirmed the presence of the [Zn-Fe_3S_4]$^+$ cluster in both WT and D14C *P.f*. Fd. The EPR spectra accord with EPR data reported for the [ZnFe_3S_4]$^+$ cluster in *D.g*. Fd (94) and in *P.f*. Fd (47; 49).

This was the first multidisciplinary study of the WT *P.f*. Fd and its D14C variant containing the [Zn-Fe_3S_4] cluster. The synthesis of the WT *P.f*. Fd containing the [Zn-Fe_3S_4] cluster has been reported before, however, only a raw purification of the reaction mixture was performed which was afterwards characterized by various techniques. In this study, the synthesis of the artificial ferredoxins with chromatographic purification of

the product and their characterization using the intact metalloprotein mass spectrometric analysis, cyclic voltammetry and EPR spectroscopy was performed. The D14C *P.f*. Fd containing heterometallic cluster has not been reported before. The D14C *P.f*. Fd variant containing the [Zn-Fe_3S_4] cluster was synthesized and characterized for the first time using this multidisciplinary approach.

8 Studies of Ferredoxins Containing [Ag-Fe_3S_4] Cluster

8.1 Introduction

This chapter describes the synthesis, purification, mass spectrometric analysis, stability, electrochemical and EPR studies of WT and D14C *P.f.* Fds containing the [Ag-Fe_3S_4] cluster. The synthesis, purification, and electrochemical characterization experiments from this chapter were all performed under anaerobic conditions using the anaerobic chamber equipped as described previously (see section 6.2).

Heterometallic cubanes involving the [Ag-Fe_3S_4] cluster have never been sysnthesized in proteins before. Holm *et al.* have, however, reported two synthetic analogues of the cluster which were characterized by H^1 NMR and cyclic votammetry (97).

In this study Ag^+ was used for incorporation into the [Fe_3S_4] cluster in WT *P.f.* Fd and its D14C variant. Two heterometallic ferredoxins have been successfully synthesized and purified – [Ag-Fe_3S_4] WT *P.f.* Fd and [Ag-Fe_3S_4] D14C *P.f.* Fds. Subsequently they were characterized by UV-vis spectrophotometry, mass spectrometric analysis, a bulk solution cyclic voltammetry, and EPR spectroscopy.

8.2 Synthesis, Purification and Mass Spectrometric Characterization of Ferredoxins Containing [Ag-Fe_3S_4] Cluster

The procedure used for the synthesis and purification of [Ag-Fe_3S_4] cluster containing ferredoxin is the same for both WT and D14C *P. f.* ferredoxin. Therefore, these experimental procedures are given together.

8.2.1 Experimental

Aerobically purified protein sample (see section 5.2.2 and 5.2.3) containing 5 mg [Fe_3S_4] ferredoxin was transferred into the glove box, thawed and the protein solution was exchanged into 100 mM Mes/NaOH pH 6.3 using a Vivacell 70 (Sartorius Stedum Biotech) with a 5000 MWCO membrane. The protein sample was transferred to a glass vial supplied with a small magnet and diluted to 1.5 mL using the same buffer. 200 µL of 20 mM $Na_2S_2O_4$ was added and the solution was incubated for 10 min at room temperature with gentle stirring in order to reduce the $[Fe_3S_4]^+$ ferredoxin. 1.13 mg of $AgNO_3$ (10-fold molar excess) was dissolved in 300 µL Milli-Q water and added to the protein solution. The solution was incubated for 3 hours at room temperature with gentle stirring. Hereafter, the protein solution was desalted using a PD – 10 column equilibrated with 20 mM Tris/HCl pH 8.0, and eluted using the same buffer. Hereafter, the protein sample was loaded onto a Q Sepharose Fast Flow column (CV ~ 3 mL) also equilibrated with 20 mM Tris/HCl pH 8.0. The column was first washed with 2 CV of 20 mM Tris/HCl pH 8.0, and the protein of interest was eluted isocratically with 20 mM Tris/HCl, 0.5 M NaCl pH 8.0 using gravity chromatography. The protein solution was diluted 5 times with 20 mM Tris/HCl pH 8.0, and loaded onto a 16/10 Source 30Q previously equilibrated with the same buffer. The protein was eluted using a linear salt gradient from 0.1 to 0.4 M NaCl in 20 mM Tris/HCl pH 8.0 over 20 CV. The fractions containing the protein of interest were collected and concentrated inside the glove box using a Vivacell 70 (Sartorius Stedum Biotech) with a 5000 MWCO membrane. The protein concentration was determined by UV-vis spectrophotometry, and the concentration of [Ag-Fe_3S_4]

cluster containing ferredoxin was estimated using the molar extinction coefficient for $[Fe_4S_4]$ WT *P.f.* Fd, ε_{390} = 17 $mM^{-1}cm^{-1}$. Hereafter, the protein sample was prepared for mass spectrometric analysis (see section 4.3.1).

8.2.2 Results and Discussion

Since the initial anion exchange step using a Q Sepharose Fast Flow column was not performed on HPLC, the brown colored protein was collected based on visually estimated elution. Protein purifications performed on HPLC system under anaerobic conditions were monitored at 280 nm.

Upon addition of $Na_2S_2O_4$ there was no visible change in the color of the protein solution. After addition of Ag^+ the color of the protein solution turned from brown to reddish brown. Some precipitations were observed since the magnet in the glass vial slows down upon the addition of Ag^+ ions. A single brown colored protein band was eluted from the PD – 10 column. Hereafter, a brown colored protein band was eluted from a Q Sepharose Fast Flow column with 20 mM Tris/HCl, 0.5 M NaCl pH 8.0, while another brown colored band remained on the column. First 1 M NaCl solution was used to remove the remaining band. However, one part of the band was eluted, while the major part of it remained on the column. Hereafter, 1 M NaOH solution was used, and again, a part of the brown colored band was eluted while the major part of it still remained on the column. Afterwards, the column was washed several times with Milli – Q water followed by 1 M HCl solution. However, the remaining brown colored band couldn't be removed, and therefore the column had to be discarded. This clearly indicated that the synthesis of $[Ag\text{-}Fe_3S_4]$ cluster containing ferredoxin is followed by other co-products.

8.2.2.1 $[Ag\text{-}Fe_3S_4]$ WT *P.f.* Fd

Chromatogram for the purification of $[Ag\text{-}Fe_3S_4]$ WT *P. f.* Fd on a 16/10 Source 30Q is shown in Figure 8.1. The collected fractions are marked with black boxes.

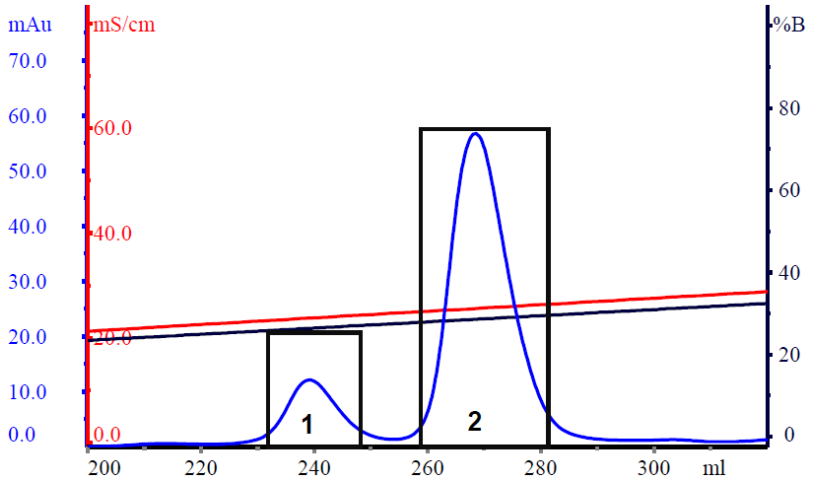

Figure 8.1: Chromatogram for the purification of $[Ag\text{-}Fe_3S_4]$ WT *P.f.* Fd on a 16/10 Source 30Q column. X-axis: elution volume; blue line: absorption at 280 nm; red line: conductivity; black line: NaCl concentration given as percent of 1 M NaCl.

Two peaks, one major and one smaller were observed from the purification – peak 1 eluting at 23.6 mS/cm, and peak 2, the major peak, at 25.6 mS/cm (see Figure 8.1) while $[Fe_4S_4]$ Fd elutes at ~ 22.1 mS/cm and $[Fe_3S_4]$ Fd at ~ 23.9 mS/cm for WT *P.f* (see section 6.2.3.1). The peak separation corresponds to the one observed for the

purification of [Zn-Fe_3S_4] cluster containing ferredoxin, see Figure 7.1. Therefore, the first peak is already at this stage assumed to contain $[Fe_4S_4]^{2+}$ ferredoxin, while the second peak is expected to be [Ag-Fe_3S_4] cluster containing ferredoxin. The concentrated fractions from each peak were analyzed by UV-vis spectrophotometry upon volume reduction. Figure 8.2 shows the normalized UV-vis spectra (according to the absorption at 280 nm) for both chromatographic peaks. The spectrum of the protein sample from the peak 1 shows an absorption maximum at 390 nm which is characteristic of $[Fe_4S_4]^{2+}$ cluster containing ferredoxin, while the UV-vis spectrum for the second peak looks bleached compared to the UV-vis spectrum of the first peak, and also compared to the UV-vis spectrum of $[Fe_3S_4]^{+}$ WT *P.f.* Fd, see Figure 5.3.

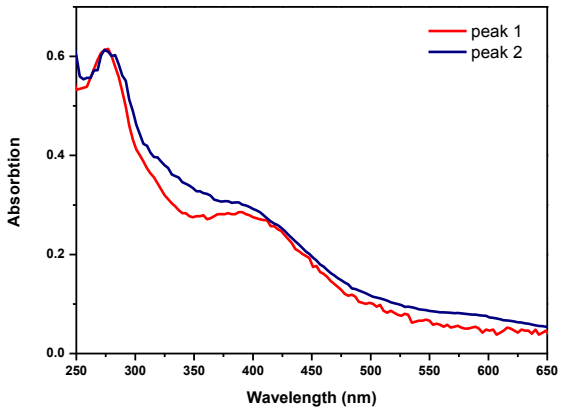

Figure 8.2: UV-vis spectra of the protein samples from the first (red) and the second (blue) chromatographic peak in Figure 8.1. UV-vis spectra are normalized according to the absorbance at 280 nm.

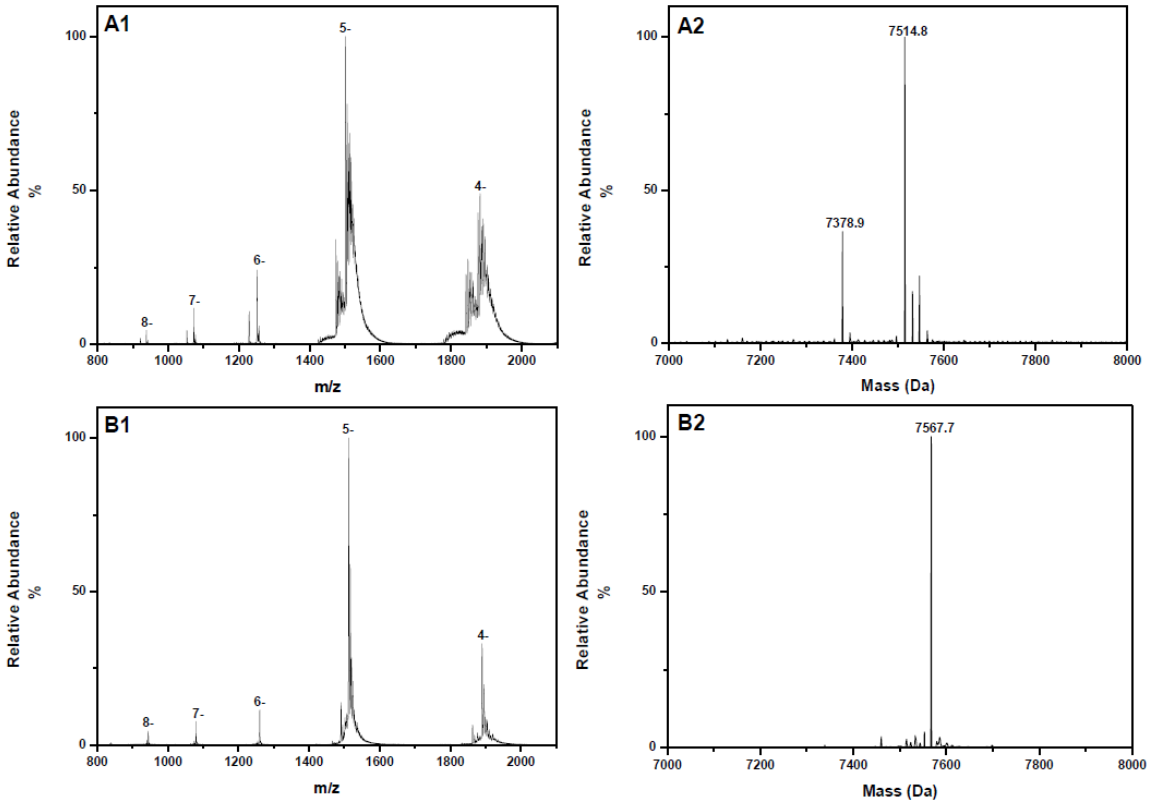

Figure 8.3: Mass spectrometric analysis spectra of the protein samples from the chromatographic peaks in Figure 8.1. (A1), (B1) – *m/z*- and (A2), (B2) – mass spectra of the samples from the first and the second chromatographic peak in Figure 8.1, respectively.

Figure 8.3 shows the negative ion-mode mass spectra for both protein samples. The *m/z*-spectra A1 and B1 show the presence of five different protein charge states. Higher charge states (e.g. 8-, 7- and 6-) are as expected adducts-free (see section 4.1.1.4). Due to the low protein concentration and not that efficient buffer exchange the *m/z*-spectrum of the protein sample from the first chromatographic peak (spectrum A1) shows also some salt adducts present, especially for the lower charge states, i.e. 5-, 4- and 3-. The apparent mass from the spectrum A2 (see Figure 8.3) is 7514.5 Da which matches the expected mass for the $[Fe_4S_4]^{2+}$ cluster containing WT *P.f.* Fd (see Table 4.1). This also confirms the assumption based on the UV-vis (see Figure 8.2). Also, the second species with the apparent mass 7378.9 Da is present suggesting that the $[Fe_4S_4]$ cluster is being further degraded during the synthesis. The apparent mass for the second chromatographic peak from the spectrum B2 is 7567.7 Da matching the expected mass for $[Ag\text{-}Fe_3S_4]^+$ WT *P.f.* Fd (see Table 4.1).

These results clearly indicate that the major peak from the chromatographic purification belongs to the novel $[Ag\text{-}Fe_3S_4]$ WT *P. f.* Fd. The yield of $[Ag\text{-}Fe_3S_4]$ WT *P. f.* Fd after purification and concentration was 1.65 mg (33 %) from 5 mg of $[Fe_3S_4]$ WT *P.f.* Fd.

8.2.2.2 $[Ag\text{-}Fe_3S_4]$ D14C *P.f.* Fd

Figure 8.4 shows the chromatogram for the purification of $[Ag\text{-}Fe_3S_4]$ D14C *P. f.* Fd on a 16/10 Source 30Q.

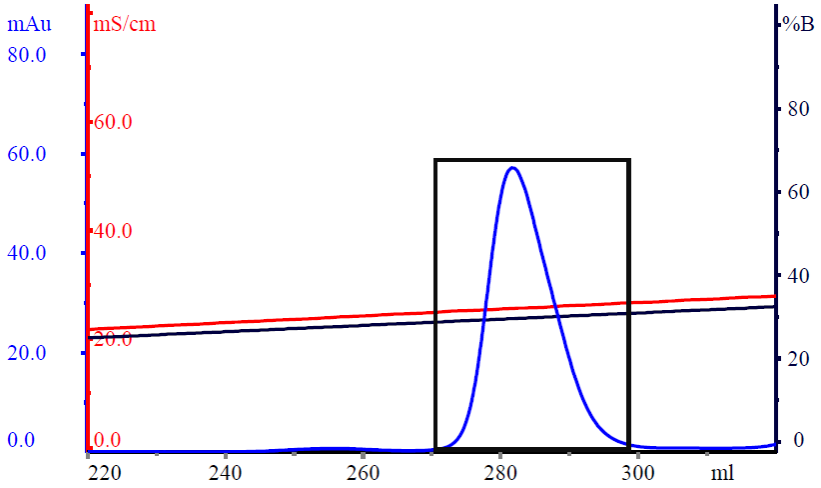

Figure 8.4: Chromatogram for the purification of $[Ag\text{-}Fe_3S_4]$ D14C *P.f.* Fd on a 16/10 Source 30Q column. X-axis: elution volume; blue line: absorption at 280 nm; red line: conductivity; black line: NaCl concentration given as percent of 1 M NaCl.

Only one peak is observed from the chromatogram eluting at 25.5 mS/cm compared to ~ 20.3 mS/cm for $[Fe_3S_4]$ D14C *P.f.* Fd. The volume of the fractions corresponding to the peak was reduced, and the UV-vis spectrum was recorded (see Figure 8.5). The UV-vis spectrum appeared bleached compared to $[Fe_3S_4]$ D14C *P.f.* Fd (see Figure 5.10).

Figure 8.6 shows the negative ion-mode mass spectra of the protein sample from the chromatographic peak. The *m/z*-spectrum A1 shows only one species present with five different charge states, where the peaks for the high charge states (8-, 7- and 6-) are adducts-free compared to the lower charge states where salt adducts are present. The

apparent mass from the mass spectrum A2 is 7555.9 Da matching the expected mass for the novel $[Ag\text{-}Fe_3S_4]^+$ D14C *P.f.* Fd (see Table 4.1).

The yield of $[Ag\text{-}Fe_3S_4]$ D14C *P. f.* Fd after purification and concentration was very much similar to the one for $[Ag\text{-}Fe_3S_4]$ WT *P. f.* Fd – 1.7 mg (34 %) from 5 mg of $[Fe_3S_4]$ D14C *P.f.* Fd.

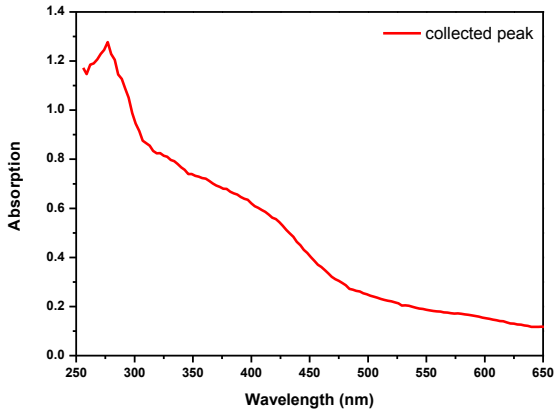

Figure 8.5: UV-vis spectrum of the protein sample from the chromatographic peak in Figure 8.4.

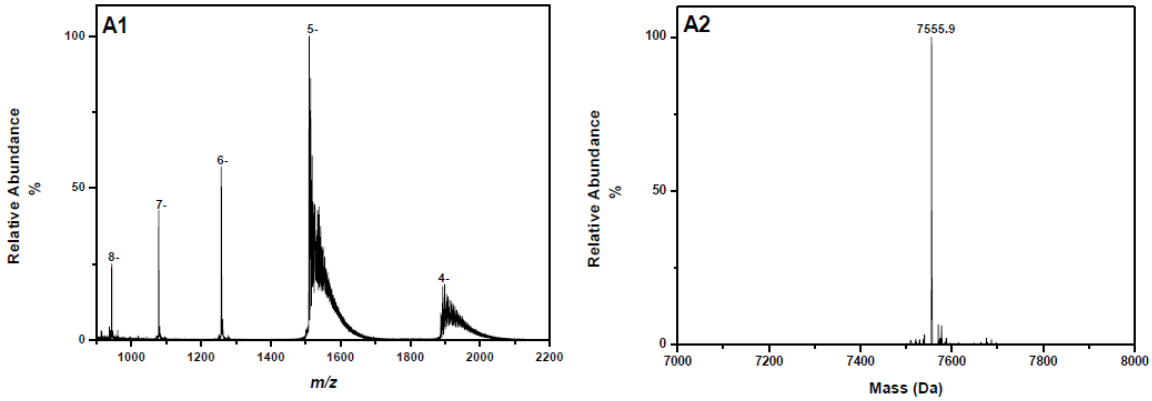

Figure 8.6: Mass spectrometric analysis spectra of the protein sample from the peak from chromatogram shown in Figure 8.4. (A1) *m/z*- and (A2) mass spectra.

8.3 Stability Studies of Ferredoxins Containing $[Ag\text{-}Fe_3S_4]$ Cluster

Synthesized and purified ferredoxins containing $[Ag\text{-}Fe_3S_4]$ cluster were tested towards different storage time, and towards oxygen exposure.

8.3.1 Experimental

Purified samples of $[Ag\text{-}Fe_3S_4]$ cluster containing ferredoxins were concentrated and stored in 20 mM Tris/HCl pH 8.0 and hereafter kept at room temperature inside the glove box. Hereafter, the stability towards different storage times of ferredoxins containing $[Ag\text{-}Fe_3S_4]$ cluster was tested using mass spectrometry. The samples were exposed to the same storage times as for $[Zn\text{-}Fe_3S_4]$ cluster containing ferredoxins (see section 7.3.1).

Standard procedure was used to prepare the samples for mass spectrometric characterization (see section 4.3.1). Mass spectra were recorded for the following storage times and conditions:

A) on the day of the synthesis,
B) one week after the synthesis,
C) one month after the synthesis, and
D) 15 min of sample being exposed to oxygen
E) 3 days of sample being exposed to oxygen.

8.3.2 Results and Discussion

Figure 8.7 shows the negative ion-mode spectra for both [Ag-Fe_3S_4] WT and [Ag-Fe_3S_4] D14C *P.f.* Fd after one month, after exposure to oxygen for 15 min, and after exposure to oxygen for 3 days.

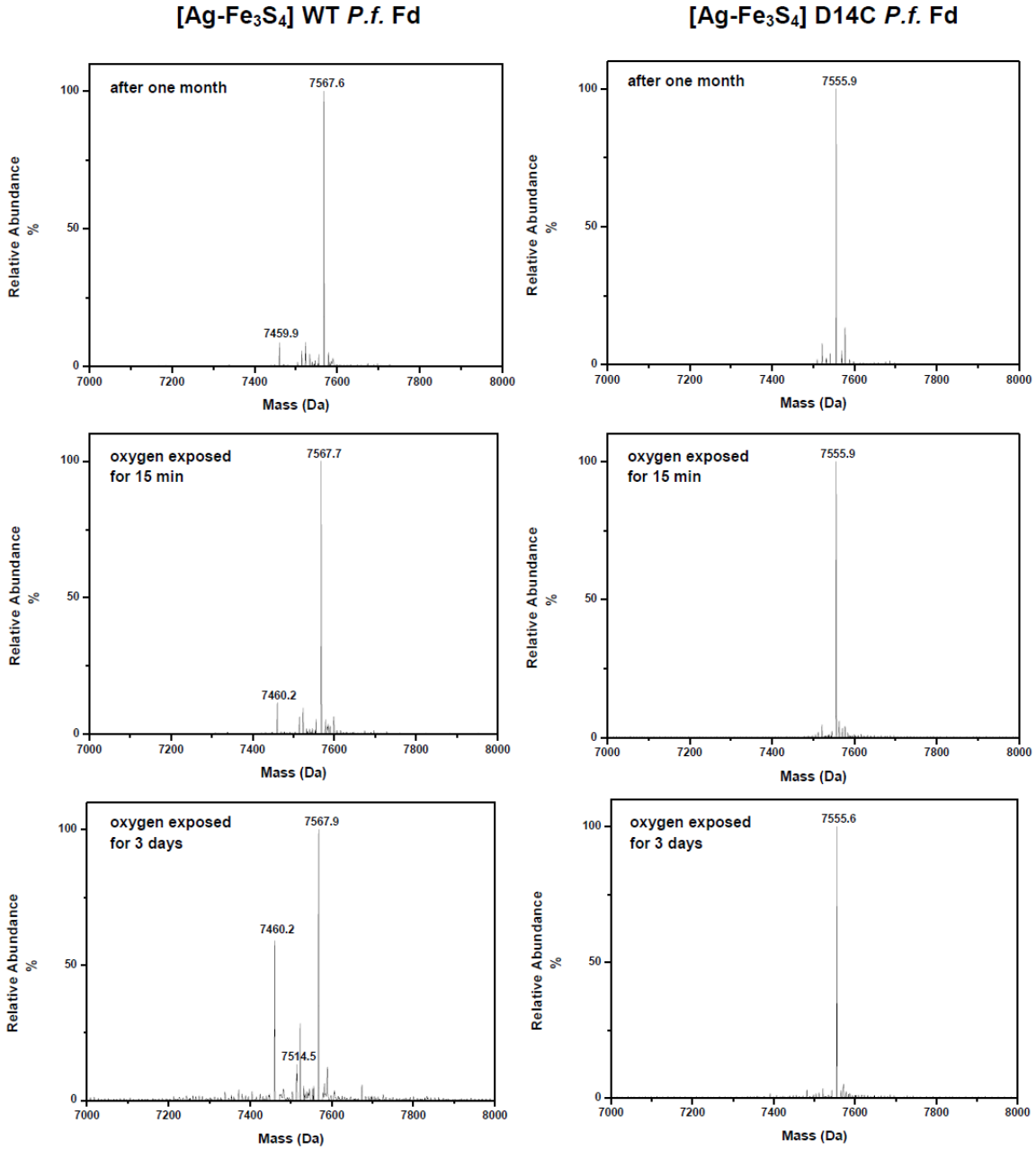

Figure 8.7: Mass spectra for the protein samples after a month, after oxygen exposure for 15 min and for 3 days. Left vertical lane is for [Ag-Fe_3S_4] WT, and the right one is for [Ag-Fe_3S_4] D14C *P.f.* Fd samples.

Freshly purified samples of [Ag-Fe_3S_4] WT *P.f.* Fd and [Ag-Fe_3S_4] D14C *P.f.* Fd, as already seen in the section 8.2.2.1 and 8.2.2.2, contain [Ag-Fe_3S_4]$^+$ cluster as the only species. The samples remained unchanged after a week inside the glove box (data not shown). After a month, some [Fe_3S_4] WT *P.f.* Fd has appeared in the [Ag-Fe_3S_4] WT *P.f.* Fd sample indicating that some of the [Ag-Fe_3S_4] cluster is being converted to [Fe_3S_4]. However, [Ag-Fe_3S_4] D14C *P.f.* Fd remained unchanged. Both protein samples were exposed to oxygen for 15 min, and hereafter the mass spectra were recorded. Data showed that the cluster remains intact both in the WT and the D14C variant. The mass spectra recorded after 2 hours showed no change in both protein samples as well (data not shown). The protein samples were left under aerobic conditions for 3 days. Spectrum E to the left in Figure 8.8 shows that ~ 33% of the [Ag-Fe_3S_4] cluster in WT *P.f.* Fd is being degraded to the [Fe_3S_4] cluster. Also, a certain amount of the [Fe_4S_4] cluster is being formed. However, the [Ag-Fe_3S_4] cluster in D14C *P.f.* Fd remained intact.

The mass spectrometric data suggest that the [Ag-Fe_3S_4] cluster in the variant D14C is more inert towards oxygen exposure compared to the one in WT *P.f*. Fd. The same was observed for the [Zn-Fe_3S_4] cluster in these two Fds (section 7.3.2), implying that the increased stability of the heterometallic cluster in D14C variant is a consequence of replacing the aspartate ligation by cysteine.

8.4 Electrochemical Studies of Ferredoxins Containing [Ag-Fe_3S_4] Cluster

The results from electrochemical characterization of the [Ag-Fe_3S_4] cluster from the WT *P.f.* Fd and its D14C variant are separated into two sections in order to have a better overview. The setup used for electrochemical characterization is described in section 6.3.1.1. All experiments were conducted in 20 mM Tris/HCl pH 8.0 buffer at 25 ± 2 °C with neomycin used as a promoter (40; 88; 89). Mass spectrometric analysis was performed upon electrochemical characterization.

8.4.1 Experimental

Concentrated protein samples (see section 8.2) in 20 mM Tris/HCl pH 8.0 were left over night inside the glove box, and prior to experiment the samples were diluted using the same buffer to the final protein concentration of 40 µM. Neomycin sulfate powder was added to the solution without further purification by dissolving it in a small volume of the protein solution and transferring this to the cell. The final concentration of neomycin in the protein solution was 5 mM. The voltammograms were recorded over the region from 244 mV to -756 mV vs. SHE for various scan rates. The electrodes were adequately prepared for the experiment (see section 6.3.1.1) and transferred to the glove box. Upon electrochemical characterization the protein sample was analyzed by mass spectrometry using the procedure described in section 4.3.1.

8.4.2 Results and Discussion

8.4.2.1 [Ag-Fe_3S_4] WT *P.f.* Fd

Figure 8.8 shows the cyclic voltammogram for 40 µM [Ag-Fe_3S_4] WT *P.f.* Fd in 20 mM Tris/HCl pH 8.0 with 5 mM neomycin at 2 mV/s scan rate. There was no signal obtained neither in the absence nor in the presence of promoter. The sample was scanned over various scan rates from 2 to 100 mV/s, and the signal remained unchanged. Though, a

very small and broad signal (see Figure 8.8) is visible upon neomycin addition which is probably due to the small amounts of [Fe_3S_4] WT *P.f.* Fd present in the protein solution which was also visible from the mass spectrum recorded after the electrochemical characterization (see Figure 8.9).

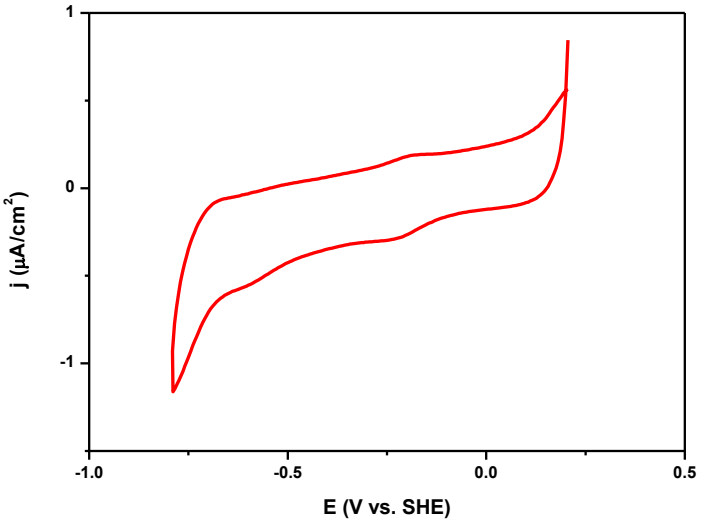

Figure 8.8: Cyclic voltammograms for 40 µM [Ag-Fe_3S_4] WT *P.f.* Fd in 20 mM Tris/HCl pH 8.0 with 5 mM neomycin; scan rate 2 mV/s.

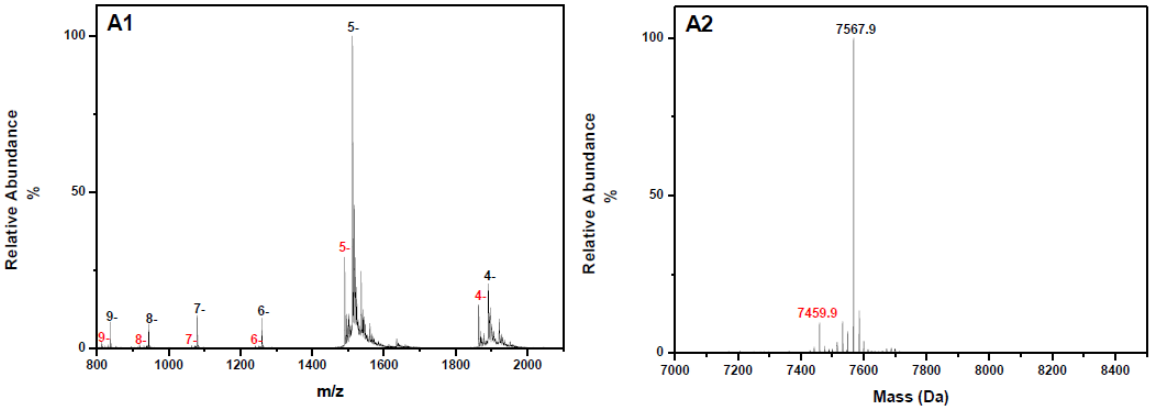

Figure 8.9: Mass spectrometric analysis spectra of [Ag-Fe_3S_4] WT *P.f.* Fd sample after electrochemistry experiment was performed. (A1) *m/z*- and (A2) mass spectra.

Two species are present in a protein sample as observed from the mass spectrum in Figure 8.9 - [Ag-Fe_3S_4]$^+$ WT *P.f.* Fd as the major species with apparent mass 7567.9 Da, and a very small amount of [Fe_3S_4]$^+$ WT *P.f.* Fd with apparent mass 7459.9 Da. For all previously electrochemically characterized ferredoxins the formation of the protein-promoter complex was observed which accords with proposed neomycin promoting effect (88).

Based on the mass spectrometric data for this protein sample no neomycin binding occurs. Binding of neomycin was observed for all other electrochemically characterized Fds from this project, therefore the lack of redox signal for this Fd could be associated with the absence of neomycin binding. This, however, could further imply that incorporation of Ag^+ into the [Fe_3S_4] cluster causes some structural changes in the protein preventing the formation of protein-promoter complex. To detect these structural changes, a high resolution X-ray structure of [Ag-Fe_3S_4] WT *P.f.* Fd is required. Another

reson for the lack of the redox signal could be that the formal potential of the [Ag-Fe_3S_4] WT *P.f.* Fd lies outside the potential range used in the experiment. However, the absence of redox signal suggests that Ag^+ was incorporated in the [Fe_3S_4] cluster.

8.4.2.2 [Ag-Fe_3S_4] D14C *P.f.* Fd

The cyclic voltammogram for 40 µM [Ag-Fe_3S_4] D14C *P.f.* Fd in 20 mM Tris/HCl pH 8.0 with 5 mM neomycin at 2 mV/s scan rate is shown in Figure 8.10. The lack of redox signal was observed for this protein sample as well, both in the presence and absence of neomycin. On the positive side of the cyclic voltammogram, however, arising of the signal is observed and the formation of the redox couple is suspected, implying that the redox couple formation might occure at higher potential values. The mass spectrum recorded upon the electrochemical characterization of the protein is shown in Figure 8.11.

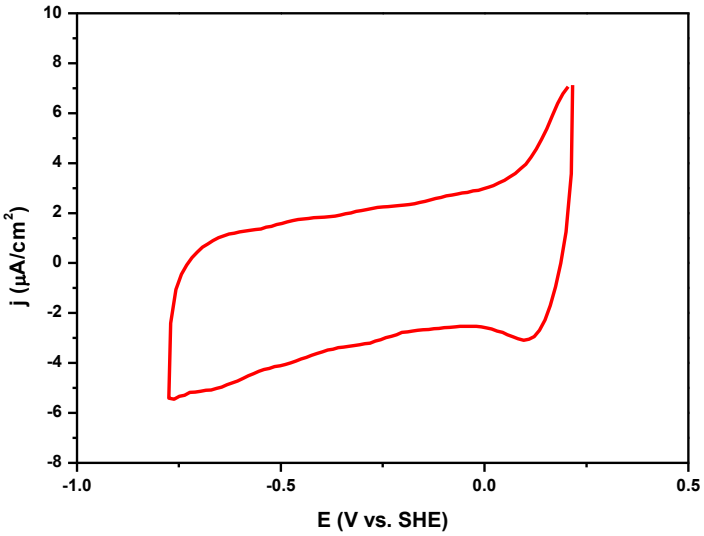

Figure 8.10: Cyclic voltammogram of 40 µM [Ag-Fe_3S_4] D14C *P.f.* Fd in 20 mM Tris/HCl pH 8.0 with 5 mM neomycin; scan rate 30 mV/s.

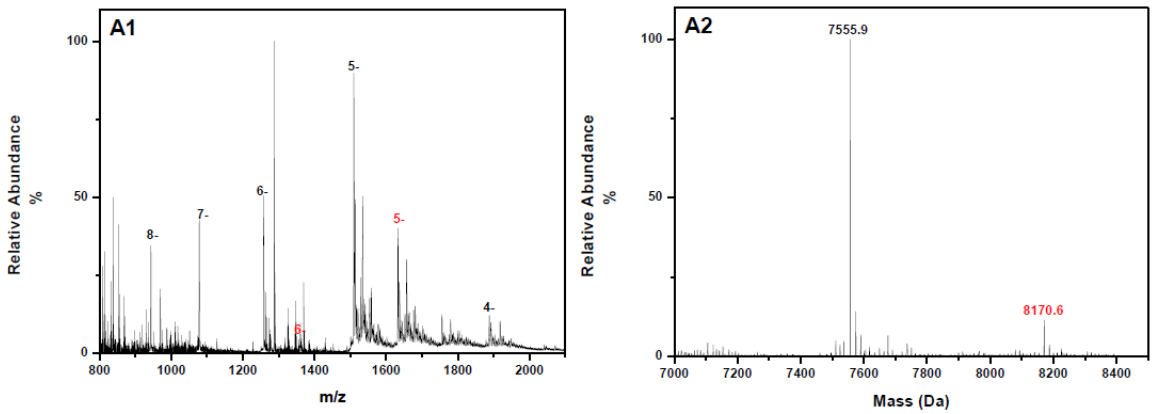

Figure 8.11: Mass spectrometric analysis spectra of [Ag-Fe_3S_4] D14C *P.f.* Fd sample after electrochemistry experiment was performed. (A1) *m/z*- and (A2) mass spectra.

The *m/z*-range used for calculating the mass spectrum was from 1200 to 2000. The observed apparent masses belong to [Ag-Fe_3S_4]$^+$ D14C *P.f.* Fd as the major peak with 7555.9 Da, while the second peak belongs to the protein-promoter complex with apparent mass app. ~ 615 Da higher.

Based on the mass spectrometric data the formation of the protein-promoter complex is observed for [Ag-Fe_3S_4] D14C *P.f.* Fd. However, the redox signal was not observed for the used potential range. This accords with the results obtained for the [Ag-Fe_3S_4] WT *P.f.* Fd from section 8.4.2.2. If an intrinsic factor i.e. electron-withdrawing power of the heterometal was the only determining factor of the formal potential then the same trend which was observed for the synthetic, non-protein analogues would be observed for all proteins. Holm *et al.* have measured the formal potential for a number of non-protein analogues of heterometallic [M-Fe_3S_4] clusters; the observed order is Fe < Co< Ni < Cu <Ag (97). However, the intrinsic property of the heterometal is not the only factor influencing the formal potential of the cluster in the protein environment and the same trend as for the synthetic analogues is not observed (97; 89) but it serves as a good guide. Therefore, running the electrochemistry experiment with extented potential range toward more positive potential would offer some more information.

However, as opposed to [Ag-Fe_3S_4] WT *P.f.* Fd, the formation of the protein-promoter complex is observed for the [Ag-Fe_3S_4] D14C *P.f.* Fd. The reasons for this remain unclear.

8.5 EPR Spectroscopic Studies of Ferredoxins Containing [Ag-Fe_3S_4] Cluster

The [Ag-Fe_3S_4] cluster has not ben characterized before using EPR spectroscopy. As previously mentioned in section 3.5, the ground spin state of heterometallic cuboidal clusters [MFe_3S_4] can be rationalized by anti-ferromagnetic coupling between the high-spin metal ion, M, and the appropriate cluster fragment, i.e. $[Fe_3S_4]^+$ (S = 1/2), $[Fe_3S_4]^0$ (S = 2) or $[Fe_3S_4]^-$ (S = 5/2) (49). Based on this model Ag^+ ions couples anti-ferromagnetically to the $[Fe_3S_4]^{+/0}$ fragment, and the expected ground spin state of the oxidized [Ag-Fe_3S_4]$^{2+}$ cluster is S = 1/2, and for the reduced [Ag-Fe_3S_4]$^+$ cluster is S = 2.

The same experimental setup described in section 7.5 was used for EPR spectroscopic characterization of the [Ag-Fe_3S_4] Fds.

8.5.1 Experimental

The samples of [Ag-Fe_3S_4] WT and [Ag-Fe_3S_4] D14C *P.f.* Fd were synthesized using the procedure described in section 8.2 and 8.3 and hereby prepared for EPR spectroscopic measurements. Both protein samples were buffer exchanged to 20 mM Tris/HCl pH 8.0, concentrated using a Vivacell 70 (Sartorius Stedum Biotech) with a 5000 MWCO membrane, and prepared, inside the glove box, for EPR measurements. Two sets of each protein sample were prepared – one “as-purified” protein sample, and one dithionite reduced sample (reduced with 10 mM dithionite from a freshly prepared solution of 1M $Na_2S_2O_4$ in 1M Tris/HCl pH 8.0). 200 µL of each sample was transferred into rubber-sealed quartz tubes, taken out of the glove box, and frozen in liquid nitrogen. Hereafter, the rubber lid was removed, frozen samples placed into the dry shipper (liquid nitrogen temperature, -196 °C), and shipped to TU Delft.

As mentioned in section 7.5, the samples were unintentionally thawed and therefore oxygen exposed prior their arrival. The samples were frozen in liquid nitrogen again, and EPR spectra were recorded. These samples will be referred to as “oxygen exposed”

samples. Afterwards, two new sets of samples were prepared using these thawed samples – originally "as-purified" sample was re-oxidized and the reduced sample was re-reduced. EPR spectroscopic characterization was performed hereafter.

Thawed protein samples were transferred to the glove box and the following samples were prepared:

1) The "re-oxidized" sample – the "as-purified" sample was oxidized using a solution of 100 mM $K_3[Fe(CN)_6]$ in 1M Tris/HCl pH 8.0 to the final concentration of 1 mM $K_3[Fe(CN)_6]$,
2) The "re-reduced" sample – the reduced sample was re-reduced with dithionite from a freshly prepared solution of 1M $Na_2S_2O_4$ in 1M Tris/HCl pH 8.0 to the final concentration of 10 mM $Na_2S_2O_4$.

Samples were incubated inside the glove box for 15 minutes, rubber-sealed, taken out of the glove box, and frozen in liquid nitrogen again. Hereafter, the EPR spectra were recorded. Frozen protein samples were shipped back to our labs and the mass spectrometric analysis was performed using the procedure for sample preparation given in section 4.3.1.

8.5.2 Results and Discussion

8.5.2.1 [Ag-Fe_3S_4] WT *P.f.* Fd

The X-band EPR spectra in a perpendicular mode of the oxygen exposed and the re-oxidized [Ag-Fe_3S_4] WT *P.f.* Fd sample are shown in Figure 8.12. A signal at around 3400 Gauss (g ~ 2.02) is observed for both spectra. The g-value and the shape of the resonance signal are very typical for the $[Fe_3S_4]^+$ cluster which is paramagnetic with S = 1/2 system (30). This might suggest that the [Ag-Fe_3S_4] cluster was degraded by the loss of Ag ion due to its prolonged oxygen exposure which was previously observed from the stability studies of [Ag-Fe_3S_4] WT *P.f.* Fd (see section 8.3). However, for the re-oxidized sample changes in the shape of the signal are observed (Figure 8.12 B) implying that upon the oxidation there is another paramagnetic species present in the sample besides $[Fe_3S_4]^+$Fd.

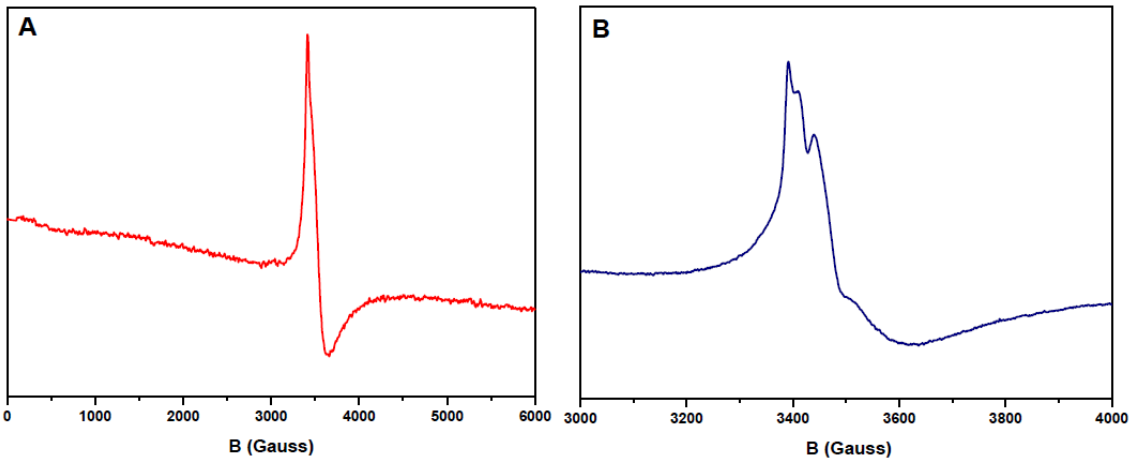

Figure 8.12: X-band EPR spectra in perpendicular mode of 150 µM [Ag-Fe_3S_4] WT *P.f.* Fd in 20 mM Tris/HCl pH 8.0. (A) oxygen exposed sample, wide field range, T = 10 K, v = 9.65 GHz, P = 2 dB, G = $1 \cdot 10^4$; (B) re-oxidized sample with 1 mM $K_3[Fe(CN)_6]$, narrower field range, T = 10 K, v = 9.65 GHz, P = 2 dB, G = $1 \cdot 10^4$.

Figure 8.13 shows the X-band EPR spectra in perpendicular mode of the oxygen exposed and the re-reduced [Ag-Fe_3S_4] WT *P.f.* Fd samples. For both spectra a signal at around 3400 Gauss (g ~ 2.02) is observed. The g-value and the shape of the resonance signal are very typical for the $[Fe_3S_4]^+$ cluster for both samples (see section 3.4.1, Figure 3.6) (30). No changes in the shape of the signal are observed by re-reducing the sample meaning that no other paramagnetic species is being formed in the sample by reducing it.

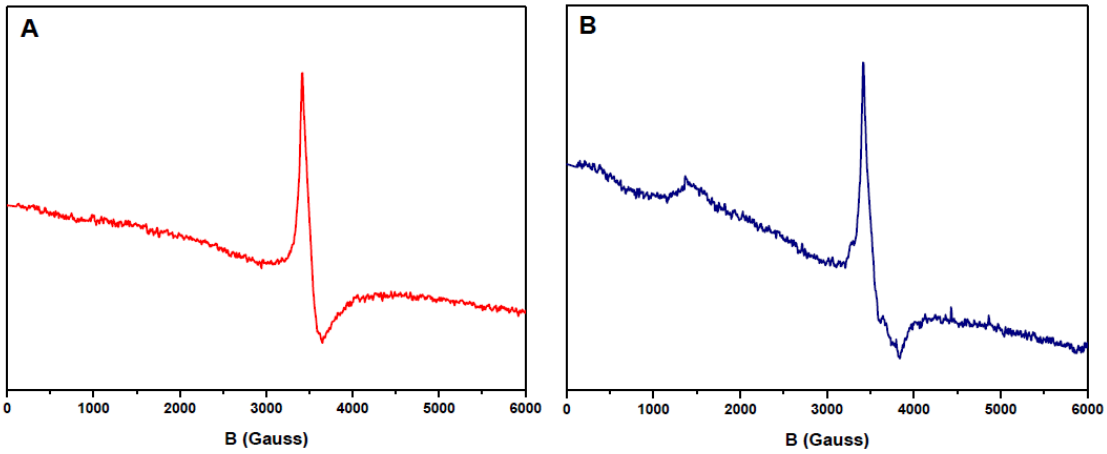

Figure 8.13: X-band EPR spectra in perpendicular mode of 150 µM [Ag-Fe_3S_4] WT *P.f.* Fd in 20 mM Tris/HCl pH 8.0. (A) oxygen exposed sample, T = 9.2 K, v = 9.65 GHz, P = 2 dB, G = $1 \cdot 10^4$; (B) re-reduced sample with 10 mM $Na_2S_2O_4$, T = 9.2 K, v = 9.65 GHz, P = 2 dB, G = $1 \cdot 10^5$.

Afterwards the X-band EPR spectra in parallel mode was recorded for the re-reduced sample (see Figure 8.14). The spectrum shows a broad peak at around 500-600 Gauss (g ~ 12) typical for diamagnetic species with the integer spin S = 2.

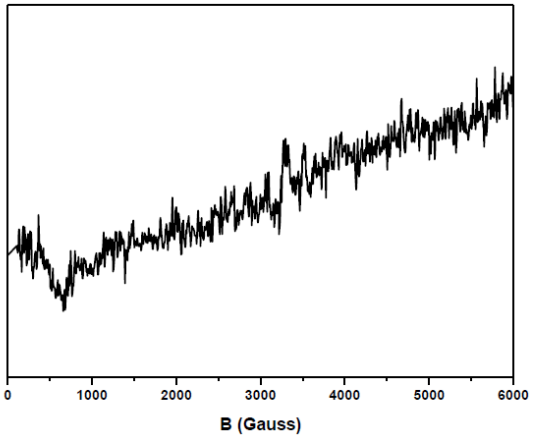

Figure 8.14: X-band EPR spectra in parallel mode of 150 µM [Ag-Fe_3S_4] WT *P.f.* Fd in 20 mM Tris/HCl pH 8.0 re-reduced with 10 mM $Na_2S_2O_4$, T = 9.2, v = 9.37 GHz, P = 2 dB, G = $1 \cdot 10^5$.

The mass spectra of the re-oxidized and re-reduced protein sample recorded after the EPR measurements are shown in Figure 8.15 and 8.16, respectively. The *m/z*-range from 900 to 1300 was used for calculating the mass spectrum A2. There are three species present in the sample which is visible from the zoomed *m/z*-spectrum (spectrum (I), Figure 8.15).

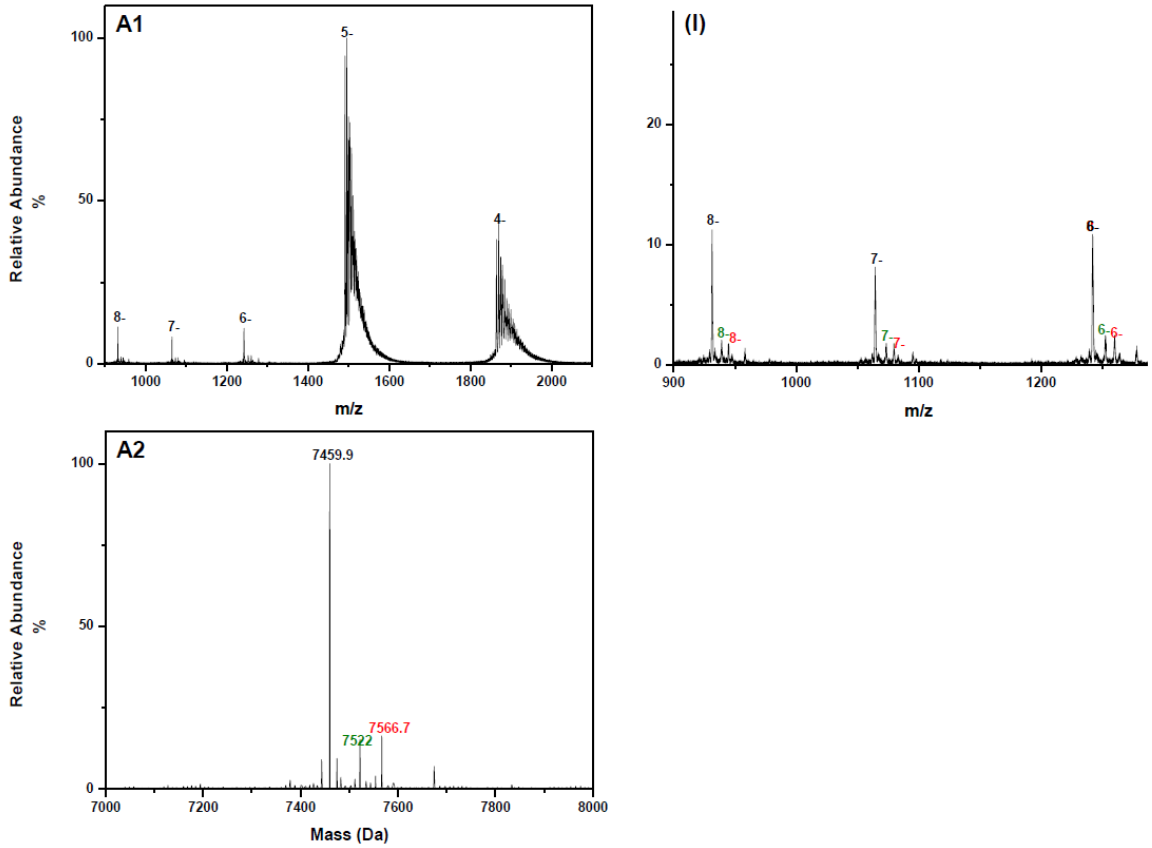

Figure 8.15: Mass spectrometric analysis spectra of the re-oxidized [Ag-Fe_3S_4] WT *P.f.* Fd sample after EPR measurements. (A1) *m/z*- and (A2) mass spectrum. (I) zoomed spectrum A1 in the *m/z*-range 900 to 1300.

The major species with the apparent mass 7459.9 Da is $[Fe_3S_4]^+$ WT *P.f.* Fd. The species with the apparent mass 7566.7 Da is [Ag-$Fe_3S_4]^{2+}$ WT *P.f.* Fd (for expected masses see Table 4.1), while the species with the apparent mass 7522 Da is most probably a product of the cluster degradation since it hasn't been observed in the sample before the EPR measurements.

The mass spectra for the re-reduced sample are shown in Figure 8.16. For calculating the mass spectrum the range from 900 to 1300 from its *m/z*-spectrum was used. As it can be seen from the zoomed *m/z*-spectrum in Figure 8.16, the sample contains three species. The apparent mass 7514.8 Da corresponds to the $[Fe_4S_4]^{2+}$ Fd which is diamagnetic and EPR silent with S = 0 (30), and according to the mass spectrum is a major species in this sample. The other two peaks with the apparent masses 7459.6 Da and 7567.3 Da correspond to the expected masses for the $[Fe_3S_4]^+$ Fd and the [Ag-$Fe_3S_4]^+$ Fd, respectively. This is also consistent with the data gained from the stability studies in section 8.3 where degradation of the [Ag-Fe_3S_4] WT *P.f.* Fd to the same three species was observed when the protein sample was exposed to oxygen for a longer period of time. This also suggests that under reducing conditions a certain amount of the [Ag-Fe_3S_4] cluster in the WT *P.f.* Fd is being rebuilt. However, the formation of [Fe_4S_4] Fd seems to be the favored process under reducing conditions. The same behavior is observed for [Zn-Fe_3S_4] WT *P.f.* Fd in section 7.5.2.1.

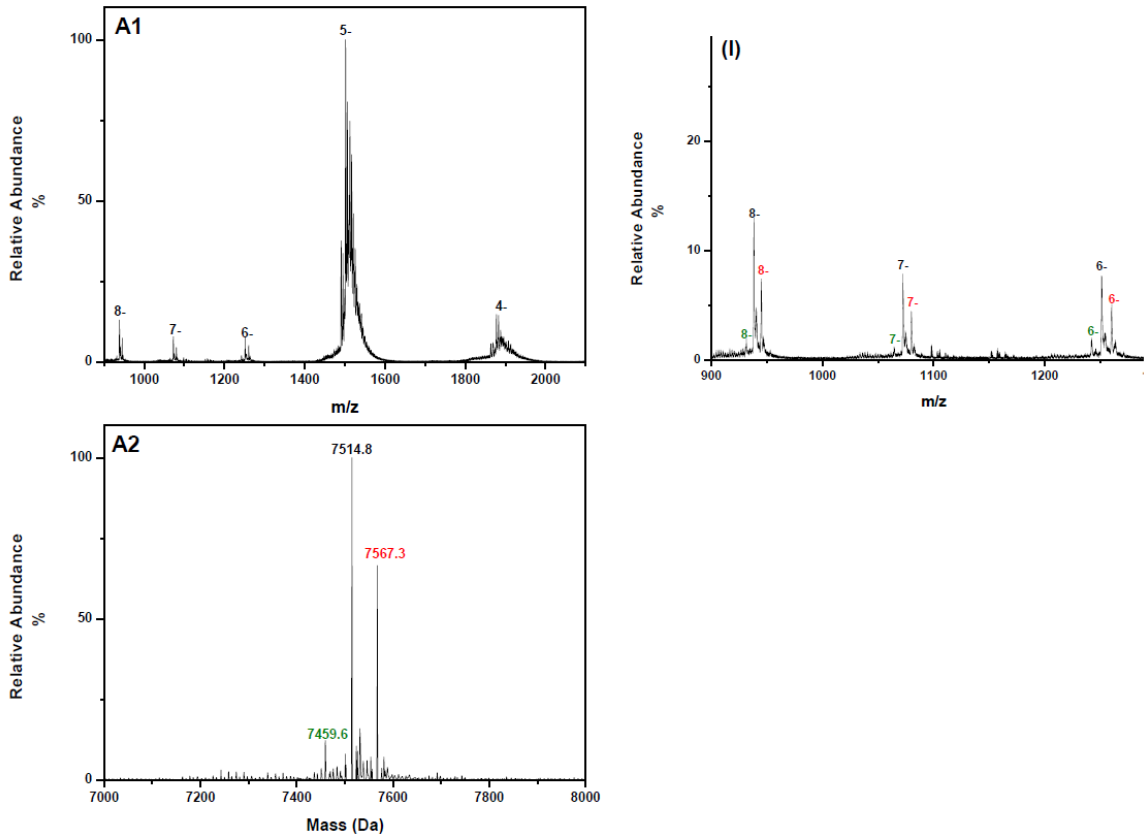

Figure 8.16: Mass spectrometric analysis spectra of the re-reduced [Ag-Fe_3S_4] WT *P.f.* Fd sample after EPR measurements. (A1) *m/z*- and (A2) mass spectrum. (I) zoomed spectrum A1 in the *m/z*-range 900 to 1300.

Based on the mass spectrometric data the paramagnetic species present in the re-oxidized sample is the $[Fe_3S_4]^+$ Fd. However, $[Ag\text{-}Fe_3S_4]^{2+}$ WT *P.f.* Fd was detected in small amounts (see Figure 8.15). Combining the mass spectrometric and the EPR spectroscopic data suggests that the species influencing the difference in the shape of the EPR signal for $[Fe_3S_4]^+$ cluster with S = 1/2 system in the re-oxidized sample could be the $[Ag\text{-}Fe_3S_4]^{2+}$ WT *P.f.* Fd (see Figure 8.12). Therefore, it can be rationalized that the $[Ag\text{-}Fe_3S_4]^{2+}$ is a paramagnetic species with a ground spin state S = 1/2, as expected. Mass spectrometric analysis also shows that the [Ag-Fe_3S_4] cluster in WT *P.f.* Fd is being degraded by oxidizing it with ferricyanide.

Based on the mass spectrometric data the only paramagnetic species from the re-reduced sample that should give a resonance signal in perpendicular mode is $[Fe_3S_4]^+$ Fd with S = 1/2 which is an agreement with the observed signal (see Figure 8.13). The EPR spectrum in a parallel mode of the re-reduced sample (see Figure 8.14) shows the signal for the species with the integer spin S = 2. The mass spectrometric data shows the presence of a very small amounts of $[Fe_3S_4]^0$ Fd in the sample (less than 10 % compared to the major species) and significant amounts of $[Ag\text{-}Fe_3S_4]^+$ WT *P.f.* Fd (see Figure 8.16) implying that a certain portion of the [Ag-Fe_3S_4] cluster is being rebuilt under reducing conditions. If it is assumed that the $[Ag\text{-}Fe_3S_4]^{2+}$ cluster is a paramagnetic species, its reduction will result in a diamagnetic $[Ag\text{-}Fe_3S_4]^+$ cluster with a ground state S = 2. Therefore, diamagnetic $[Ag\text{-}Fe_3S_4]^+$ cluster might also contribute to the observed signal.

8.5.2.2 [Ag-Fe_3S_4] D14C *P.f.* Fd

The X-band EPR spectra in perpendicular mode of the oxygen exposed and the re-oxidized [Ag-Fe_3S_4] D14C *P.f.* Fd sample are shown in Figure 8.17 A and B.

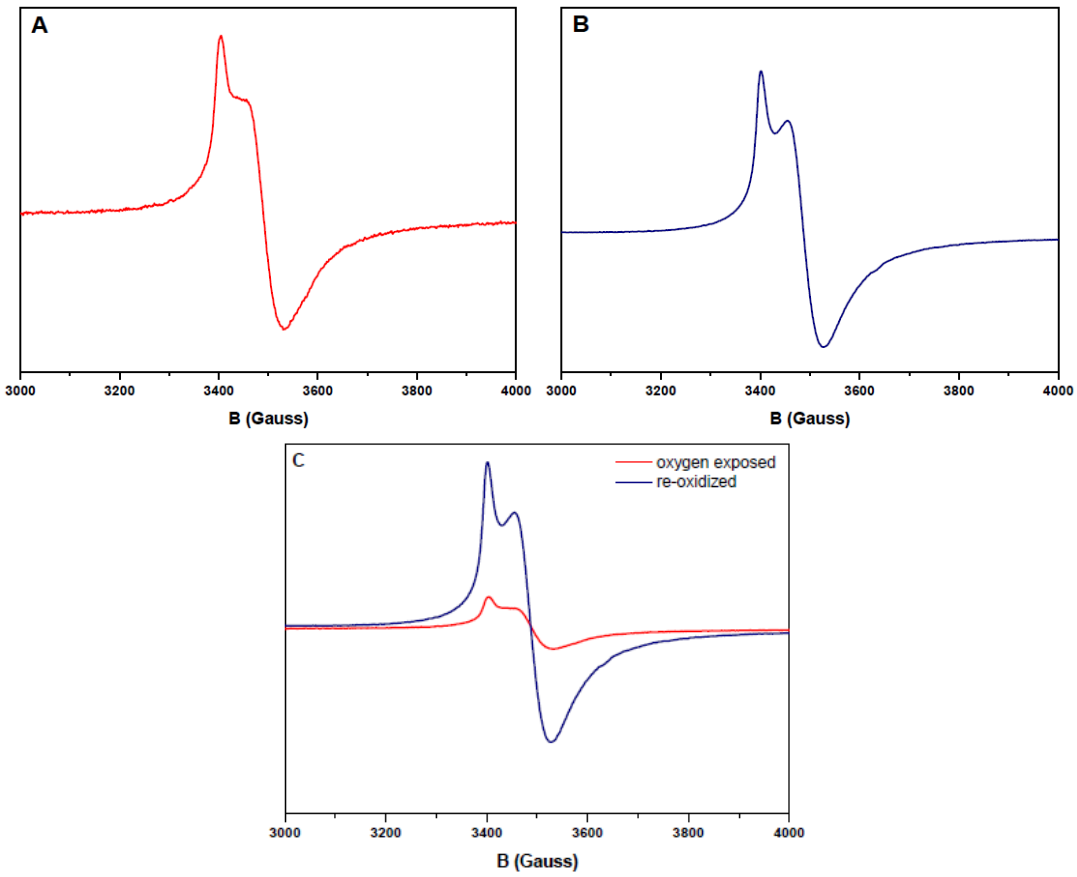

Figure 8.17: X-band EPR spectra in perpendicular mode of 230 µM [Ag-Fe_3S_4] D14C *P.f.* Fd in 20 mM Tris/HCl pH 8.0. (A) oxygen exposed sample, T = 10 K, v = 9.65 GHz, P = 2 dB, G = $5 \cdot 10^4$; (B) re-oxidized sample with 1 mM $K_3[Fe(CN)_6]$, T = 10 K, v = 9.65 GHz, P = 2 dB, G = $1 \cdot 10^4$, (C) comparison of the two EPR spectra on a same scale for the experimental conditions given.

Both spectra show peak at around 3400 Gauss (g ~ 2.02) with the g-value typical for the paramagnetic system with S = 1/2 but with deviation in shape compared to the typical signal for the $[Fe_3S_4]^+$ cluster (see section 3.4.1, Figure 3.6) (30). However, by re-oxidizing the sample, besides the signal at 3400 Gauss, a signal at 3450 Gauss (g ~ 1.99) sharpens up (see Figure 8.17 B). Based on a molar quantification at the conditions given in the figure caption using a copper standard, the concentration of the paramagnetic species in the oxygen exposed sample is found to be ~ 40 µM. Also, if plotted together the EPR spectra of the oxygen exposed and re-oxidized sample on the same scale for a given experimental conditions (see Figure 8.17 C) it can be seen that the intensity of the re-oxidized sample is much, much higher. This implies that a paramagnetic species is being formed or its concentration increases by oxidizing the protein sample which causes the change in the shape of the signal.

Figure 8.18 shows the X-band EPR spectra in perpendicular mode of the oxygen exposed and the re-reduced [Ag-Fe_3S_4] D14C *P.f.* Fd sample (spectra A and B, respectively). For both spectra a signal at around 3400 Gauss (g ~ 2.02) is observed.

The g-value and the shape of the resonance signal are typical for the paramagnetic $[Fe_3S_4]^+$ cluster with S = 1/2 system (see section 3.4.1, Figure 3.6) (30).

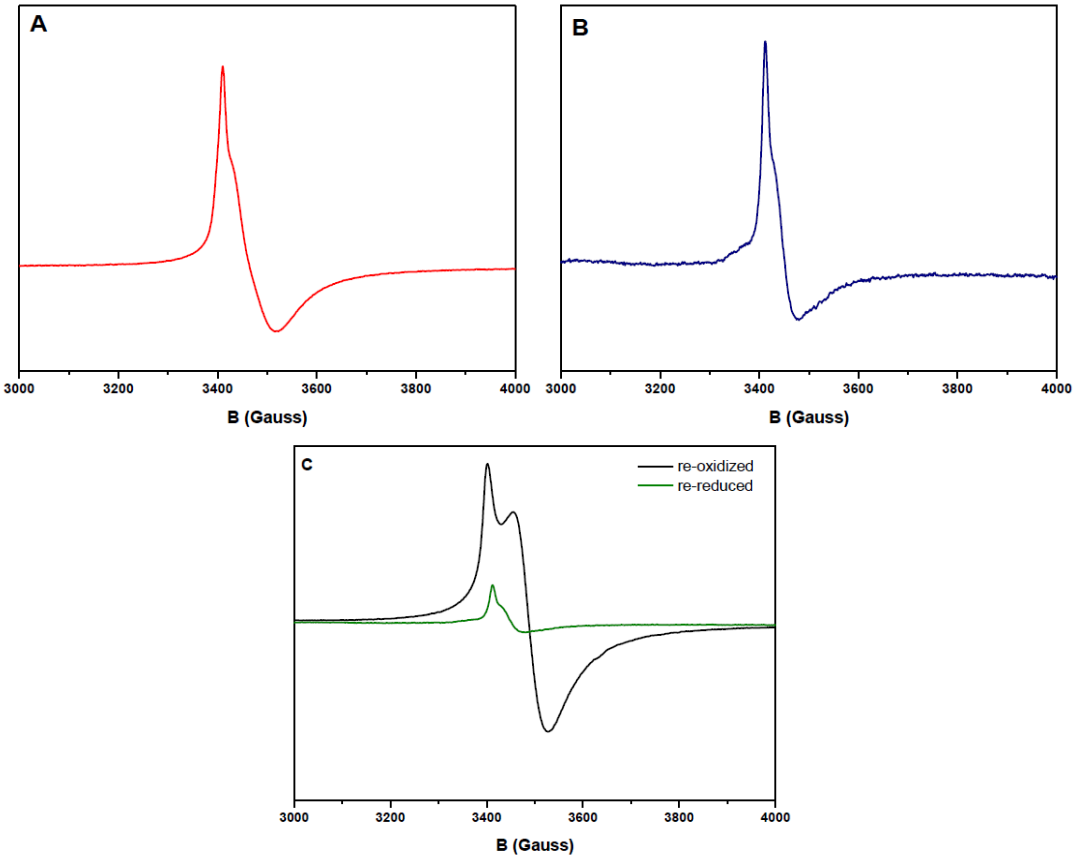

Figure 8.18: X-band EPR spectra in perpendicular mode of 230 µM [Ag-Fe_3S_4] D14C *P.f.* Fd in 20 mM Tris/HCl pH 8.0. (A) oxygen exposed sample, T = 9.2, v = 9.65 GHz, P = 2 dB, G = $1 \cdot 10^4$; (B) re-reduced sample with 10 mM $Na_2S_2O_4$, T = 9.2, v = 9.65 GHz, P = 2 dB, G = $1 \cdot 10^5$; (C) comparison of EPR spectra of re-oxidized (black trace) and re-reduced (green trace) [Ag-Fe_3S_4] D14C *P.f.* Fd on a same scale for the experimental conditions given in this caption and the caption of Figure 8.17.

No changes in the shape of the signal caused by re-reduction are observed. Based on a molar quantification at the conditions given in the figure legend using a copper standard, the concentration of the $[Fe_3S_4]^+$ Fd in the oxygen exposed sample is found to be ~ 110 µM while its concentration in the re-reduced sample is app. 11 times lower (~ 10 µM) which is caused by the cluster reduction and the formation of diamagnetic species $[Fe_3S_4]^0$ with S = 2 ground spin state (30). Also, if plotted together the EPR spectra of re-oxidized and re-reduced sample on the same scale for a given experimental conditions (see Figure 8.18 C) it can be seen that the intensity of the re-reduced sample is much, much lower indicating a trace amounts of the $[Fe_3S_4]^+$ Fd present in the sample.

The X-band EPR spectra in parallel mode was recorded for the re-reduced sample (see Figure 8.19). The spectrum shows a very broad peak at around 560 Gauss (g ~ 12) typical for the diamagnetic species with S = 2 (30).

The mass spectra of the re-oxidized and re-reduced protein sample recorded after the EPR spectroscopic characterization are shown in Figure 8.20 and 8.21, respectively.

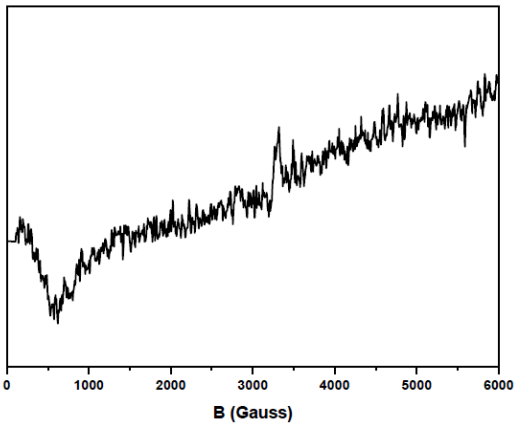

Figure 8.19: X-band EPR spectra in parallel mode of 230 µM [Ag-Fe_3S_4] D14C *P.f.* Fd in 20 mM Tris/HCl pH 8.0 re-reduced with 10 mM $Na_2S_2O_4$, T = 9.2, v = 9.37 GHz, P = 2 dB, G = $1 \cdot 10^5$.

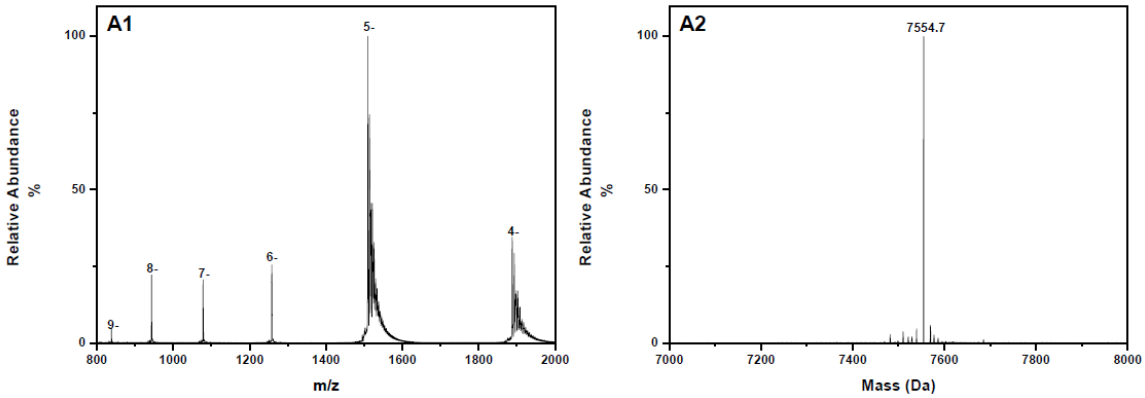

Figure 8.20: Mass spectrometric analysis spectra of the re-oxidized [Ag-Fe_3S_4] D14C *P.f.* Fd sample after EPR measurements. (A1) *m/z*- and (A2) mass spectrum.

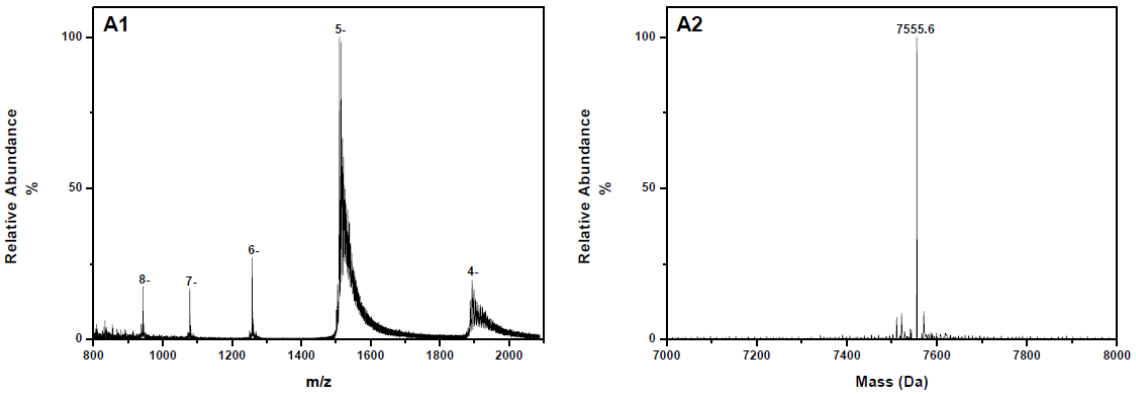

Figure 8.21: Mass spectrometric analysis spectra of the re-reduced [Ag-Fe_3S_4] D14C *P.f.* Fd sample after EPR measurements. (A1) *m/z*- and (A2) mass spectrum.

Based on the mass spectrometric data both samples contain exclusively one species - [Ag-Fe_3S_4] D14C *P.f.* Fd. The difference in their apparent masses is ~ 1 Da which suggests the difference in the oxidation state of the cluster – [Ag-Fe_3S_4]$^{2+}$ and [Ag-Fe_3S_4]$^{+}$ for the re-oxidized and re-reduced sample, respectively, based on the calculations for the expected masses for [Ag-Fe_3S_4] D14C *P.f.* Fd (see Table 4.1). As mentioned, the protein was oxidized with ferricyanide that has a formal potential +410 mV (85) and based on the mass spectrometric data the change in the oxidation state is observed. In the light of the electrochemistry experiment in section 8.2.2 this suggests

that the experiment should be conducted over a range of potential extened to the positive side compared to the experimental setup in section 8.2.2. Thus, it is believed that Ag^+ incorporation into the $[Fe_3S_4]$ cluster renders the formal potential more positive and it lies outside the potential range which was used in the electrochemistry experiment rather then that the incorporation of the Ag^+ into the $[Fe_3S_4]$ cluster causes its inactivation. Also, based on the mass spectrometric data the $[Ag\text{-}Fe_3S_4]$ cluster in D14C variant has remained intact under both oxidizing and reducing conditions. Compared to the data obtained for the $[Ag\text{-}Fe_3S_4]$ WT *P.f.* Fd where cluster breaks down upon oxidation with ferricyanide, the $[Ag\text{-}Fe_3S_4]$ cluster in D14C variant is much more inert. This observation also accords with those from the stability studies in section 7.3.2.

The mass spectrometric analysis implies that the EPR signal in Figure 8.17 for the re-oxidized sample comes from the species containing the $[Ag\text{-}Fe_3S_4]^{2+}$ cluster. This suggests that this species is, as expected, paramagnetic and with S = 1/2 ground spin state. The EPR signal for the re-reduced sample combined with the mass spectrometric data (see Figure 8.18 and 8.21) suggest that the signal comes from the traces of $[Fe_3S_4]^+$ Fd present in the protein sample (also see Figure 8.18 C). The EPR spectrum of the re-reduced sample in parallel mode (see Figure 8.19) shows the signal for the diamagnetic species with S = 2. The mass spectrometric data combined with the EPR measurements for the re-reduced sample imply that the diamagnetic species with the signal in parallel EPR mode is the reduced $[Ag\text{-}Fe_3S_4]^+$ D14C *P.f.* Fd with a ground spin state S = 2, as expected. However, further investigations of the $[Ag\text{-}Fe_3S_4]$ cluster are required. Mössbauer spectroscopic measurements would provide some further insight into its magnetic and electronic properties.

8.6 Conclusions

Both the WT *P.f.* Fd and its variant D14C containing $[Ag\text{-}Fe_3S_4]$ cluster were successfully synthesized, and chromatographically purified. The novel ferredoxins were subsequently characterized using multidisciplinary approach involving mass spectrometric analysis, electrochemistry and EPR spectroscopy.

Mass spectrometric analysis of the purified samples showed that the proteins are synthesized in a form containing the reduced cluster $[Ag\text{-}Fe_3S_4]^+$. Stability studies of these novel ferredoxins have shown that they are, especially the $[Ag\text{-}Fe_3S_4]$ D14C *P.f.* Fd, much more inert towards oxygen exposure than other ferredoxins containing heterometallic cluster. Attempts were made to characterize both Fds electrochemically using a bulk solution cyclic voltammetry. However, no redox signal was obtained for the used experimental setup. Further studies imply that the experiment should be conducted over a broader range of potential. The EPR spectroscopic studies combined with mass spectrometric analysis have confirmed the presence of the $[Ag\text{-}Fe_3S_4]$ cluster in both WT and D14C *P.f.* Fd. Based on these studies it is believed that the oxidized $[Ag\text{-}Fe_3S_4]^{2+}$ cluster has a ground spin state S = 1/2 versus S = 2 in its reduced form.

For the first time the $[Ag\text{-}Fe_3S_4]$ cluster was synthesized inside the ferredoxin. Using a multidisciplinary approach, the WT *P.f.* Fd and its D14C variant containing the $[Ag\text{-}Fe_3S_4]$ cluster were synthesized, chromatographically purified and characterized using UV-vis spectrophotometry, intact metalloprotein mass spectrometric analysis, cyclic voltammetry and EPR spectroscopy.

9 Overall Conclusion and Perspectives

The main goal of this thesis was synthesis, purification and characterization involving mass spectrometric analysis, electrochemistry and EPR spectroscopy of artificial ferredoxins containing heterometallic clusters. For that purpose, two ferredoxins were used as reference systems – WT *P.f.* Fd and its variant D14C. Artificial ferredoxins containing heterometallic cluster were synthesized and subsequently characterized by incorporating non-naturally occurring metal-ions into their active centers. Two metal-ions were used for this purpose and two sets of artificial ferredoxins were synthesized – the first set containing the [Zn-Fe_3S_4] cluster, and the second containing the [Ag-Fe_3S_4] cluster.

This is the first multidisciplinary study on artificial ferredoxins containing the [Zn-Fe_3S_4] cluster. They were synthesized and for the first time purified by established chromatographic procedure. High purity of the species was confirmed by mass spectrometric analysis. Electrochemical characterization of the [Zn-Fe_3S_4] cluster in WT *P.f.* Fd and its D14C variant resulted in determined formal potentials of -206 mV and -254 mV vs. SHE, respectively. EPR spectroscopic studies confirmed the presence of the [Zn-Fe_3S_4] cluster in these artificial ferredoxins. The [Zn-Fe_3S_4] cluster in WT *P.f.* Fd and in its D14C mutant is now very well characterized using various techniques in this multidisciplinary study. The next step would be to start investigating the possibilities of this artificial ferredoxin to catalyze some interesting chemical reactions.

The synthesis of the [Ag-Fe_3S_4] cluster in a protein environment was reported for the first time, and the same multidisciplinary approach as for the Fds containing the [Zn-Fe_3S_4] cluster was applied on its characterization. The purification procedure resulted in protein sample containing exclusively the [Ag-Fe_3S_4] ferredoxin which was subsequently confirmed by mass spectrometric analysis followed by EPR spectroscopic characterization. Combined EPR and mass spectrometric studies suggest that in its oxidized form the [Ag-Fe_3S_4] cluster has a ground spin state S = 1/2, and S = 2 in its reduced form. Attempts were made to characterize these two novel ferredoxins electrochemically however further investigations in that direction are required. The characterization of the [Ag-Fe_3S_4] Fds is still in its initial phase. However, it would be interesting to examine the potential of this cluster to bind exogenous ligands and their effect on EPR spectra. Also, investigation of the catalytic properties of this novel ferredoxin would be very intriguing. No structures are available on ferredoxins containing heterometallic cluster. The information gained from the heterometallic cluster structure would be beneficial for correct assessment of possible catalytic function. Therefore, employing crystallographic studies to determine their three dimensional structure would be of great importance. The [Ag-Fe_3S_4] D14C *P.f.* Fd is a very good candidate for those since, as compared to other artificial ferredoxins, it is more stable in aerobic conditions which makes the experimental setup for crystallographic studies much easier.

A general trend was observed concerning the stabilities of these artificial ferredoxins. All heterometallic clusters from the variant D14C are observed to be more inert towards oxygen exposure compared to the one from WT *P.f.* Fd, implying that increased stability of the heterometallic cluster in D14C variant stems from the replacement of aspartate

ligation by cysteine. Also, EPR and mass spectrometric studies of novel ferredoxins containing the [Ag-Fe_3S_4] cluster have proven to be more stable than those containing the [Zn-Fe_3S_4] cluster. Furthermore, the stability studies of [Ag-Fe_3S_4] ferredoxins have shown that they are much more inert towards oxygen exposure than other artificial ferredoxins containing heterometallic clusters, especially the [Ag-Fe_3S_4] D14C *P.f.* Fd which remains intact after several days spent under aerobic conditions suggesting that it is oxygen inert.

Mass spectrometric analysis of intact metalloproteins has been extensively used in these studies. Its primary use was to identify species present in a protein sample, and further on to assign the oxidation state of the metal-cluster present in their active center and the presence or the absence of disulfide bonds. Even though the information that are sought are determined by measuring a relatively small change in a molecular mass of the metalloprotein, mass spectrometry has proved to be very efficient. With an appropriate calibration of the instrument, it has been shown throughout this project that accurate assignment of changes such as oxidation state of the metal-cluster is possible. This accurate assignment has also been confirmed by EPR spectroscopy e.g. in section 7.5.2.2 where the EPR active species was correctly assigned from its mass spectrum. Based on the data presented in this study, mass spectrometric analysis of intact metalloproteins can be used for the small systems as ferredoxins (7.5 kDa) to correctly assign the oxidation state of its metal-cluster. It is by far the fastest, the simplest and the most efficient way of analyzing these systems.

10 Publications

Article submitted to *J. Biol. Inorg. Chem.* under revision

Crystal structures of the all cysteinyl coordinated D14C variant of *Pyrococcus furiosus* ferredoxin: [4Fe-4S] ↔ [3Fe-4S] cluster conversion

Monika Nøhr Løvgreen, Maja Martic, Michael S. Windahl, Hans E. M. Christensen and Pernille Harris

Abstract
The structure of the all cysteinyl coordinated D14C variant of [4Fe-4S] ferredoxin from the hyperthermophilic archaeon *Pyrococcus furiosus* has been determined to 1.7 Å resolution from a crystal belonging to space group $C222_1$ with two types of molecules, A and B, in the asymmetric unit. The crystal packing reveals a β-sheet interaction between A molecules in adjacent asymmetric units. The B molecules do not show the same interaction and are packed as monomers in a less rigid position next to the A-A extended β-sheet dimers. The A molecule of the asymmetric unit contains a double conformation of the disulfide bond existing in a 60 % occupancy of the left-handed and a 40 % occupancy of the right-handed spiral conformation, while molecule B has a disulfide bond in a right-handed spiral conformation.

The cluster in D14C [4Fe-4S] *Pyrococcus furiosus* ferredoxin was chemically oxidized to [3Fe-4S]. When purified at pH 8.0, two forms of the protein are obtained. Mass spectrometric analysis shows that the two forms are the D14C [3Fe-4S] *Pyrococcus furiosus* ferredoxin monomer and a disulfide bonded dimer of D14C [3Fe-4S] *Pyrococcus furiosus* ferredoxin. When purified at pH 5.8, only the monomer is obtained.

The crystal structure of D14C [3Fe-4S] *Pyrococcus furiosus* ferredoxin monomer was determined to 2.8 Å resolution from a crystal belonging to space group $P2_12_12_1$ with two molecules in the asymmetric unit. The molecules resemble molecule A of D14C [4Fe-4S] *Pyrococcus furiosus* ferredoxin and electron density clearly shows the presence of a [3Fe-4S] cluster.

Bibliography

1. **Beinert, H.; Kennedy, M.C.; Stout, C.D.** Aconitase as iron−sulfur protein, enzyme, and iron-regulatory protein. *Chem. Rev.* 1996, 96, 2335-2373.

2. **Kim, J.; Rees, D.C.** Structural models for the metal centers in the nitrogenase molybdenum-iron protein. *Science.* 1992, 257, 1677-1682.

3. **Aono, S.; Bryant, F.O.; Adams, M.W.W.** A novel and remarkably thermostable ferredoxin from the hyperthermophilic archaebacterium *Pyrococcus furiosus*. *J. Bacteriol.* 1989, 171, 3433-3439.

4. **Nielsen, M.S.; Harris, P.; Ooi, B.L.; Christensen, H.E.M.** The 1.5 Å resolution crystal structure of $[Fe_3S_4]$-ferredoxin from the hyperthermophilic archaeon *Pyrococcus furiosus*. *Biochemistry.* 2004, 43, 5188-5194.

5. **Lu, Yi.** Metalloprotein design & engineering. [ed.] R. Bruce King. *Encyclopedia of Inorganic Chemistry.* Chichester: John Wiley & Sons, 2005, 3159-3192.

6. **Lu, Y; Yeung, N; Sieracki, N; Marshall, N.M.** Design of functional metalloproteins. *Nature.* 2009, 460, 855-862.

7. **Benson, D.E.; Wisz, M.S.; Hellinga, H.W.** The development of new biotechnologies using metalloprotein design. *Curr. Opin. Biotech.* 1998, 9, 370-376.

8. **Hellinga, H.W.** Metalloprotein design. *Curr. Opin. Biotech.* 1996, 7, 437-441.

9. **DeGrado, W. F.; Summa, C. M.; Pavone, V.; Nastri, F.; Lombardi, A.** *De novo* design and structural characterization of proteins and metalloproteins. *Annu. Rev. Biochem.* 1999, 68, 779–819 .

10. **DeGrado, W.F.; Wasserman, Z.R.; Lear, J.D.** Protein design, a minimalist approach. *Science.* 1989, 243, 622-628.

11. **Ghosh, D.; Pecoraro, V.L.** Probing metal–protein interactions using a *de novo* design approach. *Curr. Opin. Chem. Biol.* 2005, 9, 97–103.

12. **Choma, C. T.; Lear, J.D.; Nelson, M.J.; Dutton, P.L.; Robertson, D.E.; DeGrado, W.F.** Design of a heme-binding four-helix bundle. *J. Am. Chem. Soc.* 1994, 116, 856–865 .

13. **Reedy, C. J.; Gibney, B. R.** Heme protein assemblies. *Chem. Rev.* 2004, 104, 617–649.

14. **Matzapetakis, M.; Farrer, B.T.; Weng, T.; Hemmingsen,L.; Penner-Hahn, J.E.; Pecoraro, V.L.** Comparison of the binding of cadmium(II), mercury(II), and arsenic(III) to the *de novo* designed peptides TRI L12C and TRI L16C. *J. Am. Chem. Soc.* 2002, 124, 8042–8054.

15. **Barker, P.D.; Ferrer, J.C.; Mylrajan, M.; Loehr, T.M.; Feng, R.; Konishi, Y.; Funk, W.D.; MacGillivray, R.T.; Mauk, A.G.** Transmutation of a heme protein. *Proc. Natl. Acad. Sci. U.S.A.* 1993, 90, 6542-6546.

16. **Yeung, B. K. S.; Wang, X.; Sigman, J. A.; Petillo, P. A.; Lu, Y.** Construction and characterization of a manganese-binding site in cytochrome c peroxidase: towards a novel manganese peroxidase. *Chem. Biol.* 1999, 4, 215-221.

17. **Lu, Y.** Design and engineering of metalloproteins containing unnatural amino acids or non-native metal-containing cofactors. *Curr. Opin. Chem. Biol.* 2005, 9, 118-126.

18. **Merrifield B.** Concept and early development of solid-phase peptide synthesis. *Methods Enzymol.* 1997, 289, 3-13.

19. **Ikeda Y.; Kawahara S.; Taki M.; Kuno A.; Hasegawa T.; Taira K.** Synthesis of a novel histidine analog and its efficient incorporation into a protein *in vivo*. *Protein Eng.* 2003, 16, 699-706.

20. **Noren, C. J.; Anthony-Cahill, S. J.; Griffith, M. C.; Schultz, P. G.** A general method for site-specific incorporation of unnatural amino acids into proteins. *Science.* 1989, 244, 182–188 .

21. **Privett, H.K.; Reedy, C.J.; Kennedy, M.L.; Gibney, B.R.** Nonnatural amino acid ligands in heme protein design. *J. Am. Chem. Soc.* 2002, 124, 6828-6829.

22. **Peacock, A. F. A.; Hemmingsen, L.; Pecoraro, V. L.** Using diastereopeptides to control metal ion coordination in proteins. *Proc. Natl Acad. Sci.* 2008, 105, 16566-16571.

23. **Hayashi, T.; Hisaeda, Y.** New functionalization of myoglobin by chemical modification of heme-propionates. *Acc. Chem. Res.* 2002, 35, 35-43 .

24. **Johnson, M.K.; Smith, A.D.** Iron-sulfur proteins. [ed.] R.B. King. *Encyclopedia of Inorganic Chemistry.* New York: John Wiley & Sons, 2006.

25. **Fukuyama, K.** Ferredoxins containing one [4Fe-4S] center. [ed.] A. Messerschmidt, et al. *Handbook of Metalloproteins.* New York: John Wiley & Sons, 2001.

26. **Edwards, M.R.** From a soup or a seed? Pyritic metabolic complexes in the origin of life. *Trends. Ecol. Evol.* 1998, 13, 178-181.

27. **Wächtershäuser, G.** From volcanic origins of chemoautotrophic life to Bacteria, Archaea and Eukarya. *Phil. Trans. Ecol. Evol. B.* 2006, 361, 1787-1808

28. **Meyer, J.** Iron-sulfur protein folds, iron-sulfur chemistry, and evolution. *J. Biol. Inorg. Chem.* 2008, 13, 157-170.

29. **Jensen, K. P.; Ooi, B.-L.; Christensen, H. E. M.** Computational chemistry of modified [MFe_3S_4] and [$M_2Fe_2S_4$] clusters: Assessment of trends in electronic structure and properties. *J. Phys. Chem. A.* 2008, 112, 12829-12841.

30. **Conover, R.C.; Kowal, A.T.; Fu, W.; Park, J.; Aono, S.; Adams, M.W.W.; Johnson, M.K.** Spectroscopic characterization of the novel iron-sulfur cluster in *Pyrococcus furiosus* ferredoxin. *J. Biol. Chem.* 1990, 265, 8533-8541.

31. **Dance, I.** The hydrogen chemistry of the FeMo-co active site of nitrogenase. *J. Am. Chem. Soc.* 2005, 127, 10925-10942.

32. **Kiley, P.J.; Beinerty, H.** The role of Fe–S proteins in sensing and regulation in bacteria. *Curr. Opin. Microbiol.* 2003, 6, 181-185.

33. **Beinert, H.; Holm, R. H.; Münck, E.** Iron-sulfur clusters: Nature's modular, multipurpose structures. *Science.* 1997, 277, 653-659.

34. **Saridakis, E.; Giastas, P.; Efthymiou, G.** Insight into the protein and solvent contributions to the reduction potentials of [4Fe-4S]$^{(2+/+)}$ clusters: crystal structures of the *Allochromatium vinosum* ferredoxin variants C57A and V13G and the homologous *Escherichia coli* ferredoxin . *J. Biol. Inorg. Chem.* 2009, 14, 783-799 .

35. **Dey, A.; Jenney Jr., F.E.; Adams, M.W.W.; Babini, E.; Takahashi, Y.; Fukuyama, K.; Hodgson, K.O.; Hedman, B.; Solomon, E.I.** Solvent tuning of electrochemical potentials in the actice sites of HiPIP versus ferredoxin. *Science.* 2007, 318, 1464-1468.

36. **Moura, J.J.; Moura, I.; Kent, T.A.; Lipscomb, J.D.; Huynh, B.H.; LeGall, J.; Xavier, A.V.; Münck, E.** Interconversions of [3Fe-3S] and [4Fe-4S] clusters. Mossbauer and electron paramagnetic resonance studies of *Desulfovibrio gigas* ferredoxin II. *J. Biol. Chem.* 1982, 257, 6259-6267.

37. **Busch, J.L.H.; Breton, J.L.; Bartlett, B.M.; Armstrong, F.A.; James, R.; Thomson, A.J.** [3Fe-4S]-[4Fe-4S] cluster interconversion in *Desulfovibrio africanus* ferredoxin III: properties of an Asp14Cys mutant. *Biochem. J.* 1997, 323, 95-102.

38. **Silva, P.J.; van den Ban, E.C.D.; Wassink, H.; Haaker, H.; Castro, B.; Robb, F.T.Hagen, W.R.** Enzymes of hydrogen metabolism in *Pyrococcus furiosus*. *Eur. J. Biochem.* 2000 , 267, 6541-6551.

39. **Calzolai, L.; Gorst, C.M.; Zhao, Z-H.; Teng, Q.; Adams, M.W.W.; La Mar, G.N.** 1H NMR Investigation of the electronic and molecular structure of the four-iron cluster ferredoxin from the hyperthermophile *Pyrococcus furiosus*. Identification of Asp 14 as a cluster ligand in each of the four redox states. *Biochemistry.* 1995, 34, 11373-11384.

40. **Hasan, M.N.; Hagedoorn, P.L.; Hagen, W.R.** *Pyrococcus furiosus* ferredoxin is a functional dimer. *FEBS Letters.* 2002, 531, 335-338.

41. **Zhou, Z.H.; Adams, M.W.W.** Site-directed mutations of the 4Fe-ferredoxin from the hyperthermophilic archaeon *Pyrococcus furiosus:* Role of the cluster-coordinating aspartate in physiological electron transfer reactions. *Biochemistry.* 1997, 36, 10892-10900.

42. **Brereton, P.S.; Verhagen, M.F.J.M.; Zhou, Z.H.; Adams, M.W.W.** Effect of iron-sulfur cluster environment in modulating the thermodynamic properties and biological function of ferredoxin from *Pyrococcus furiosus*. *Biochemistry.* 1998, 37, 7351-7362.

43. **Duderstadt, E.E.; Staples, C.R.; Brereton, P.S.; Adams, M.W.W.; Johnson, M.K.** Effects of mutations in aspartate 14 on the spectroscopic properties of the [Fe_3S_4] clusters in *Pyrococcus furiosus* ferredoxin. *Biochemistry.* 1999, 38, 10585-10593.

44. **Brereton, P.S.; Duderstadt, R.E.; Staples, C.R.; Johnson, M.K.; Adams, M.W.W.** Effect of serinate ligation at each of the iron sites of the [Fe_4S_4] cluster of *Pyrococcus*

furiosus ferredoxin on the redox, spectroscopic, and biological properties. *Biochemistry.* 1999, 38, 10594-10605.

45. **Holm, R.H.** Trinuclear cuboidal and heterometallic cubane-type iron-sulfur clusters: new structural and reactivity themes in chemistry and biology. *Adv. Inorg. Chem.* 1992, 38, 1-71.

46. **Moura, I.; Moura, J.J.G.** Evidence for the formation of a $CoFe_3S_4$ cluster in *Desuliovibrio gigas* ferredoxin II. *J. Am. Chem. Soc.* 1986, 108, 349-351.

47. **Srivastava, K.K.P.; Surerus, K.K.; Conover, R.C.; Johnson, M.K.; Park, J.B.; Adam, M.W.W.; Munck, E.** Mossbauer study of $ZnFe_3S_4$ and $NiFe_3S_4$ clusters in *Pyrococcus furiosus* ferredoxin. *Inorg. Chem.* 1993, 32, 927-936.

48. **Fu, W.; Telser, J.; Hoffman, B.M.; Smith, E.T.; Adam, M.W.W.; Fmegan, M.G.; Conover, R.C.; Johnson, M.K.** Interaction of Tl^+ and Cs^+ with the $[Fe_3S_4]$ Cluster of *Pyrococcus furiosus* ferredoxin: Investigation by resonance Raman, MCD, EPR, and ENDOR spectroscopy. *J. Am. Chem. Soc.* 1994, 116, 5722-5729.

49. **Finnegan, M.G.; Conover, R.C.; Park, J.B.; Zhou, Z.H.; Adams, M.W.W.; Johnson, M.K.** Electronic, magnetic, redox, and ligand-binding properties of $[MFe_3S_4]$ clusters (M = Zn, Co, Mn) in *Pyrococcus furiosus* ferredoxin. *Inorg. Chem.* 1995, 34, 5358-5369.

50. **Staples, C.R.; Dhawan, I.K.; Finnegan, M.G.; Dwinell, D.A.; Zhou, Z.H.; Huang, H.; Verhagen, M.F.J.M.; Adams, M.W.W.; Johnson, M.K.** Electronic, magnetic, and redox properties of $[MFe_3S_4]$ clusters (M = Cd, Cu, Cr) in *Pyrococcus furiosus* ferredoxin. *Inorg. Chem.* 1997, 36, 5740-5749.

51. **Dole, M.; mach, L.L.; Hines, R.L.; Mobley, R.C.; Ferguson, L.D.; Alice, M.B.** Molecular beams of macroions. *J. Chem. Phys.* 1968, 49, 2240-2247.

52. **Yamashita, M.; Fenn, J.B.** Electrospray ion source: another variation of the free-jet theme. *J. Phys. Chem.* 1984, 88, 4451-4459.

53. **Kerable, P.; Tang, L.** From ions in solution to ions in the gas phase. *Anal. Chem.* 1993, 65, 972-986.

54. **Gaskell, S.J.** Electrospray: principles and practise. *J. Mass Spectrom.* 1997, 32, 677-688.

55. **Kerable, P.** A brief overview of the present status of the mechanism involved in electrospray mass spectrometry. *J. Mass Spectrom.* 2000, 35, 804-817.

56. **Cech, N.B.; Enke, C.G.** Practical implications of some recent studies in electrospray ionization fundamentals. *Mass Spectrom. Rev.* 2001, 20, 362-387.

57. **Blades, A.T.; Ikonomou, M.G.; Kebarle, P.** Mechanism of electrospray mass spectrometry. Electrospray as an electrolysis cell. *Anal. Chem.* 1991, 63, 2109-2114.

58. **Iribarne, J.V.; Thomson, B.A.** On the evaporation of small ions from charged droplets. *J. Chem. Phys.* 1976, 64, 2287-2294.

59. **Fenn, J.B.** Ion formation from charged droplets: roles of geometry, energy, and time. *J. Am. Soc. Mass Spectrom.* 1993, 4, 524-535.

60. **de la Mora, J.F.** Electrospray ionization of large multiply charged species proceeds via Dole's charged residue mechanism. *Analytica Chimica Acta.* 2000, 406, 93-104.

61. **Emmet, M.R.; Caprioli, R.M.** Micro-electrospray mass spectrometry: Ultra-high-sensitivity analysis of peptides and proteins. *J. Am. Soc. Mass Spectrom.* 1994, 5, 605-613.

62. **Wilm, M.S.; Mann, M.** Electrospray and Taylor cone theory: Dole's beam of macromolecules at last? *Int. J. Mass Spectrom. Ion Proces.* 1994, 136, 167-180.

63. **Herbert, C.G.; Johnstone, R.A.W.** *Mass Spectrometry Basics.* Boca Raton: CRC Press, 2003.

64. **Juraschek, R.; Dulcks, T.; Karas, M.** Nanoelectrospray - more than just a minimized flow electrospray ionization source. *J. Am. Soc. Mass Spectrom.* 1999, 10, 300-308.

65. **Watson, J.T.; Sparkman, O.D.** *Introduction to Mass Spectrometry.* 4th Edition: John Wiley & Sons, 2007.

66. **Johnson, K.A.; Verhagen, M.F.J.M.; Brereton, P.S.; Adams, M.W.W.; Amster, I.J.** Probing the stochiometry and oxidation states of metal centers in iron-sulfur proteins using electrospray FTICR mass spectrometry. *Anal. Chem.* 2000, 72, 1410-1418.

67. **Johnson, K.A.; Verhagen, M.F.J.M.; Adams, M.W.W.; Amster, I.J.** Difference between positive and negative ion stabilities of metal-sulfur cluser proteins: and electrospray ionization Fourier transform ion cyclotron resonance study. *Inter. J. Mass Spectrom.* 2001, 204, 77-85.

68. **Johnson, K.A.; Amster, I.J.** First observation by mass spectrometry of a 3+ oxidation state for [4Fe-4S] metalloprotein: An ESI-FTICR mass spectrometry of the high potential iron-sulfur protein from Chromatium vinosum. *J. Am. Soc. Mass Spectrom.* 2001, 12, 819-825.

69. **de Hoffmann, E.; Stroobant, V.** *Mass Spectrometry - Principles and Applications.* 3rd Edition: John Wiley & Sons, 2007.

70. **Loo, J.A.** Electrospray ionization mass spectrometry: a technology for studying noncovalent macromolecular complexes. *Int. J. Mass Spectrom.* 2000, 200, 175-186.

71. **Hernandez, H.; Robinson, C.V.** Determination the stoichiometry and interactions of macromolecular assemblies from mass spectrometry. *Nat. Protoc.* 2007, 2, 715-726.

72. **Veenestra, T.D.** Electrospray ionization mass spectrometry in the study of biomolecular non-covalent interactions. *Biophys. Chem.* 1999, 79, 63-79.

73. **Verkerk, U.H.; Kerable, P.** Ion-ion and ion-molecule reactions at the surface of proteins produced by nanospray. Information on the number of acidic residues and

control of the number of ionized acidic and basic residues. *J. Am. Soc. Mass Spectrom.* 2005, 16, 1325-1341.

74. **Iavarone, A.T.; Udekwu, O.A.; Williams, E.R.** Buffer loading for counteracting metal salt-induced signal suppression in electrospray ionization. *Anal. Chem.* 2004, 76, 3944-3950.

75. **Chernushevich, I.V.; Thomson, B.A.** Collisional cooling of large ions in electrospray mass spectrometry. *Anal. Chem.* 2004, 76, 1754-1760.

76. **Stephens, W.E.** A pulsed mass spectrometer with time dispersion. *Phys. Rev.* 1946, 69, 691.

77. **Wiley, W.C.; McLaren, I.H.** TOF-MS. *Rev. Sci. Instrum.* 1955, 26, 1150-1157.

78. **Ham, B.M.** *Even Electron Mass Spectrometry with Biomolecule Applications.* John Wiley & Sons, Inc., 2008.

79. Waters LCT Premier Operator's Guide. USA: Waters Corporation, 2006.

80. **Jankovics, H.; Kristensen, J.; Christophersen, S.; Nielsen, M.S.; Gudmundsdóttir, H.; Martic, M.; Ooi, B.L.; Christensen, H.E.M.** High-level expression of low-potential iron-sulfur proteins in *Escherichia coli*: Exemplified by expression of *Pyrococcus furiosus* ferredoxin. Article in preparation.

81. **Johannessen, M.N.** *Expression, purification, crystallization and crystal structure of the all cysteinyl coordinated D14C mutant of [Fe_4S_4] Pyrococcus furiosus ferredoxin and initial preparation and purification of a molybdenum-sulfur analogue.* Department of Chemistry, DTU. 2007. Master Thesis.

82. **Løvgreen, M.N.** *Studies of proteins and enzymes involved in the nucleotide metabolism and iron-sulfur proteins.* Department of Chemistry, Technical University of Denmark. to be published. PhD Thesis.

83. **Bas, D.C.; Rogers, D.M.; Jensen, J.H.** Very fast empirical prediction and rationalization of protein pKa values. *Proteins: Struct. Funct. Bioinf.* 2008, 73, 765-783.

84. **Li, H.; Robertson, A.D.; Jensen, J.H.** Very fast prediction and rationalization of protein pKa values. *Proteins: Struct. Funct. Bioinf.* 2005, 61, 704-721.

85. **Kolthoff, I.M.; Tomsicek, W.J.** The oxidation potential of the system potassium ferrocyanide–potassium ferricyanide at various ionic strengths. *J. Phys. Chem.* 1935, 39, 945-954.

86. **Kristensen, J.** *Synthesis, purification and characterization of ferredoxins with re-designed active sites.* Department of Chemistry, DTU. 2010. PhD Thesis.

87. **Park, J.; Fanp, C.; Hoffmang, B.M.; Adams, M.W.W.** Potentiometric and electron nuclear double resonance properties of the two spin forms of the $[4Fe\text{-}4S]^+$ cluster in the novel ferredoxin from the hyperthermophilic archaebacterium *Pyrococcus furiosus*. *J. Biol. Chem.* 1991, 266, 19351-19356.

88. **Zhang, J.; Christensen, H.E.M.; Ooi, B.L.; Ulstrup, J.** In situ STM imaging and direct electrochemistry of *Pyrococcus furiosus* ferredoxin assembled on thiolate-modified Au(111) surfaces. *Langmuir.* 2004, 20, 10200-10207.

89. **Fawcett, S.E.J.; Davis, D.; Breton, J.L.; Thomson, A.J.; Armstrong, F.A.** Voltammetric studies of the reactions of iron–sulphur clusters ([3Fe-4S] or [M3Fe-4S]) formed in *Pyrococcus furiosus* ferredoxin. *Biochem. J.* 1998, 335, 357-368.

90. **Smith, E.T; Blarney, J.M.; Zhou, Z.H.; Adams, M.W.W.** A variable-temperature direct electrochemical study of metalloproteins from hyperthermophilic microorganisms involved in hydrogen production from pyruvate. *Biochemistry.* 1995, 34, 7161-7169.

91. **Hasan, M.N.; Kwakernaak, C.; Sloof, W.G.; Hagen, W.R.** *Pyrococcus furiosus* 4Fe-ferredoxin, chemisorbed on gold, exhibits gated reduction and ionic strength dependent dimerization. *J. Biol. Inorg. Chem.* 2006, 11, 651-662.

92. **Skoog, D.A.; West, D.M.; Holler, F.J.; Crouch, S.R.** *Fundamental of Analytical Chemistry.* 8th Ediition: Brookks/Cole - Thomson Learning, 2004.

93. **Moreno, C.; Macedo, A.L.; Moura, I.; LeGall, J.; Moura, J.J.G.** Redox properties of *Desulfovibrio gigas* $[Fe_3S_4]$ and $[Fe_4S_4]$ ferredoxins and heterometal cubane-type clusters fromed within the $[Fe_3S_4]$ core. Square wave voltammetric studies. *J. Inorg. Biochem.* 1994, 53, 219-234.

94. **Surerus, K.K; Munck, E.** Evidence for the formation of $ZnFe_3S_4$ cluster in *Desulfovibrio gigas* ferredoxin II. *J. Am. Chem. Soc.* 1987, 109, 3805-3807.

95. **Butt, J.N.; Armstrong, F.A.; Breton, J.; George, S.G.; Thomson, A.J.; Hatchikian, E.C.** Investigation of metal ion uptake reactivities of [3Fe-4S] clusters in proteins: Voltammetry of Co-Adsorbed ferredoxin-aminocyclitol films at graphite electrodes and spectroscopic identification of transformed clusters. *J. Am. Chem. Soc.* 1991, 113, 6663-6670.

96. The software can be obtained from http://www.tnw.tudelft.nl (10-12-2010)

97. **Zhou, J.; Raebiger, J.W.; Crawford, C.A.; Holm, R.H.** Metal ion incorporation reactions of the cluster $[Fe_3S_4(LS_3)]^{3-}$,containing the cuboidal $[Fe_3S_4]^0$ core. *J. Am. Chem. Soc.* 1997, 119, 6242-6250.